Three Dimensional Spatio-Temporal Model-based SAR Algorithms for Monitoring Large Gradient Deformations in Mining Areas

Author

Sen Du

Thesis Supervisor

Jordi J. Mallorquí

A thesis submitted to the Universitat Politècnica de Catalunya (UPC)
in partial fulfillment of the requirements for the degree of
DOCTOR OF PHILOSOPHY

Ph.D program on Signal Theory and Communications
CommSensLab - Unidad de Excelencia María de Maeztu
Universitat Politècnica de Catalunya (UPC)
Barcelona, March 2022

Thesis written by Sen Du

Three Dimensional Spatio-Temporal Model-based SAR Algorithms for Monitoring Large Gradient Deformations in Mining Areas

Ph.D. program on Signal Theory and Communications

This work has been supported by the National Key R&D Program of China (Grant No. 2022YFE0102600), China Scholarship Council (Grant 201806420035), the Spanish Ministry of Economy, Industry and Competitiveness (MINECO), the Agencia Estatal de Investigación (AEI), the European Funds for Regional Development (EFRD) under project TEC2017-85244-C2-2-P, the National Natural Science Foundation of China (Grant 41874044, 42004011) and programme of Introducing Talents of Discipline to Universities, Plan 111 (Grant No. B20046). CommSensLab is Unidad de Excelencia María de Maeztu MDM-2016-0600 financed by the AEI, Spain.

献给我的父亲、母亲，我的弟弟，

我的爱人汪泽。

To my families,

and my cherished Ze Wang.

路漫漫其修远兮，吾将上下而求索。

——屈原《离骚》

The road is long, but I will keep going.

--- from Qu Yuan in ‘‘Encounter in Sorrow’’

There is nothing noble in being superior to some other man. The true nobility is in being superior to your previous self.

--- Ernest Miller Hemingway

Acknowledgments

On October 18, 2018, after a long flight, I came to Barcelona from China and embarked on an unforgettable journey. Getting of the plane, Dr. Zhongbo Hu's pick-up made me feel warm. After three years, this journey will come to an end as the studies are about to be completed. During this period, I experienced the warm Spanish sun and the beautiful beaches of Barcelona. A joyful life is inseparable from the help and company of many people. I would like to take this opportunity to express my gratitude to everyone.

First of all, I would like to thank my supervisor, Professor Jordi J. Mallorquí. For scientific research, he is not only my beacon, but also my think tank. His professional knowledge makes all the research problems not so difficult. His attitude towards research is so serious that I would benefit from it for my future research work. His humor, passion and enthusiasm influence me a lot, teach me to enjoy my life.

I would like to thank Professor Yunjia Wang and Hongdong Fan of China University of Mining and Technology (CUMT) for their help in my master's career. When I stand at the crossroad, their suggestions point me like a signpost.

I would like to thank Dr. Zhongbo Hu, Dr. Feng Zhao, and Dr. Meinan Zheng. The research discussions and joyful chats with them always make me satisfies. Dr. Hu Zhongbo is a bridge between UPC and CUMT and helped me establish contact with Professor Jordi J. Mallorquí. He also patiently helped me with many problems that blocked me and Barcelona, such as scholarship application and accommodation.

I would like to thank the friends who share the same office with me, Jorge, Giselle, Fae, Luca, Patrick, Susana, Youness, Christian, Xavier, Jun Ni, Miquel, Rocio, Cristina, Mireia and Tieyan Yi. It is fate for everyone from all over the world to gather in a small room. Your presence makes this room full of vitality and laughter. I hope you will be successful in your future work and study. Especially Cristina and Mireia, thank you for translating Spanish to me, you really help me a lot.

Last but not least, I would like to thank my parents, my twin brother and my wife. My parents nurture me, raise me, give me everything I need, especially their love. With a twin brother, I think miracles are possible in the world, and they are even possible to happen to me. My wife Ze Wang, she sacrificed too much due to my PhD career. She sacrificed her job, her time, came to my side to accompany me and take care of me. Half of the medals are hers. Home is where she is.

This work has been financially supported in part by the National Key R&D Program of China (Grant No. 2022YFE0102600), in part by the Spanish Ministry of Economy,

Industry and Competitiveness (MINECO), the State Research Agency (AEI) and the European Funds for Regional Development (EFRD) under Project TEC2017-85244-C2-2-P, in part by the National Natural Science Foundation of China under Grant 42004011 and Grant 41874044, and in part by CommSensLab, Unidad de Excelencia Maria de Maeztu through the State Research Agency (AEI), Spain, under Grant MDM-2016-0600, by the China Scholarship Council under Grant 201806420035, by programme of Introducing Talents of Discipline to Universities, Plan 111 (Grant No. B20046).

Contents

Abstract

During the last decade, space-borne based Differential Synthetic Aperture Radar Interferometry (DInSAR), also known as Persistent Scatters Interferometry (Persistent Scatters Interferometry (PSI)), and SAR data based Offset Tracking (OT) techniques have matured to the widely used deformation monitoring tools. Compared with the conventional ground deformation monitoring methods, Synthetic Aperture Radar Interferometry (InSAR) has the advantages of dense spatial sampling and large coverage, independence of light and weather. Despite these advantages, according to Nyquist-Shannon sampling theorem, phase unwrapping based InSAR has a deformation gradient limit for retrieving deformation. Although higher resolution and longer wavelength could lessen this innate restriction, some large deformations caused by earthquakes, landslides, minings and volcanisms are still beyond the monitoring capability of InSAR. As complementary to InSAR, OT with SAR amplitude images is an efficient tool for large ground deformation monitoring. The offsets among pixels between two images can be obtained with a simple cross correlation calculation. In general, the accuracy can be very high in the presence of strong point-like scatterers or with the help of ad-hoc deployed Corner Reflector (CR). However, when the deformation is distributed these point-like targets cannot be a good representation of the terrain deformation and even induce errors on the deformation maps, known as Patch Like (PL), if their reflectivity strongly change along time. These errors are clearly visible in the results, but they are difficult to detect with the different error estimation methods, like the Signal-to-Noise Ratio (SNR) or similar. In addition, the huge potential of polarization SAR data remains locked for the amplitude information based OT technology. For example, to the best knowledge of the authors, there is no single example of a polarization based image optimization method that has been developed for OT processing. ***In this context, large gradient deformation extraction algorithms for SAR/InSAR are crucial for improving the accuracy of OT and extending the monitoring capability of InSAR.*** In this thesis, large gradient deformation extraction algorithms have been investigated for OT and InSAR applications.

Firstly, an External Model Deformation Decomposition based Persistent Scatters Interferometry (EMDD-PSI) method has been proposed. This method first uses interferograms generated from SAR Single Look Complex (SLC) images to optimize the parameters of the external model. Then, the number of fringes in the original interferograms are reduced by the modeled subsidence phase produced from the external model to ease the PSI processing. Finally, the ground deformation is retrieved jointly adding the external model and PSI results. The capabilities of the proposed method

is demonstrated by 14 Radarsat-2 SAR images over the Fengfeng mining area (China). The deformation obtained by the proposed method is evaluated by the leveling data. Results have shown that after the optimization, the external model is able to mimic the real deformation and the fringes of the interferograms can be reduced effectively. As a consequence, the large gradient deformation can be better retrieved with the preservation of the nonlinear subsidence term.

Second, to reduce the PL, a novel amplitude filter, i.e. the Pacth-Like Reduction (PLR), is developed. The proposed PLR reduces the PL effects by replacing the pixels with extremely high amplitudes with zero. Three different SAR data sets and in-field Global Positioning System (GPS) measurements are used to evaluate the performance of the proposed method. The results show that PL effects can be reduced with the proposed amplitude filter. The processing parameters of the improved OT are optimized as well, considering both the relationship between the deformation resolution and the size of matching template and the effect of different window functions in the final results.

Third, a polarization data based Amplitude Contrast Enhancement Offset Tracking (ACE-OT) is proposed. The method first uses the Kennaugh matrix to construct the optimal polarization formula with 6 optimal parameters. Then, the 6 optimal parameters leading to the highest contrast are searched. Finally, amplitude contrast enhanced SAR image can be obtained by the optimized polarization formula. The 31 quad-pol Radarsat-2 images covering Barcelona Airport and 20 dual-pol TerraSAR-X images are used to verify the proposed method. The enhancement result shows that the contrasts of the amplitude images are increased, which also improves the correlation of the image pair. Therefore, the ACE-OT can achieve better results than the OT with unenhanced amplitude images.

To conclude, a PSI processing algorithm with external model and two improved OT methods have been proposed in this thesis. I hope the work presented in this thesis could make some contributions to the research area of ***"Large gradient deformation extraction algorithms for SAR/InSAR".***

Resumen

Durante la última década, la interferometría diferencial basada en radares de apertura sintética (Differential Interferometric Synthetic Aperture Radar, DInSAR) orbital, también conocida como interferometría de dispersión persistente (Persistent Scatter Interferometry, PSI), y las técnicas de seguimiento de desplazamiento (Offset Tracking, OT) basadas en datos de radar de apertura sintética (SAR) han madurado hasta convertirse en una de las más ampliamente utilizadas herramientas de monitorización de deformaciones. En comparación con los métodos convencionales de monitorización de la deformación del suelo, las técnicas DInSAR tienen las ventajas de un muestreo espacial denso y una gran cobertura, independencia de la iluminación solar y del tiempo meteorológico. A pesar de estas ventajas, según el teorema de muestreo de Nyquist-Shannon, las técnicas interferométricas basadas en el desenrollado de fase tiene un límite de gradiente de deformación para poder recuperarla. Aunque una resolución más alta y una longitud de onda más larga podrían disminuir esta restricción innata, algunas grandes deformaciones causadas por terremotos, deslizamientos de tierra, minería y volcanismo aún están más allá de la capacidad de monitorización de DInSAR. Como complemento a DInSAR, OT con imágenes de amplitud es una herramienta eficiente para la monitorización de grandes deformaciones del suelo. Los desplazamientos entre píxeles entre dos imágenes se pueden obtener con un simple cálculo de correlación cruzada. En general, la precisión puede ser muy alta en presencia de fuertes puntos de dispersión (blancos puntuales) o con la ayuda de reflectores (Corner Reflectors, CR) desplegados ad-hoc. Sin embargo, cuando la deformación es distribuida, estos blancos puntuales no pueden ser una buena representación de la deformación del terreno e incluso inducen errores en los mapas de deformación, conocidos como Patch Like (PL), si su reflectividad cambia fuertemente a lo largo del tiempo. Estos errores son claramente visibles en los resultados, pero son difíciles de detectar con los diferentes métodos de estimación de errores, como el Signal-to-Noise Ratio (SNR) o similares. Además, el enorme potencial de los datos SAR polarimétricos no se explota en la tecnología OT basada en información de amplitud. Por ejemplo, según el mejor conocimiento del autor, no existe un solo ejemplo de un método de optimización de imagen basado en polarización que se haya desarrollado para el procesado OT. ***En este contexto, los algoritmos de extracción de deformación en presencia de grandes gradientes para SAR/DInSAR son cruciales para mejorar la precisión de OT y ampliar la capacidad de monitoreo de DInSAR.*** En esta tesis, se han investigado algoritmos de extracción de deformación en presencia de grandes gradiente para aplicaciones OT e InSAR.

En primer lugar, se ha propuesto un método PSI basado en la descom-

posición de la deformación con modelo externo (EMDD-PSI). Este método primero utiliza interferogramas generados a partir de imágenes SAR Single Look Complex (SLC) para optimizar los parámetros del modelo externo de deformación. Luego, el número de franjas en los interferogramas originales se reduce por la fase de hundimiento modelada producida a partir del modelo externo para facilitar el procesado PSI. Finalmente, la deformación del terreno se recupera conjuntamente agregando el modelo externo y los resultados PSI. Las capacidades del método propuesto se demuestran con 14 imágenes Radarsat-2 SAR sobre el área minera de Fengfeng (China). La deformación obtenida por el método propuesto es evaluada con los datos de nivelación precisa adquiridos sobre el terreno. Los resultados han demostrado que después de la optimización, el modelo externo puede imitar la deformación real y las franjas de los interferogramas se pueden reducir de manera efectiva. Como consecuencia, la deformación de gran gradiente se puede recuperar mejor conservando el término de hundimiento no lineal.

En segundo lugar, para reducir el PL, se desarrolla un nuevo filtro de amplitud, es decir, la reducción a Pacth Like (PLR). El PLR propuesto reduce los efectos de PL reemplazando los píxeles con amplitudes extremadamente altas con ceros. Se utilizan tres conjuntos de datos SAR diferentes y mediciones del Sistema de Posicionamiento Global (GPS) en el campo para evaluar el rendimiento del método propuesto. Los resultados muestran que los efectos de PL se pueden reducir con el filtro de amplitud propuesto. Los parámetros de procesado del OT mejorado también se optimizan, considerando tanto la relación entre la resolución de deformación y el tamaño de la plantilla coincidente como el efecto de las diferentes funciones de enventanado en los resultados finales.

En tercer lugar, se propone una mejora del contraste de las imágenes de amplitud para la mejora del procesado OT (Amplitude contrast Enhancement, ACE-OT) basado en imágenes SAR polarimétricas. El método primero usa la matriz de Kennaugh para construir la fórmula de polarización óptima con 6 parámetros óptimos. Luego, se buscan los 6 parámetros óptimos que conducen al mayor contraste. Finalmente, la imagen SAR mejorada se puede obtener mediante la fórmula de polarización optimizada. Las 31 imágenes Radarsat-2 quad-pol que cubren el Aeropuerto de Barcelona y las 20 imágenes TerraSAR-X dual-pol se utilizan para verificar el método propuesto. El resultado de la mejora muestra que los contrastes de las imágenes de amplitud aumentan, lo que también mejora la correlación del par de imágenes. Por lo tanto, el ACE-OT puede lograr mejores resultados que el OT con imágenes de amplitud no mejorada.

Para concluir, en esta tesis se ha propuesto una metodología de procesado PSI con modelo externo y dos métodos OT mejorados. Espero que el trabajo presentado en esta tesis pueda hacer algunas contribuciones al área de investigación de ***"Algoritmos de extracción de deformación de gran gradiente para SAR/InSAR".***

Acronyms

ACE Amplitude Contrast Enhancement

ACE-OT Amplitude Contrast Enhancement Offset Tracking

AHE Adaptive Histogram Enhancement

ALOS Advanced Land Observation Satellite

APS Atmospheric Phase Screen

CC Correlation Coefficient

CCF Correlation Coefficient in Frequency domain

CCFP Correlation Coefficient in Frequency domain with Phase information

CGM Conjugate Gradient Method

CPT Coherent Pixels Technique

CR Corner Reflector

CUMT China University of Mining and Technology

DEM Digital Elevation Model

DInSAR Differential Synthetic Aperture Radar Interferometry

DS Distributed Scatterer

EMDD-PSI External Model Deformation Decomposition based Persistent Scatters Interferometry

FFT Fast Fourier Transform

GOPCE Generalized Optimization of Polarimetric Contrast Enhancement

GPS Global Positioning System

InSAR Synthetic Aperture Radar Interferometry

KML Keyhole Markup Language

LDEB Linear Deformation Estimation Block

LFM Linear Frequency Modulate

LOS Line of Sight

MAR Middle Amplitude Reserving

NCC Normalized Cross Correlation

NLDEB Non-linear Deformation Estimation Block

OPCE Optimization of Polarimetric Contrast Enhancement

OT Offset Tracking

PDAOM Polarimetric Data based Amplitude Optimizing Methods

PDPOM Polarimetric Data based Phase Optimizing Methods

PIM Probability Integral Method

PL Patch Like

PLR Pacth-Like Reduction

PMCBO Parameters that Can Be Optimized

Pol-InSAR Polarimetric SAR Interferometry

PRF Pulse Repetition Frequence

PS Persistent Scatter

PSC Persistent Scatter Candidate

PSI Persistent Scatters Interferometry

PT Point-like Targets

RAR Real Aperture Radar

RBS Rubber Sheet

RMSE Root Mean Square Error

ROI Region of Interest

RTK Real-Time Kinematic

SAR Synthetic Aperture Radar

SBAS Small Baseline Subsets

SLC Single Look Complex

SLR Spatial Low Resolution

SNR Signal-to-Noise Ratio

SRTM Shuttle Radar Topography Mission

STD Standard Deviation

SVD Singular Value Decomposition

TOPS Terrain Observation by Progressive Scans

TPC Temporal Phase Coherence

UPC Universitat Politècnica de Catalunya

UTM Universal Transverse Mercator

WGS84 World Geodetic System 1984

1

Chapter 1
Introduction

Ground deformation monitoring is of great significance for human beings to explore and protect the natural and their own living environment. Conventional point-based methods such as Global Positioning System (GPS), total station, and leveling are accurate and reliable, but time and money consuming. Moreover, they are powerless in unreachable or dangerous areas. Meanwhile, as a remote sensing technique, Synthetic Aperture Radar (SAR) has the advantages of efficiency and large coverage. Besides, due to its longer signal wavelength than optical sensors, the active SAR sensors can obtain high-quality images in any weather and illumination conditions. With the unprecedented development of SAR missions (such as Sentinel-1, TerraSAR-X, ALOS-2, COSMO-SkyMed, RADARSAT-2, PAZ, Gaofen-3 and ICEYE), large amounts of SAR data are or will be available with short repeat cycles and wide swath modes. Differential Synthetic Aperture Radar Interferometry (DInSAR) and Offset Tracking (OT) are two kinds of ground deformation measurements based on SAR data. Theoretically, DInSAR can provide results with millimeter-level accuracy. However, large gradient deformation is one of its limitations, because the phase changes between adjacent pixels are assumed within π. OT is an effective supplement in this aspect because the phase is not employed. However, OT suffers from various problems caused by changes of the ground features. Therefore, DInSAR and OT need to be improved to cope with large deformations.

1.1 Persistent Scatters Interferometry (PSI) with External Model

Differential Interferometric Synthetic Aperture Radar (DInSAR), also known as Persistent Scatterer Interferometry (PSI), with its continuously improved algorithms, has been widely applied to multiple cases like earthquakes [1–3], tectonic movements [4, 5], landslides [6, 7], volcanisms [8–10], and evaluations of city ground [11], mining subsidence [12, 13] and building stability [14].

However, large deformation gradients may lead to inaccuracies of PSI monitoring results. For PSI, the phase difference between two adjacent points, either in space or time, are assumed to be within half a cycle in order to properly unwrap the phase. Large deformation patterns can cause phase jumps in the interferograms larger than half a cycle among pixels. Methods working with interferograms at full resolution, in comparison with multi-look based ones, help to reduce the chances of having wrapped phases beyond the half cycle limit, higher pixel densities help also to reduce the phase differences among neighbouring points [15].

Saving resolution or increasing Persistent Scatter (PS)s density by lowering pixels selection thresholds reduces the limitation of deformation gradient while reduces result quality. Like topography phase cancellation, phase jumps can be estimated and eliminated with the information provided by an external deformation model. This method can help PSI to retrieve large gradient deformations without losing accuracy, as long as the external models do not add extra phase jumps.

The missing integer phase cycles caused by large gradient deformations are calculated through the Probability Integral Method (Probability Integral Method (PIM)) model, so the deformation can be obtained completely [16]. This method does not discard the information monitored by InSAR, and, theoretically, it can get more detailed information. However, it assumes that the phase differences other than those calculated by the PIM model (including atmospheric errors, Digital Elevation Model (DEM) errors, and deformation phases not simulated by PIM) are less than half a cycle. This is unreasonable. The fringes of the interferograms may be too dense to allow calculating the deformation correctly. Thus, like an external DEM is used to eliminate the fringes associated to the topographic phase when generating the differential interferograms, PIM is used to reduce the number of fringes associated to deformation [17]. However, the determination of some parameters in the PIM model depends on the actual working face geological conditions and mining conditions. Different geological mining conditions will cause a large estimation error of the parameters, and when the estimated parameters are different from the actual situation, it will cause a negative impact on the subsequent fitting estimation of the model. Several methods have also been proposed to improve the performance of the constant velocity model in large gradient deformation monitoring. The Gaussian velocity model is used to estimate velocity fields and DEM errors [18]. This method can also fill areas where PS/Distributed Scatterer (DS) points are sparse or absent, but it requires the sinking area to be known. Still, a linear model is used, and the nonlinear deformation can only be obtained by the residual phase. A third-order polynomial model is used to solve the nonlinear deformation [19]. This method can obtain the obvious time series deformation of non-linear characteristics, but the cubic polynomial is not applicable to

all PS points as different subsidence phenomenon appears in different mining phases.

1.2 Offset Tracking (OT)

By detecting the offset of the pixels in the two images before and after the deformation, OT can obtain the information of the surface deformation. Before SAR acquisitions, OT was first applied on optical images [20, 21]. Remotely sensed data make it to be an extraordinary geodetic approach for large-scale deformation measurement. However, optical sensors can easily be affected by clouds and illumination situation. In contrast, SAR sensors have proven their unprecedented ability and merits of withstanding severe weather conditions, making SAR acquisitions robust for OT technology [22, 23]. The accuracy of OT largely depends on the pixel size. Due to the launch of satellites with high-resolution SAR sensors, the deformation monitoring accuracy of OT can even be comparable to the phase measurement of InSAR [24]. In addition, OT technology has high robustness in the incoherence area and can obtain large deformations that cannot be monitored by InSAR.

Due to its robustness for dealing with cases in which large deformations are present, amplitude image based Offset Tracking (OT) is widely used in the observation of glacier movements [25], mining caused ground deformations [26], landslides [27] and volcanic activity [28].

However, amplitude variations remain one of the major limitations for retrieval of deformation signals from SAR stacks. One the one hand, the correlation overestimation of reference and search window due to amplitude weighting leads to patch noise appearing in the result, Patch Like (PL). This noise harms the observation of distributed deformation and is not able to be detected by SNR indicators. On the other hand, as more satellite sensors with polarimetric capabilities have been launched, pixel selection of PSI is improved by Polarimetric Data based Phase Optimizing Methods (PDPOM) and Polarimetric Data based Amplitude Optimizing Methods (PDAOM) [29–40]. By searching the optimal solution from multidimensional space constructed from polarization data, noise can be reduced and PS number is increased. But these methods cannot be transplanted to OT. For the amplitude optimization, PDAOM works with time series data, while OT need optimization of each single image. In addition, the deformation obtained with PSI is within one pixel, while OT detects offset of several pixels, which beyond the ability of PDPOM and PDAOM.

1.3 Motivation and Objectives

The capabilities and limitations of PSI and OT are introduced in the previous part. The two methods can be improved to better acquire large gradient deformation. For this purpose, the research questions this thesis would like to cope with are:

- *How to determine parameters of an external model to help PSI obtain large gradient deformation without introducing error?*
- *How can the PL be eliminated or reduced in OT processing?*

- *How to optimize the amplitude images by polarimetric data to improve OT result?*

Corresponding to the research questions above, the research objectives are summarized as follows:

- ▶ 1) Develop an interferogram based method to optimize the parameters of the external model.
- ▶ 2) Discover the sources of the PL and exclude them.
- ▶ 3) Investigate a polarimetric optimization method for amplitude images.

1.4 Outline of the Thesis

The purpose of this thesis is to develop advanced algorithms for PSI and OT to improve their result of large gradient deformation monitoring. According to the research goals, it is structured as follows:

- Chapter 1 introduces the background and state-of-the-art of PSI obtaining large deformation and OT techniques, as well as the outline of the thesis.
- Chapter 2 introduces the basic concepts related to this thesis, including SAR imaging, Pauli decomposition, DInSAR basis, OT principles and the software used in this thesis.
- In Chapter 3, an external model-based deformation decomposition PSI method is proposed. The proposed method is explicitly evaluated in Fengfeng mining area, China, with leveling data as the ground truth. The classical PSI and PSI with unadjusted parameters are referred as comparison.
- Chapter 4 explains a middle amplitude reserving SAR OT method. The proposed method reduces the PL effects by using only the mid-range amplitude pixels to estimate the offset map between the image pair. In addition, an error estimation method is introduced, which is independent of amplitude contrast.
- Chapter 5 proposes a polarimetric data based amplitude contrast enhancement algorithm for OT. The algorithm is validated with 31 Radarsat-2 images covering Barcelona airport and 20 Terrsar-X images covering the mountainous area in China. The amplitude contrast enhancement can improve the correlation between two images before and after the deformation, which is beneficial for OT processing.
- The conclusions and future research lines are summarized in Chapter 6.

2

Chapter 2
Theoretical Basis

There are generally two methods based on SAR to monitor ground deformation. One is differential interferometry based on adjacent phase continuity and its derived time series method. The other is the shifted pixel matching based on the correlation between two SAR images before and after deformation. This chapter aims to briefly introduce the fundamentals of SAR, PolSAR, InSAR, DInSAR, and OT.

2.1 Synthetic Aperture Radar (SAR) Imaging

Radar systems can obtain information about scatterers by receiving the echoes of electromagnetic pulses transmitted at a specific Pulse Repetition Frequence (PRF). A SAR system usually consists of an active microwave sensor and a mobile platform. The direction in which the platform moves is *azimuth*, and in which the pulse is emitted is *range*.

2.1.1 Range Resolution

The resolution in range direction X_r can be determined by the speed of light in vacuum c and the pulse duration time τ or pulse bandwidth B_w:

$$X_r = \tau c/2 \simeq c/2B_w \tag{2.1}$$

where a factor 2 is related to the round trip delay. Fewer pulse times and larger bandwidths result in higher resolution, the peak power has to be increased to preserve the

same SNR. One typical solution is to use a chirp signal and the matched filter. The most commonly used matched filter [41] consists of convolving the echo signal with a conjugated time-reversed replica of the transmitted signal. In this case, the ideal signal type is a long Linear Frequency Modulate (LFM) pulse, also known as *chirp* [42]. For variable frequencies, the bandwidth is defined as:

$$B_w = \alpha\tau \tag{2.2}$$

where α is the chirp rate. Chirp signals and matched filters mean higher SNR and short pulses. After range compression, the new range resolution is:

$$X_r = c/2B_w \simeq c/2\alpha\tau \tag{2.3}$$

2.1.2 Azimuth Resolution

SAR is developed from Real Aperture Radar (RAR). For RAR systems, the azimuth resolution depends on the 3 dB azimuth beam width of the antenna. Assuming that the beam width is β, the radar wavelength is λ, and the physical length of the antenna in azimuth is D, then the relationship between them can be expressed as:

$$\beta \simeq \lambda/D \tag{2.4}$$

If the slant-range from the antenna to the target is R, then the real aperture azimuth resolution X_a is:

$$X_a = R\beta \simeq R\lambda/D \tag{2.5}$$

It can be seen from Eq. 2.5 that the azimuth resolution of RAR is limited by the antenna aperture size, the height of the flight platform, and the radar wavelength. Taking ERS-1 as an example, its wavelength is 5.66 cm, the antenna size is 10 m in azimuth and 1 m in range. The orbital altitude is 782 km − 785 km, and the look angle is 23°, which means the R is about 853 km. From these data, we can know that the azimuth resolution in the real aperture mode is about 4.8 km. To achieve an azimuth resolution comparable to the range resolution, which is 12.5 m, the antenna length needs to be increased to around 3858 m.

Overly large aperture antenna sizes are difficult to achieve, and SAR can solve this problem. The principle of aperture formation is shown in Fig. 2.1, where Q is the target, $P1$ and $P2$ are the positions where the radar first and last illuminates the target Q, respectively.

Since the transmitted and received signals are coherent, the phase of the echo signal is a function of time, determined by the distance between the target and the sensor. When the sensor moves from $P1$ to $P2$, the relative motion between the target and the sensor causes a change in the instantaneous frequency of the echo, that is, the Doppler shift. When the sensor moves in a straight line at a constant speed, the azimuth echo signal is similar to the chirp signal [43]. The received signal is pulse-compressed by an azimuth matched filter to form a synthetic aperture L_S from $P1$ to $P2$:

$$L_s \simeq R\lambda/\mathrm{D} \tag{2.6}$$

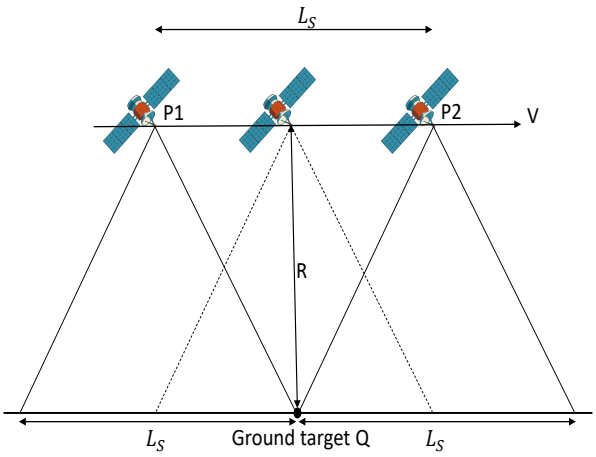

Fig. 2.1. Schematic diagram of the synthetic aperture.

In this case, the equivalent ground range covered by the beam is $2L_S$, and the beam width is:

$$\beta_s \simeq \lambda/2L_s = D/2R \tag{2.7}$$

From Eq. (2.5) to Eq. (2.7), the resolution of the synthetic aperture in azimuth direction X_a is:

$$X_a = R\beta_s \simeq D/2 \tag{2.8}$$

2.1.3 Geometric Distortions

Radar imaging is recorded based on the time it takes for the radar transmitted pulse to return to the antenna. When side looking is applied,different objects are at different distances from the radar antenna, and the signal returns to the antenna at different times, allowing the recorded signals to be differentiated. If the signal is launched vertically downward, objects symmetrical about the antenna will return to the radar antenna at the same time, and their echo signals will be mixed together and cannot be distinguished. Therefore, imaging radars often use side looking imaging. However, limited by the geometry of side looking, foreshortenings, layovers, and shadows can also result.

- Foreshortening. The foreshortening effect may be defined as the compression of the slope towards the satellite when projected onto the slant range plane. This effect is more pronounced as the local slope is closer to the incidence angle. The extreme situation occurs when the two angles are equal, in which case the slope is represented by a single point in the image.
- Layover. The layover distortion effect occurs when the angle of a slope facing the radar exceeds the incidence angle. This inverse effect in the echo arrival order

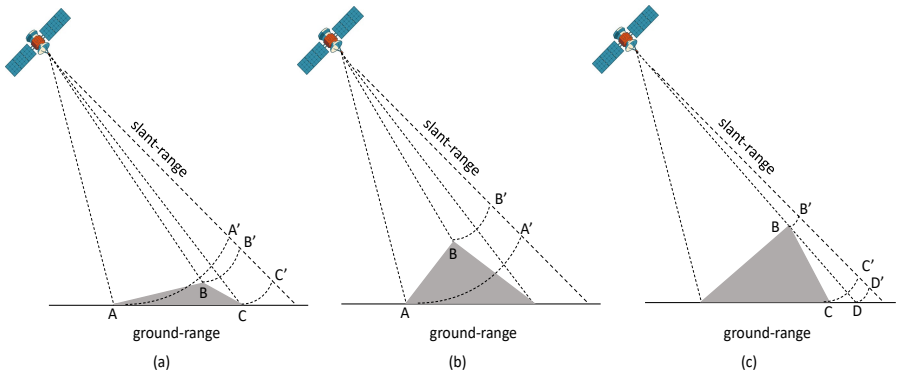

Fig. 2.2. Main SAR geometric distortions.(a) Foreshortening, (b) layover and (c) shadowing.

provokes those points located at higher elevations, which are closer to the radar, to appear earlier in SAR images. From an intuitive point of view, the tops of the mountains appear before the valleys.

- Shadowing. The shadowing effect occurs when a slope opposite to the radar has a steeper slope than the incidence angle. This causes some parts to be not illuminated by the radar, the so-called shaded areas, and thus no reflectivity or phase information from these points can be collected. Due to the absence of back-scattered signals, the compressed radar image will exhibit extremely low amplitude values in these areas.

2.2 Polarimetric SAR

One of the main characteristics of electromagnetic waves is the vectorial nature of their electromagnetic field, i.e, the polarization. By exploiting different polarization combinations of incident and reflected electromagnetic waves, the amount of information may be increased, thus benefiting a large number of SAR applications such as offset tracking or DInSAR [44]. This section provides some basic polarization knowledge to ease the comprehension of this development.

2.2.1 Electromagnetic Wave Polarization

Electromagnetic waves, propagating in free space or other homogeneous isotropic non-attenuating media, are properly described as *transverse waves*, meaning that a plane wave's electric field vector $\vec{E}$ and magnetic field $\vec{H}$ are in directions perpendicular to (or "transverse" to) the direction of wave propagation; $\vec{E}$ and $\vec{H}$ are also perpendicular to each other. By convention, the "polarization" direction of an electromagnetic wave is given by its electric field vector.

Assuming a plane wave propagates along the z axis with frequency f. As a function of time t and spatial position z, the instantaneous physical electric and magnetic fields

can be written as:

$$\vec{E}(z,t) = \begin{bmatrix} e_x \\ 0 \\ 0 \end{bmatrix} e^{j\omega t} \cdot e^{-jkz} \tag{2.9}$$

$$\vec{H}(z,t) = \begin{bmatrix} 0 \\ h_y \\ 0 \end{bmatrix} e^{j\omega t} \cdot e^{-jkz} \tag{2.10}$$

$$\vec{E} \times \vec{H} = \vec{K} \tag{2.11}$$

where λ is the wavelength, $T = 1/f$ the period of the wave, the wave number $k = 2\pi n/\lambda$, angular frequency $\omega = 2\pi f$. It can be seen from (2.9), (2.10) and (2.11) that the electric field $\vec{E}$, the magnetic field $\vec{H}$ and their propagation direction $\vec{K}$ are orthogonal to each other.

2.2.2 Polarization Ellipse

The electric field vector over an oscillation period can be plotted as an ellipse, as shown in Fig. 2.3, corresponding to a particular state of elliptical polarization. Linear polarization and circular polarization can be seen as special cases of elliptical polarization.

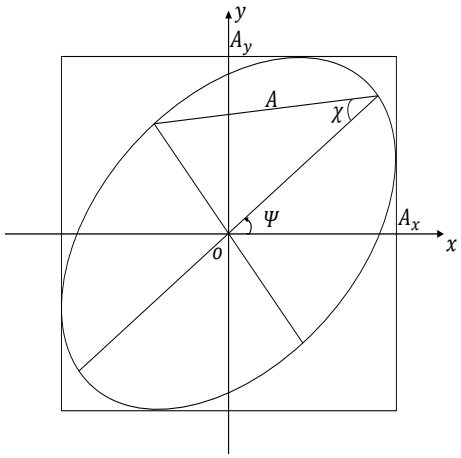

Fig. 2.3. Polarization ellipse in the cartesian coordinate system propagating in z direction.

One parameterization of the elliptical figure specifies the orientation angle Ψ, defined as the angle between the major axis of the ellipse and the x axis along with the ellipticity $\varepsilon = a/b$, the ratio of the ellipse's major to minor axis. The ellipticity parameter is an alternative parameterization of an ellipse's eccentricity $e = \sqrt{1 - b^2/a^2}$, or the ellipticity angle $\chi = \arctan b/a = \arctan 1/\varepsilon$, as is shown in Fig. 2.3.

Besides the geometrical parameters of the ellipse, the "handedness", i.e., whether the rotation around the ellipse is clockwise or counter clockwise, is also necessary to describe a polarization state.

2.2.3 Jones Vector

Full information on a completely polarized state is also provided by the amplitude and phase of oscillations in two components of the electric field vector in the plane of polarization. The amplitude and phase information can be conveniently represented as a two-dimensional complex vector (the Jones vector):

$$\mathbf{e} = \begin{bmatrix} a_1 e^{i\theta_1} \\ a_2 e^{i\theta_2} \end{bmatrix} \tag{2.12}$$

where a_1 and a_2 the amplitude of the wave in the two components of the electric field vector, θ_1 and θ_2 represent the phases. The product of a Jones vector with a complex number of unit modulus gives a different Jones vector representing the same ellipse, and thus the same state of polarization. The physical electric field, as the real part of the Jones vector, would be altered but the polarization state itself is independent of absolute phase. The basis vectors used to represent the Jones vector need not represent linear polarization states (i.e. be real). In general, any two orthogonal states can be used, where an orthogonal vector pair is formally defined as one having a zero inner product.

2.2.4 Four Basic Reflections

One of the many applications of polarimetric SAR data is to find physical interpretations of reflections [45–48]. According to these studies, the reflection of electromagnetic waves on various scatterers can generally be divided into four categories, shown in Fig. 2.4.

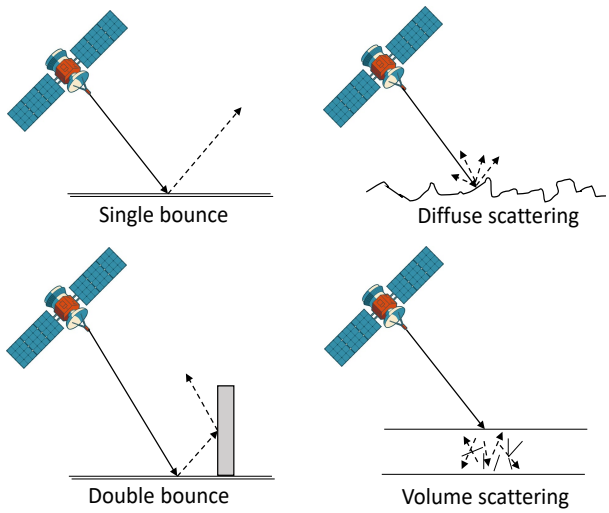

Fig. 2.4. Four different types of radar signal reflecting.

The first one is the single bounce, it is similar to optical specular reflection. This scattering happens on smooth surfaces, such as calm water, dry riverbeds, and flat rocks. Normally, the wave power after this reflection is weak, so the pixels with this reflection are usually dark on the SAR images, unless the surface faces the antenna. The second

one is the diffuse reflection, which occurs on rough surfaces with surface fluctuations much larger than the incident wavelength, such as solidified volcanic lava, wavy water surfaces, and crop-covered surfaces. Part of the wave power returns to the antenna after this reflection, so the pixels are gray or white. The double bounce occurs between two mutually perpendicular surfaces, such as dihedral, urban building walls, and sturdy tree trunks. The reflected energy is very strong and appears light gray to white on the image. The volume reflection occur on thin cylindrical scatterers in random directions, such as areas of vegetation consisting of a large number of tree branches. The reflected energy is weaker, but stronger than a single bounce.

2.3 Synthetic Aperture Radar Interferometry

2.3.1 Theory

The interferogram is the complex product of the master SLC image by the complex conjugate of the slave SLC image. Assuming S_1 and S_2 are pixels at the same position in the master and slave images, the result is:

$$I = S_1 S_2^* \tag{2.13}$$

The phase information of I can be expressed as:

$$\phi_{\text{int}} = \phi_{\text{def}} + \phi_{\text{flat}} + \phi_{\text{atm}} + \phi_{\text{orb}} + \phi_{\text{topo}} + \phi_{\text{noise}} \tag{2.14}$$

where ϕ_{def} is the deformation phase, ϕ_{flat} is the flat earth phase, ϕ_{atm} is the atmospheric phase, ϕ_{orb} is the orbit inaccuracies induced phase, ϕ_{topo} is the topography phase contribution, ϕ_{noise} is from other noise such as misregistration, thermal noise, etc.

As can be seen in Fig. 2.5. A_1 and A_2 are the positions of the satellite antennas during the two imaging. Target P is on the reference plane. The distances from the antenna to target P are R_1 and R_2 respectively. The distances between the antennas and target P' are R_1' and R_2', respectively.

The phase of P is the flat earth phase ϕ_{flat} :

$$\phi_{\text{flat}} = -\frac{4\pi}{\lambda} B_{\parallel} = -\frac{4\pi}{\lambda} B \sin(\theta - \Delta\theta - \alpha) \tag{2.15}$$

The phase of P' is the combination of flat earth phase ϕ_{flat} and topography phase ϕ_{topo} , because P' is located on an undulating surface. The phase of P' can be expressed as:

$$\phi_{P'} = -\frac{4\pi}{\lambda} (R_1' - R_2') = -\frac{4\pi}{\lambda} (\sin(\theta - \alpha)) = -\frac{4\pi}{\lambda} B_{\parallel} - \frac{4\pi}{\lambda} B_{\perp} \Delta\theta \tag{2.16}$$

The topography phase can thus be obtained:

$$\phi_{\text{topo}} = -\frac{4\pi}{\lambda} B_{\perp} \Delta\theta = -\frac{4\pi}{\lambda} \frac{B_{\perp}}{R_1 \sin\theta_0} h \tag{2.17}$$

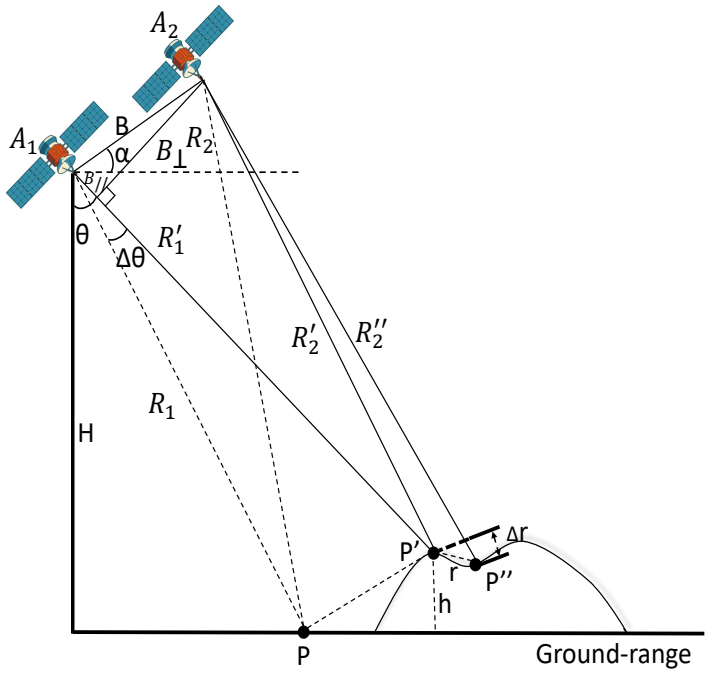

Fig. 2.5. The principle of DInSAR.

2.3.2 Interferometric Decorrelation Sources

As can be seen with Eq. (2.14) that each interferogram contains phases caused by various factors. For terrain displacement measurements, all but deformation and topography phases are defined as decorrelation or phase degradation. The study of these factors is very important because they have a direct influence on the accuracy of ground deformation monitoring. The most used parameter to evaluate the quality of the interferometric phase is the coherence estimator γ [57] [58] [59]:

$$|\widehat{\gamma}(m,n)| = \frac{\left|\sum_{m=0}^{L_1-1}\sum_{n=0}^{L_2-1} S_1(i,j)\cdot S_2^*(i,j)\right|}{\sqrt{\left(\sum_{m=0}^{L_1-1}\sum_{n=0}^{L_2-1}|S_1(i,j)|^2\right)\left(\sum_{m=0}^{L_1-1}\sum_{n=0}^{L_2-1}|S_2(i,j)|^2\right)}} \tag{2.18}$$

where L_1 and L_2 are the window sizes in range and azimuth, respectively, $L = L_1 \times L_2$ is the number of pixels involved in a spatial averaging. The values of coherence vary in the range $[0, 1]$, with two extremes accounting for the two limit situations of data totally uncorrelated and fully correlated, respectively.

Depending on the correlation distance, the sources of error can be divided into two groups.

The large correlation length errors do not have any impact on the coherence:

- Atmospheric artifacts: The different atmospheric layers that the electromagnetic

wave crosses present variations on their refractivity indexes. This modifies its propagation speed, causing a phase change in the interferometric phase term. The typical correlation window of the artifacts is considered 1 km, despite some strong and highly localized phenomena that could reduce this value but do not affect the coherence for its low frequency behavior in space. There is a strong correlation between topography and atmosphere as it can be parameterized through different magnitudes that vary with the height as temperature, water vapor, and pressure.

- Orbit errors: The state vector of each acquisition can be inaccurate and the flat earth component can appear as a phase ramp in the interferogram. However, the new generation of SAR satellites presents a high positioning precision reducing the impact of this kind of error.

The small decorrelation errors have a correlation length smaller than a regular coherence estimation window and so affect the coherence [49, 50]. They can be listed as

- Misregistration: Every image is acquired from a different point of view. If the whole set of images is corregistrated with low accuracy, it would cause this error.
- Geometric decorrelation: The two images of an interferogram are acquired from different looking directions. This means that they observe a slightly different part of the range reflectivity spectrum. This effect is known as range spectrum shift. Consequently, when generating the interferogram the non-common band contributes as noise on the interferometric phase [51]. To avoid this decorrelation, every SLC should be filtered before the generation of the interferograms.
- Doppler decorrelation: It is the azimuth equivalent of the spatial decorrelation. This is caused by the different Doppler centroid frequencies between both acquisitions which induces a frequency shift in the azimuth spectrum from one image to the other.
- Volumetric decorrelation: This term is related to the penetration of the radar waves into the illuminated scene. It analyzes the similarity between the backscattering target response in the vertical direction between the images of the interferogram. Consequently, it will strongly depend on the height target distribution within the resolution cell as well as the radar wavelength and the scattering medium.
- Temporal decorrelation: This term accounts for the possible changes in the properties of the wavelength-scale scatterers of the scene from one image to the other.
- Thermal noise: This term depends on the SNR ratio.

2.4 Differential Synthetic Aperture Radar Interferometry

The process of determining the deformation phase and removing other phase components is DInSAR technology. Suppose P'' in Fig. 2.5 is the position of P' after deformation during the satellite imaging interval, and the distance from A_2 to P'' is R_2'', assuming:

$$R_2'' = R_2' + \Delta r \tag{2.19}$$

In the interferogram, the phase of P'' can be expressed as:

$$\phi_{P''} = -\frac{4\pi}{\lambda}(R_1' - R_2'') = -\frac{4\pi}{\lambda}(R_1' - R_2') - \frac{4\pi}{\lambda}\Delta r \tag{2.20}$$

In the case of not considering the atmospheric phase and noise, the deformation phase can be described as:

$$\phi_{def} = -\frac{4\pi}{\lambda}\Delta r \tag{2.21}$$

And the deformation obtained by DInSAR in Line of Sight (LOS) direction is:

$$\Delta r = -\frac{\lambda}{4\pi}\phi_{def} \tag{2.22}$$

2.5 Persistent Scatterer Interferometry

In this thesis, the PSI processing in Chapter 3, the preparation of SLC data and registration in Chapter 4 and Chapter 5 are accomplished by SUBSIDENCE-GUI, which is the software implementation of the Coherent Pixels Technique (CPT), and developed at Universitat Politècnica de Catalunya (UPC). CPT consists of four main parts: interferogram selection, pixel selection, linear deformation estimation and non-linear deformation estimation [52] [53].

2.5.1 Interferogram and Persistent Scatterer Selection

The interferogram selection block determines the approach of interferogram generation (e.g., the single-master or multi-master approach), and both spatial and temporal maximum baseline lengths allowed for interferograms. Details about this block can be found in [54].

For the persistent pixel selection, the different criteria are basically divided into two families: those working at full-resolutions, like amplitude dispersion, D_A [55] or Temporal Phase Coherence (TPC) [56], and those working with multi-looked interferograms which rely on the coherence, γ. The former is, in principle, more suited to detect deterministic targets while the latter is better suited for distributed ones. The coherence method is introduced in Section 2.3.2.

The amplitude dispersion D_A can be obtained by:

$$D_A = \frac{\sigma_A}{m_A} \tag{2.23}$$

where m_A and σ_A refer to the mean and standard deviation of the temporal amplitude evolution, respectively.

2.5.2 Linear Deformation Estimation Block (LDEB)

Starting from the differential interferograms and a map of selected Persistent Scatter Candidate (PSC)s, the Linear Deformation Estimation Block (LDEB) estimates the linear deformation velocity v and the residual topographic error ε, which is due to inaccuracies of the DEM employed for the generation of differential interferograms. This is accomplished by adjusting a linear model of v and ε to the data (i.e., the phases of differential interferograms). This linear model, on interferogram level, of one pixel can be expressed as

$$\phi_{model} = \frac{4\pi}{\lambda} \cdot T \cdot v + \frac{4\pi}{\lambda} \cdot \frac{B_n}{r \cdot sin(\theta)} \cdot \varepsilon \tag{2.24}$$

where λ is the wavelength, T and B_n are respectively the temporal and perpendicular baselines of the interferogram, r the sensor-to-target distance, θ the local incidence angle.

The LDEB can be divided into three sub-blocks, i.e., *Triangulation*, *Minimization* and *Integration*, as Fig. 2.6 shows:

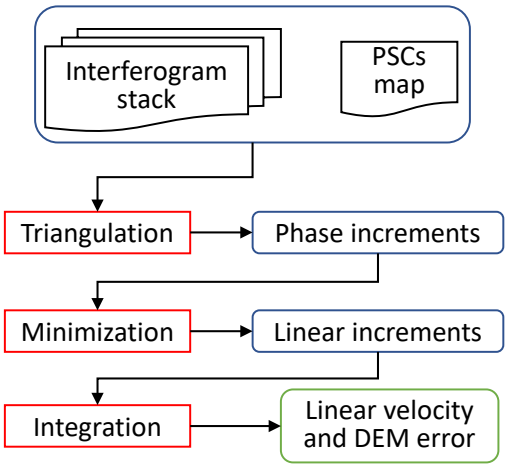

Fig. 2.6. Diagram for the estimation of the linear components of CPT.

1) Triangulation

Due to different phase offsets among differential interferograms, it is very difficult to derive v and ε through (2.24) by using phases of individual pixels, directly. On the other hand, the differential interferometric phases are wrapped and may contain atmospheric artifacts, which can affect the adjustment of (2.24). These problems are overcome by relating neighboring PSCs by the means of Delaunay triangulation, where the PSCs are nodes and links between nodes are arcs. Then phase increments along arcs are calculated on the interferogram level, and the phase increment along $arc_{m,n}$ of the $i-th$ differential interferogram can be expressed as

$$\Delta\phi^i\left(T_i, B_{n,i}, x_m, y_m, x_n, y_n\right) = \Delta\phi^i\left(T_i, B_{n,i}, arc_{m,n}\right) = \phi^i\left(x_m, y_m\right) - \phi^i\left(x_n, y_n\right) \tag{2.25}$$

where the (x_m, y_m) and (x_n, y_n) are locations of the two nodes (i.e., the two selected pixels) forming this arc. In this way, CPT is able to work with interferometric phase

increments rather than absolute phases. On the other side, for the $i-th$ differential interferogram, the linear model along $arc_{m,n}$ can be derived as (2.26) according to (2.24)

$$\Delta\phi^{i}_{model}\left(T_i, B_{n,i}, arc_{m,n}\right) = \frac{4\pi}{\lambda}\cdot T_i \cdot \Delta v\left(arc_{m,n}\right) + \frac{4\pi}{\lambda}\cdot\frac{B_{n,i}}{r_i \cdot sin(\theta_i)}\cdot\Delta\varepsilon\left(arc_{m,n}\right) \quad (2.26)$$

where $\Delta v\left(arc_{m,n}\right)$ and $\Delta\varepsilon\left(arc_{m,n}\right)$ are respectively the linear velocity and DEM error increment along $arc_{m,n}$ [54, 60].

2) Minimization

As $\Delta v\left(arc_{m,n}\right)$ and $\Delta\varepsilon\left(arc_{m,n}\right)$ are constants for all the interferograms, they can be estimated by adjusting $\Delta\phi^{i}_{model}$ to the data $\Delta\phi^{i}$. This is achieved through the minimization of a designed cost function $\Gamma\left(\mathrm{arc}_{m,n}\right)$ as

$$\Gamma\left(\mathrm{arc}_{m,n}\right) = \frac{1}{N_{\mathrm{int}}}\cdot\sum_{i=1}^{N_{\mathrm{int}}}\left|e^{-j\Delta\phi^{i}\left(T_i,B_{n,i},arc_{m,n}\right)} - e^{-j\Delta\phi^{i}_{model}\left(T_i,B_{n,i},arc_{m,n}\right)}\right|^2 \quad (2.27)$$

where N_{int} is the number of interferograms. This minimization is done in the complex plane, thus, any kind of phase unwrapping on interferograms is not required at this step. By doing this minimization from one arc to the other, increments of linear velocity and DEM error of all arcs in the network can be obtained. Meanwhile, the model quality (or model coherence) of each arc is calculated to asses the quality of its related solution (i.e., Δv and $\Delta\varepsilon$). After this, to ensure final products' reliabilities of LDEB, bad quality arcs are eliminated by discarding those with model coherence values below a threshold [54,60].

3) Integration

From the arc increments obtained in the previous step, the linear displacement and DEM error for each selected pixel are derived through an integration process. And then this float solution can be fixed by using one or multiple pixels with known DEM errors and linear velocities as tie points.

2.5.3 Non-linear Deformation Estimation Block (NLDEB)

The LDEB obtains linear component of the displacement, to retrieve a complete estimation, the non-linear deformation has to be retrieved. This is completed by Non-linear Deformation Estimation Block (NLDEB) of CPT, and it consists of two parts, i.e., *atmospheric artifacts estimation* and *temporal non-linear displacement estimation*, as Fig. 2.7 shows.

1) Atmospheric artifacts estimation

The residual interferometric phase ϕ_{res} for each interferogram can be obtained by subtracting the linear components obtained by LDEB from the differential interferometric phase ϕ as

$$\phi_{res} = \phi - \phi_{model} \quad (2.28)$$

where ϕ_{model} is the linear model phase that can be obtained according to (2.24). Then based on ϕ_{res}, the atmospheric phase can be isolated by taking advantage of its different spatio-temporal frequency properties with that of the non-linear deformation component. Particularly, the atmospheric phase can be considered as a spatial low-pass signal in each

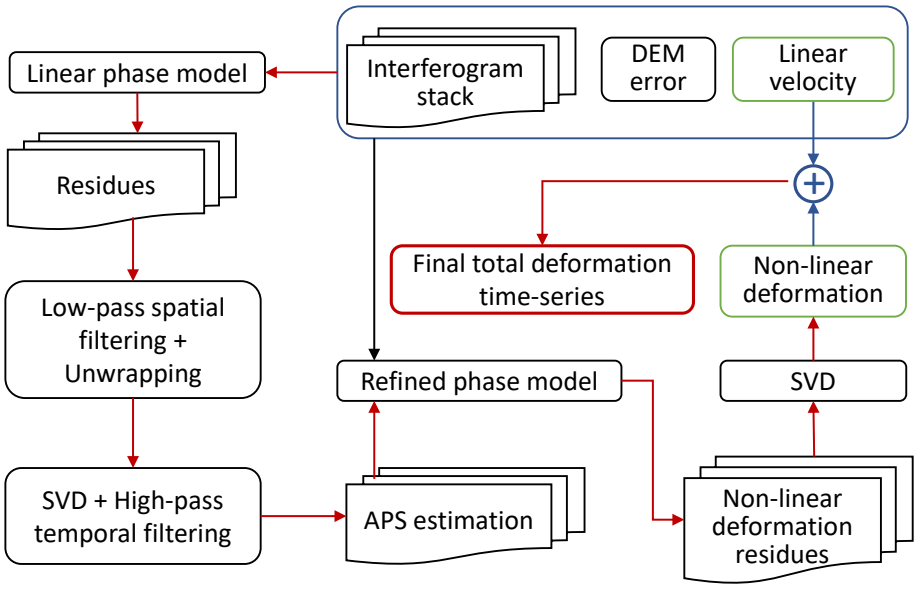

Fig. 2.7. Diagram for the estimation of the non-linear displacement of CPT.

interferogram (or image) and a white noise process in time. On the other hand, the non-linear deformation presents a narrower spatial correlation window compared with Atmospheric Phase Screen (APS) and presents a low-pass behavior in time. It is worth noting that due to the white noise process of atmospheric artifacts, their frequencies fill the whole temporal spectra and, thus, partially overlap with that of non-linear deformation.

Firstly, a low-pass spatial filtering is applied to the interferometric residue of each interferogram and the filtered residue should become

$$\phi_{res,SLR} = \phi_{non-linear,SLR} + \phi_{atm} \tag{2.29}$$

where $\phi_{non-linear,SLR}$ is the Spatial Low Resolution (SLR) non-linear component of the displacement, and ϕ_{atm} the APS as it is assumed to be low-pass in spatial domain and not affected by the spatial filter.

After the spatial low-pass filter, an offset for each $\phi_{res,SLR}$ can be estimated through a histogram analysis. And this new set of residual interferometric phases is easy to unwrap since they should be very smooth in spatial as almost all fringes have been removed. Once unwrapped the phase and removed an offset for each one of the residual interferograms, the Singular Value Decomposition (SVD) is applied to transform the phase from differential time domain to the image time one.

After the above inversion, the result is integrated with respect to the first image. And then a high-pass temporal filter is employed to extract the image level APS term. Until now, the atmospheric phase ϕ_{APS} for each interferogram can be calculated. It is worth noting that the high-pass cut frequency for the temporal filter should be set as the highest possible frequency of the non-linear displacement.

2) Temporal non-linear displacement estimation

Once the APS has been estimated, a new residual interferometric phase free of atmospheric artifacts can be calculated as

$$\phi_{res,APSfree} = \phi - \phi_{model} - \phi_{APS} - \phi_{off} = \phi_{non-linear} + \phi_{noise} \tag{2.30}$$

where ϕ_{APS} and ϕ_{off} are the APS and phase offset estimated in the previous step, $\phi_{non-linear}$ the non-linear deformation component, and ϕ_{noise} the interferometric phase noise term. Then by employing a new SVD process on $\phi_{res,APSfree}$ of all the interferograms, the temporal phase profile corresponding with non-linear deformation can be retrieved and converted to displacement. Finally, the total deformation is obtained by adding the linear and non-linear terms together, as it is shown in Fig. 2.7.

2.6 The Probability Integral Method (PIM)

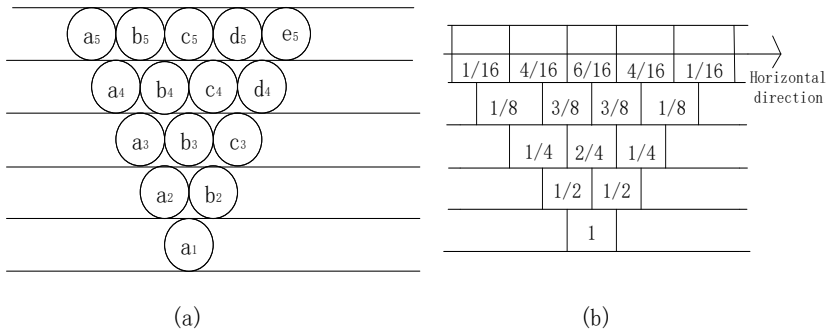

Fig. 2.8. Theoretical model of particulate medium. (**a**) Theoretical model.(**b**) Distribution of particulate movement probability.

The probability integration method, firstly proposed by Polish scholars, is a mining subsidence simulation method based on stochastic medium theory [61]. It considers the movement of particles, such as sand or tiny rock masses, as a random event, which makes the relationship between particles irrelevant. The mining area can be divided into a number of differential units with the assumption that they are mined. The total impact of the complete mining on the rock formation and the surface can be regarded as the integral of the small impact generated during the mining of the differential units. As shown in Fig. 2.8a, when the ball (named a_1) on the first floor is taken away, one of the balls on the second floor (a_2 and b_2) will fall, so the probability of falling for each of the two balls is 1/2. Then, one of the balls on the third floor will fall, and the falling probabilities for each of the three are 1/4, 2/4, and 1/4, respectively (in Fig. 2.8b).

On this basis, the differential equation of the probability distribution function of the sinking event is obtained. The surface subsidence at point x is,

$$W(x) = \frac{W_{max}}{2} \cdot [erf(\frac{\sqrt{\pi}}{r} \cdot x) + 1] \tag{2.31}$$

Where $W(x)$ stands for the subsidence value at x; W_{max} is the max value of the subsidence curve; r is the major influencing radius; erf is the error function, and $erf = \frac{2}{\sqrt{\pi}} \int_0^x e^{-\eta^2} d\eta$. The location of $x = 0$ is the coal mining boundary.

The integral can be extended to two dimensions. The length and width of the working surface are l and L, respectively, then the subsidence value of point (x, y) on the surface is,

$$\begin{aligned} W(x,y) =& W_{\max} \times \frac{1}{2}\left\{\left[\operatorname{erf}\left(\sqrt{\pi}\frac{x}{r}\right)+1\right] - \left[\operatorname{erf}\left(\sqrt{\pi}\frac{x-l}{r}\right)+1\right]\right\} \\ & \times \frac{1}{2}\left\{\left[\operatorname{erf}\left(\sqrt{\pi}\frac{y}{r}\right)+1\right] - \left[\operatorname{erf}\left(\sqrt{\pi}\frac{y-L}{r}\right)+1\right]\right\} \\ =& \frac{1}{W_{\max}}[W(x) - W(x-l)][W(y) - W(y-L)] \end{aligned} \tag{2.32}$$

The parameters in Eq. (2.32) can be calculated as follows,

$$\begin{cases} W_{\max} = qm\cos\alpha \\ r = \frac{H_0}{\tan\beta} \\ r_1 = \frac{H_1}{\tan\beta} \\ r_2 = \frac{H_2}{\tan\beta} \\ \theta = 90^o - k\cdot\alpha \\ l = L_1 - 2S_0 \\ L = \frac{(L_2 - S_1 - S_2)\sin(180^o - \alpha - \theta)}{\sin\theta} \\ W(x) = \frac{W_{max}}{2}\cdot[erf(\sqrt{\pi}\cdot\frac{x}{r})+1] \\ W(x-l) = \frac{W_{max}}{2}\cdot[erf(\sqrt{\pi}\cdot\frac{x-l}{r})+1] \\ W(y) = \frac{W_{max}}{2}\cdot[erf(\sqrt{\pi}\cdot\frac{y}{r_1})+1] \\ W(y-L) = \frac{W_{max}}{2}\cdot[erf(\sqrt{\pi}\cdot\frac{y-L}{r_2})+1] \end{cases} \tag{2.33}$$

In Eq. (2.33), q is the subsidence coefficient, m is the mining thickness, α is the dip angle of the coal seam, H_0 is the average distance of the coal seam from the ground surface, $\tan\beta$ is the tangent of main effect angle, r_1 is the main influence radius of the downhill direction, r_2 is the main influence radius of the uphill direction, θ is the propagation angle of extraction, k is the propagation coefficient of extraction, L_1 is the length of the mining face, L_2 is the width of the mining face, l and L are the equivalent length and width of the mining face, S_0, S_1, S_2 are the deviations of the inflection point.

2.7 Offset Tracking (OT) Principle

The OT method itself is inspired by traditional optical image registration algorithms. As shown in Fig. 2.9, OT obtains the offset by matching a reference template and a search template of the same size. The reference template in the reference SAR image is fixed and the search template is moved in the search SAR image to find the window that best matches the reference template. The parameter describing the similarity between the reference template and the search template is the cross correlation coefficient, and can be

calculated by Eq. (2.34):

$$\rho(x,y) = \left| \frac{\sum_u \sum_v \left(I_1(x,y) - \bar{I}_1\right)\left(I_2(x+u,y+v) - \bar{I}_2\right)}{\sqrt{\sum_u \sum_v \left(I_1(x,y) - \bar{I}_1\right)^2 \sum_u \sum_v \left(I_2(x+u,y+v) - \bar{I}_2\right)^2}} \right| \tag{2.34}$$

where $\rho(x,y)$ represents the correlation coefficient. (x,y) are the coordinates of the center pixel of the reference template in the reference image. (u,v) indicate the movements of the search template. $(x+u,y+v)$ are the coordinates of the center pixel of the search template in the search image. I_1, I_2 represent the pixel intensity in the reference template and the search template, respectively. $\bar{I}_1$, $\bar{I}_2$ indicate the mean of the pixel intensity in the corresponding template window. The (u,v), which can lead to the maximum $\rho(x,y)$, is the offset of the pixel in the center of the reference template.

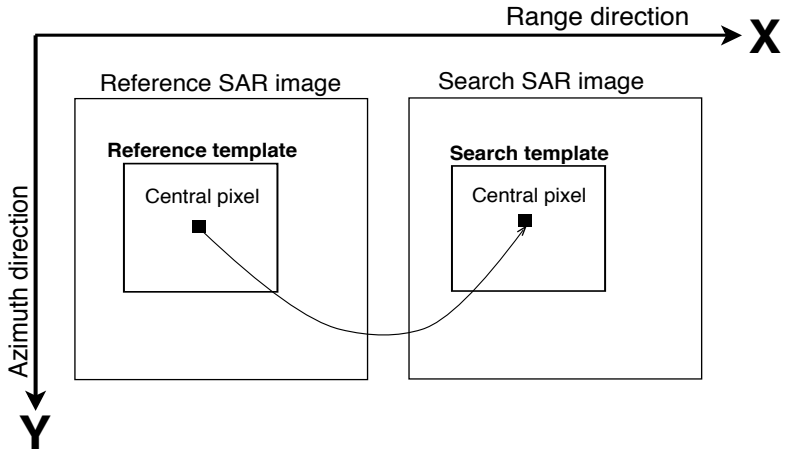

Fig. 2.9. The principle of pixel tracking.

The pixel-tracking method is simple and computationally expensive. The computation burden can be reduced by performing cross correlation in the frequency domain. The monitoring accuracy is affected by factors such as pixel size, surface scattering properties, template window size, and cross correlation factor. This method cannot be performed if the surface scattering signal has no contrast or the contrast is very weak, such as a flat desert without rocks or plants. The pixel-tracking method is not restricted by the deformation gradient. Besides, it has strong phase decorrelation immunity. These two advantages allow OT complements the InSAR method based on phase unwrapping.

3

Chapter 3

EMDD-PSI: External Model Deformation Decomposition based Persistent Scatters Interferometry

As introduced in Chapter 1, several methods have also been proposed to improve the performance of PSI in large gradient deformation monitoring. Inspired by the afore mentioned methods and also in order to avoid the above constraints, in this Chapter a new method with less parameter dependence and better non-linear retrieving ability is presented, named as External Model Deformation Decomposition based Persistent Scatters Interferometry (EMDD-PSI). To assess the performance of the proposed EMDD-PSI, it has been tested with 14 Radarsat-2 images over Fengfeng mining area (China). The benefits of the proposed EMDD-PSI have been evaluated and discussed. This Chapter is organized as follows. Section 3.1 describes the principals and detailed procedures of the proposed EMDD-PSI. In Section 3.2, data sets and study area are briefly introduced. Then, the results obtained with the proposed and traditional methods are compared with the ground truth in Section 3.3. In Section 3.4, some procedures and results are discussed. Finally, conclusions are made in Section 3.5.

3.1 Methodology

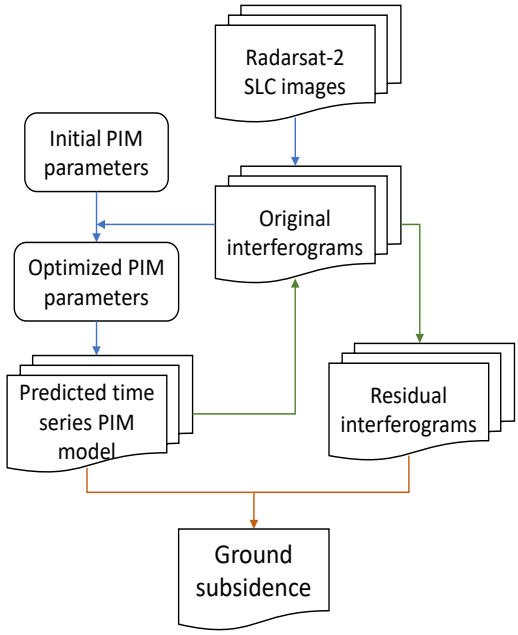

Fig. 3.1. Overall processing scheme.

When PSI techniques try to monitor deformations with large gradients in a mining area, one of the challenges is the error caused by the so-called *phase saturation*. When the LOS deformation difference between two adjacent pixels exceeds $\lambda/4$ [62], with λ the wavelength of the carrier frequency, the correct deformation cannot be retrieved. As mentioned in Chapter 1, a proper model of the subsidence phenomena can be used to reduce the phase difference among adjacent pixels. However, inaccurate model parameters may introduce additional fringes in the interferograms instead of reducing them.

In this section, a method is proposed to increase the accuracy of PSI monitoring of large gradient deformations by reducing the fringes of the interferograms, as shown in Fig. 3.1. For the sake of clarity, the differential interferograms are referred to as original interferograms. The subsidence maps generated by the PIM model are called the model simulated maps. The proposed approach mainly consists of three steps: a) optimize the adjustment of the model parameters using individually all or a subset of the original interferograms and then generate model simulated maps, b) remove or reduce the deformation fringes in all interferograms with the simulated maps and c) do the PSI processing to the cleaned interferograms and obtain the residual deformation not considered by the model, and finally generate the deformation time-series adding the model simulated maps to the calculated residual deformations.

a) Parameter optimization

The purpose of parameter optimization is to make the model simulated deformation

as close as possible to the original interferograms by adjusting the parameters of the PIM model. Generally, there are two ways to obtain these parameters. One is by inversion according to the ground subsidence value, the subsidence can be acquired by measurement of DInSAR, GPS or leveling. While the other is from a-priori knowledge. All the parameters are listed in Table 3.1 with their obtaining methods and effects.

Obviously, not all the parameters need to be optimized. The parameters obtained from the measurements should not be changed because they represent the actual situation of the working panel. According to [63], different working panels should be simulated with different PIM parameters obtained by a-priori knowledge because of their different geological structure and mining conditions. Similarly, not all the parameters from a-priori knowledge need to be optimized either. Here mainly two factors are considered, one is due to the simplification of the model, the other is 'the curse of dimensionality'.

Due to the simplification of the model, the coal seam is considered horizontal. Under these circumstances, some parameters do not need to be optimized anymore, such as the maximum sinking angle, which represents the influence caused by the tilt of the coal seam. When the coal seam is horizontal, the maximum sinking angle is 90°. Also, since the horizontal deformation is ignored, the horizontal movement coefficient is not necessary as its role is to calculate the maximum horizontal movement.

Inflection point offsets are used to determine the horizontal distance between inflection points and the working panel boundaries. The tangent of main effect angle represents the ratio between the depth and the distance from basin center to the inflection points. Once the coordinates and depth of the working panel is determined, these parameters will have the same influence on the basin, i.e. they are in same dimensionality. The four inflection point offset correspond to the four boundaries of the working panel. Since the model is considered symmetrical, it is enough to just optimize the tangent of the main effect only.

Table 3.1: Obtaining method and effect of PIM parameters.

Parameters of PIM	method of obtaining	Effect
Coordinates of the working panel	measurement	Description of the location of the mining activity
Mining depth	measurement	Description of the depth of the mining activity
mining thickness	measurement	Description of the thickness the of mining coal seam
coal seam dip angle	measurement	Description of the angle between coal seam and horizontal plane
strike azimuth	measurement	Description of the mining direction
sinking coefficient	prior knowledge	Determining the maximum deformation value of the basin
horizontal movement coefficient	prior knowledge	Determining the horizontal deformation value
tangent of main effect angle	prior knowledge	Determining the ratio of mining depth to major influencing radius
inflection point offsets	prior knowledge	Determining the horizontal distance between mining boundary and inflection point
propagation angle of extraction	prior knowledge	Description the relationship between inflection point offsets and mining depth
maximum sinking angle	prior knowledge	Determining the relationship between the working panel and the point on the ground surface with maximum subsidence value

Two additional offset parameters are added. They are not PIM parameters, but they are used to correct the subsidence location to compensate for the impact of faults and adjacent goafs. With the three PIM parameters, there are a total of five parameters participating in the optimization. These five parameters are named as Parameters that Can Be Optimized (PMCBO).

After the PMCBOs are defined, the next step is its optimization to better match the model simulated deformation to the original interferograms. A brute force approach is used, i.e. given a search range (max and min values) and step size for the parameters, the values of all possible combinations are feeded into the PIM model to get all possible simulated maps. Then the model simulated maps are transformed from deformation to interferometric wrapped phases in radar coordinates to be consistent with the original interferograms. After that, the phase difference between the simulated model maps and the original interferograms is calculated to measure the degree of compliance of the model for each parameter combination.

In addition, only those PS pixels with a coherence beyond 0.6 and located within the PIM simulated basin are used to calculate the phase difference. The average of the absolute values of the phase differences is considered the metric to evaluate the agreement between the simulated model maps and the original interferograms.

b) Fringes reduction

The purpose of reducing the number of fringes in the interferograms is to improve the accuracy and reliability of the solution by reducing phase ambiguities among adjacent points in the PSI processing. After obtaining the optimized PMCBOs, model simulated maps are generated using PIM. After converting the model simulated subsidence values into interferometric phases in radar coordinates, the cleaned interferograms are obtained by subtracting the model phase from the original interferograms. The cleaned interferograms are also mentioned as residual interferograms. Ideally, if the model simulated maps were absolutely consistent with the original interferograms, that is, the phase difference between both would be zero and all the fringes in the original interferograms would have been removed. This situation is clearly unrealistic as both the model and their parameter adjustment present limitations. In fact, the objective is to reduce the fringes under an acceptable level not to remove them completely.

c) Deformation retrieval

CPT is applied to obtain the time-series deformation and subsidence velocity from the residual interferograms, which is called the residual deformation information. This deformation is added to the one simulated by the model to determine the complete deformation time-series.

3.2 Study Area and Data Set

3.2.1 Study Area

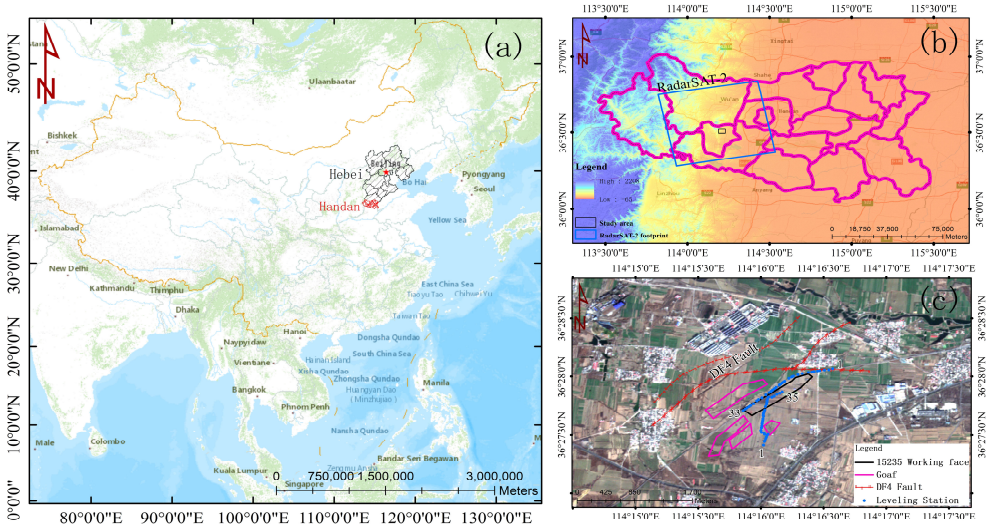

Fig. 3.2. Study area overview. Figure (a) shows the location of the study area.Figure (b) shows the coverage of RADARSAT-2 images and the altitude of the study area. Figure (c) shows the goafs, working faces, faults and leveling stations. The numbers around blue points indicate the name of the leveling station.

The 15235 working face of the Jiulong mining area is selected as test site. It is located in Fengfeng coalfield, Hebei Province (China), and surrounded by villages, industrial plants and farmlands. The working face presents a length of 935 m in the strike direction, a length of 142 m in the dip direction, an average coal mining thickness of 4.5 m, and an average mining depth of 740 m. The inclination of the working face is between 12 ° and 15 ° with an average of 14 °. In the south of the study area, there is the 15221N working face goaf, in the north is the northern boundary of the minefield, in the west is the DF4 fault and the Daqing waterproof coal pillar. Due to the proximity to the DF4 fault, there may be some small faults in the west of the 15235 working face.

3.2.2 Data Set

14 ascending Radarsat-2 Stripmap images were collected from April 4th, 2015 to March 5th, 2016, with a HH polarization. The incidence angle ranges from 33.9 ° to 37.1 °. The pixel resolution is approximately 2.66 m in the range direction and 2.91 m in the azimuth one. Radarsat-2 works at C-band and has a revisit period of 24 days. The wavelength of the carrier is 5.55 cm. DEM with pixels spacing of 10 m from the Shuttle Radar Topography Mission (SRTM) is used to help with coregistration and remove the topographic phase.

The characteristics of the area of interest, barely urbanized and covered with high vegetation, and the strong gradient deformation introduces a severe constraint on the maximum temporal baseline that can produce useful interferograms. The interferograms are generated using a Delaunay triangulation, where the maximum temporal baseline has been set to 48 days while the maximum spatial baseline to 360 m. A total of 16 interferograms have been generated whose the details are summarized in Table 3.2.

Table 3.2: Parameters of interferogram pairs.

Nnmber	Interferograms Pairs	Spatial Baseline	Time Baseline
1	20150404–20150428	−99.1 m	24 d
2	20150404–20150522	83.8 m	48 d
3	20150522–20150615	50.1 m	24 d
4	20150615–20150802	−94.2 m	48 d
5	20150709–20150826	−116.9 m	48 d
6	20150826–20150919	109.1 m	24 d
7	20150826–20151013	8.9 m	48 d
8	20150919–20151013	−102.0 m	24 d
9	20151013–20151106	−50.6 m	24 d
10	20151013–20151130	−51.0 m	48 d
11	20151106–20151130	−10.1 m	24 d
12	20151106–20151224	−30.0 m	48 d
13	20151130–20151224	−20.5 m	24 d
14	20151130–20160117	30.5 m	48 d
15	20151224–20160117	−47.4 m	24 d
16	20160117–20160305	−39.0 m	48 d

In order to validate the DInSAR monitoring result, leveling data provided by China University of Mining and Technology (CUMT) is used as ground-truth. It was collected on April 24th, 2015 and March 4th, 2016, and the accuracy of the leveling data is better than 1 mm. The position of the leveling stations are shown in Fig. 3.2 as blue points. The station number gets higher from northeast to southwest in the strike direction and from south to north in the dip direction.

3.3 Results

In this section, the performance of the proposed method is evaluated in terms of the consistency of the model simulated maps and the original interferograms, the comparison with the traditional PSI processing and, finally, the verification with the available ground-truth data.

SUBSIDENCE-GUI, the software implementation of the CPT developed at UPC, is used to perform the PSI processing. The details are introduced in Section 2.5. For the

pixel selection step, the surface of the mining area is often covered by soil, so coherence has been used to select the pixels with a 3×3 multilook, in order to preserve resolution, and a mean coherence threshold of 0.5. The phase standard deviation σ of the selected coherence threshold and multi-look is 32°.

3.3.1 Consistency of the Model Simulated Deformation Maps with the Original Interferograms

Fig. 3.3 shows the wrapped phase maps of the 16 original interferograms generated from the 14 SLC images (the first and fourth columns), simulated by PIM (the second and fifth columns) and residual interferograms (the third and sixth columns), in radar coordinates.

Some of the original interferograms clearly show that there are two adjacent subsidence basins. They are caused by working panels 15235 and 15221N. Compared with Universal Transverse Mercator (UTM), the radar coordinate system is upside down. Therefore, in Fig. 3.2 and Fig. 3.4, 15235 is located above 15221N, while in Fig. 3.3, 15235 is below 15221N.

It can be seen from the original interferograms that the sinking basin induced by the 15235 working face has an offset towards adjacent basins and faults. The borders of the two mining basins are even connected together. In some interferograms fringes are barely visible due to the poor quality of the phase, which is heavily decorrelated. Although there are only two different temporal baselines (24 days and 48 days) in the data set, the number of interferometric fringes varies widely along time, highlighting the non-linear behavior of the subsidence pattern.

Some strange horizontal thick fringes appears in the interferogram 20151224-20160117. Four possible reasons are examined: DEM error, ground surface change, groundwater caused deformation and atmospheric artefacts. DEM is checked and its shape does not match these features. Ground surface did not change so much during that time. There are some villages in this area and the domestic water of local people is from groundwater (it is normal in China). The decline of the groundwater may cause subsidence like this. But if these fringes were caused by groundwater, the mining activities should affect the groundwater, and the subsidence basins caused by groundwater and mining will become a large one, instead of two separate basins. Since other possibilities are ruled out, and the strange area is large enough (at least 3 km^2), the most likely reason for the strange fringes are atmospheric artifacts.

The model simulated maps are first back-geocoded from UTM coordinates into radar coordinates, then phase wrapped. As it can be seen in Fig. 3.3, in contrast to the original interferograms, the simulated basins do not develop towards surrounding basins and faults, and they have the characteristics of a regular shape and neat boundary, while the rest has a phase equal to 0. This is because the model considers the rock formations above the working panel to have the same mechanical properties, and the information of other goafs and faults is not considered.

In the residual interferograms, it can be seen that there are still small residual phases distributed around the 15235 basin because the upper basin and faults are not considered in the model. In general, the number of fringes has been reduced in the interferograms showing clear and significant fringes. It can be clearly seen that the number of fringes in

the lower basin has been reduced, which proves the accuracy of the model despite their boundaries were not perfectly adjusted. It has to be kept in mind that the goal was to reduce the high frequency fringes but cancelling them completely was not compulsory.

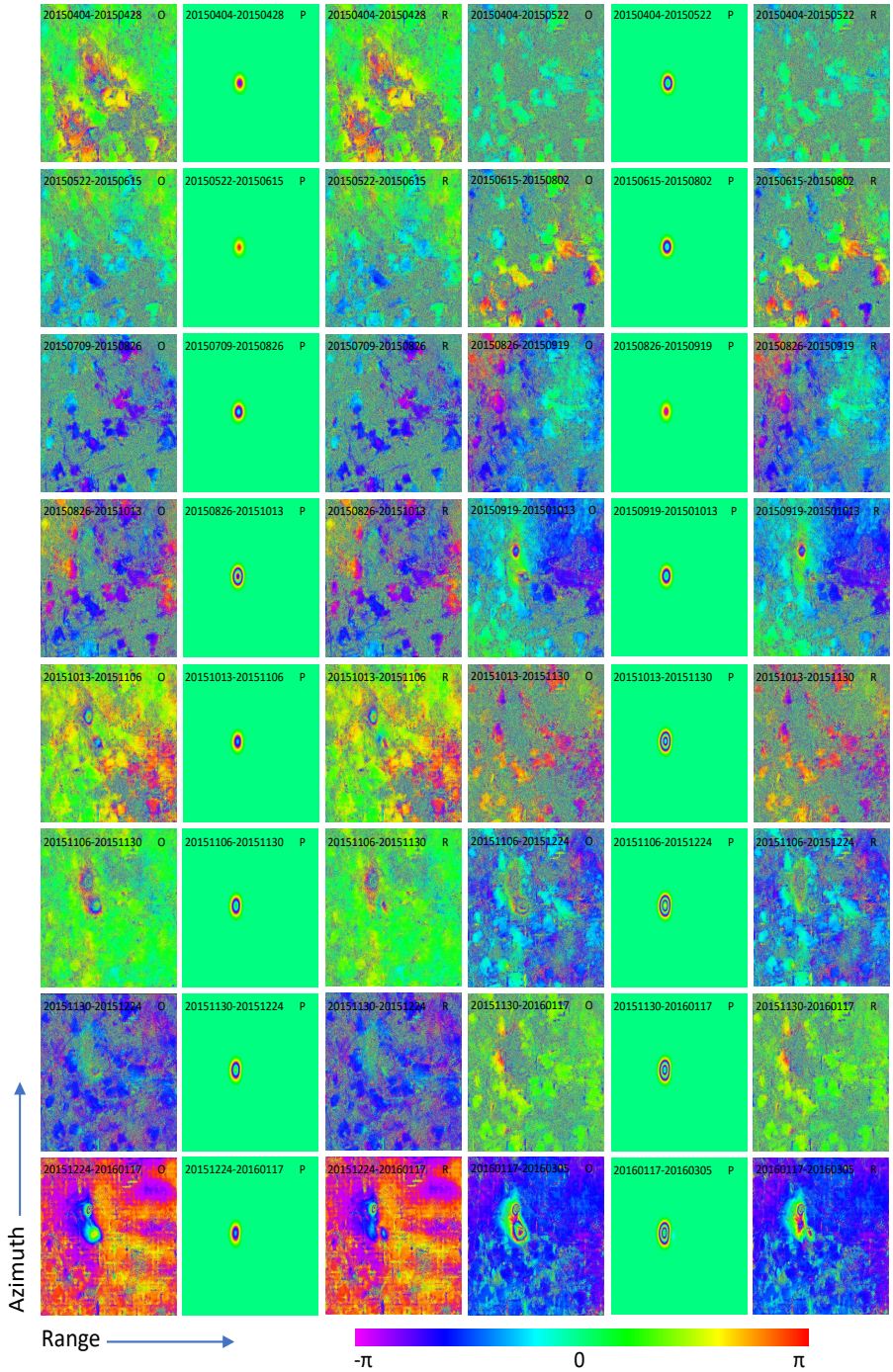

Fig. 3.3. Phase maps of 16 original interferograms, model simulated deformation and residual interferograms in image coordinates. The acquisition dates of master image and slave image of each interferogram is on the top, O indicates original interferogram, P means the phase map is from PIM model and R represents the residual interferogram.

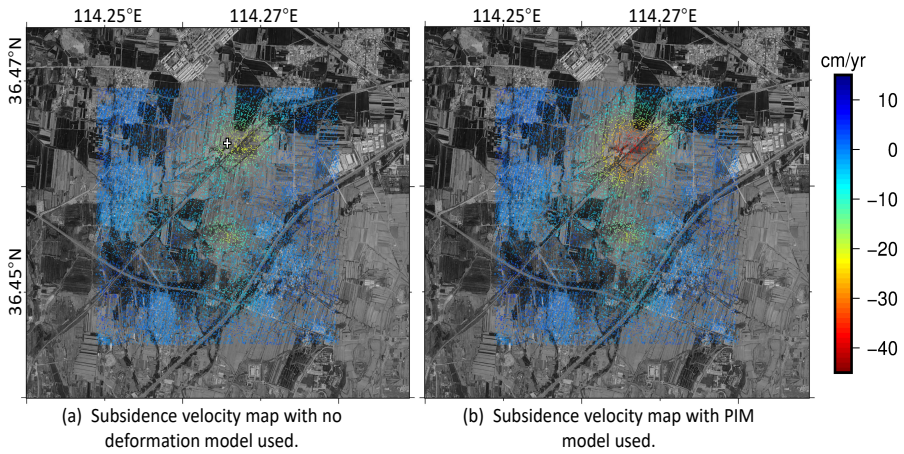

Fig. 3.4. Deformation velocity maps of the study area in vertical direction. The white cross symbol is the point with maximum deformation velocity.

3.3.2 Comparison with the Traditional Persistent Scatters Interferometry (PSI) Processing

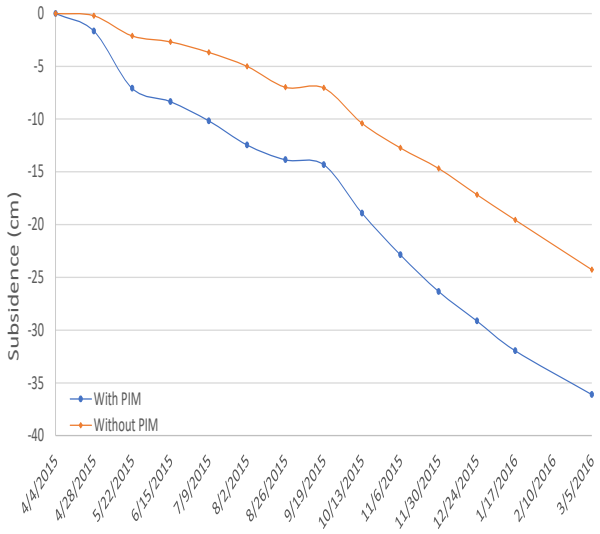

Fig. 3.5. Time series subsidence in LOS direction at the location with the maximum subsidence value.

Fig. 3.4 shows the subsidence vertical velocity maps obtained with SUBSIDENCE-GUI in UTM coordinates without and with the deformation model. The upper subsidence basin, caused by the mining of 15235 working face, is the one that has been modeled. By comparing the two figures, it can be seen that the PSs density and location are almost

identical in both cases. The difference of mean coherence of the original and cleaned interferograms in the subsidence area is only 0.03, which is too small to influence the pixels selection step. The reason that the coherence has only a small improvement after fringes removal is because the frequency of the fringes caused by mining are not extremely high and the multi-look small, only 3×3. The key contribution of PIM model in this case is to compensate the periods influenced by decorrelation instead of coherence improvement.

The characteristics of the mining area make it not specially suited for PSI processing. In order to have an acceptable density of pixels, the coherence threshold has been set to 0.5, a lower value than usual. This makes the results to be noisier but this loss of precision is compensated by the large values of deformation. Results in stable areas are almost identical with both approaches. As expected, the density of selected points is higher in urbanized areas than in rural fields. The subsidence basins in the two figures are not symmetrical. There is an offset to the southwest direction due to the influence of nearby faults and adjacent goafs. The subsidence basin induced by 15235 in Fig. 3.4 (b) is larger in extension and deformation values than in Fig. 3.4 (a). The rationale of the differences will be detailed in Section 3.3.3

The comparison of the time-series deformation obtained with the two methods in the location with the maximum subsidence velocity is shown in Fig. 3.5. As it can be seen, the two time-series present the same trend but it is steepest when using the subsidence model. They both have a slowly deformation rate tending to a stabilization from August 26th to September 19th, 2015. When the subsidence accelerates, from September 19th, 2015 to March 5th, 2016, the orange curve is almost a line, while the blue one shows that the subsidence rate starts to slow-down. The behaviour of the blue line is consistent with the law of sinking after the surface point is affected by underlying mining. The deformation time-series are better retrieved thanks to the fringe reduction provided by PIM, which considers the non-linear deformation.

3.3.3 Leveling Data Verification

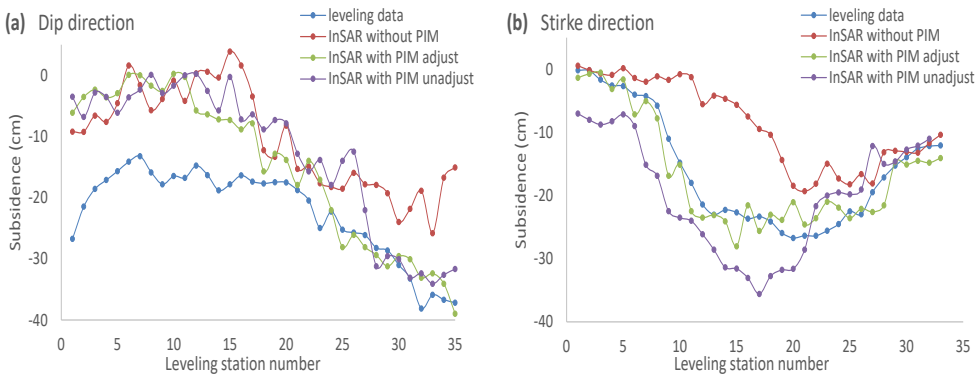

Fig. 3.6. Results comparison of different methods.

The deformations obtained by PSI with and without PIM assistance are compared with leveling data in Fig. 3.6. In the plots, the deformation retrieved with PIM without parameter optimization is also included for comparison purposes. In order to be consistent with the leveling data, the deformation results have been transformed from LOS to vertical direction. As the subsidence measured by leveling is from April 24th, 2015 to March 4th, 2016, the deformation monitored by PSI has been limited to the period from April 28th, 2015 to March 5th, 2016. It can be seen that, the green and purple curves, PSI with PIM, decrease faster than the red one, PSI with no model, in both dip and strike directions. This is because, compared to traditional PSI, PIM reduces the number of interferometric fringes in the sinking area, that is, the phase gradient. Thus, as the phase ambiguity of the relationship among PS points is reduced, the network is more robust. Besides, part of the deformation is a-priori retrieved by the external model. Therefore, the PSI processing can achieve better results.

There are some differences with the leveling stations 1 to 19 in Fig. 3.6(a) because the subsidence in the dip direction is also affected by another working face not included in the model and so the subsidence is clearly underestimated. This results highlights the importance on the selection of the proper model. Meanwhile, it can be seen that the purple curve is shifted towards north and east compared to the green curve due to the setted offset in parameter optimization. As it can be seen in Fig. 3.6(b), the purple curve has a larger subsidence value than the green and blue ones. This is due to the unadjusted parameters used that generate a basin with subsidence larger than the actual one. After subtracting the over-modeled deformation, PSI obtains uplifts in the subsidence area when retrieving deformation from the residual interferograms. But the over-modeled deformation is so large that there is ambiguity among PSs in the residual interferograms, therefore the uplifts cannot be obtained completely. Then, the retrieved uplifts are not enough to neutralize the over-modeled deformation, so the final deformation is larger than it actually is. The purple curve in Fig. 3.6(a) has no greater subsidence value because the basin produced by unadjusted parameters is shifted away from the leveling station, so the deformation value at the station becomes smaller.

Finally, the Root Mean Square Error (RMSE) of the three processing strategies is calculated according to the ground truth. The RMSE of PSI without modeling, with non-optimized and with optimized modeling are 11.47, 9.34 and 7.43, respectively. This means that the accuracy of PSI with non-optimized modeling has increased by a 18.6% compared to conventional PSI, the accuracy of PSI with optimized modeling has increased by a 35.2% compared to conventional PSI, and the accuracy of PSI with optimized modeling has increased by a 20.4% compared to PSI with non-optimized modeling. The ground truth demonstrates the effectiveness of the proposed method.

3.4 Discussion

3.4.1 Analysis of the Relationship among PMCBOs

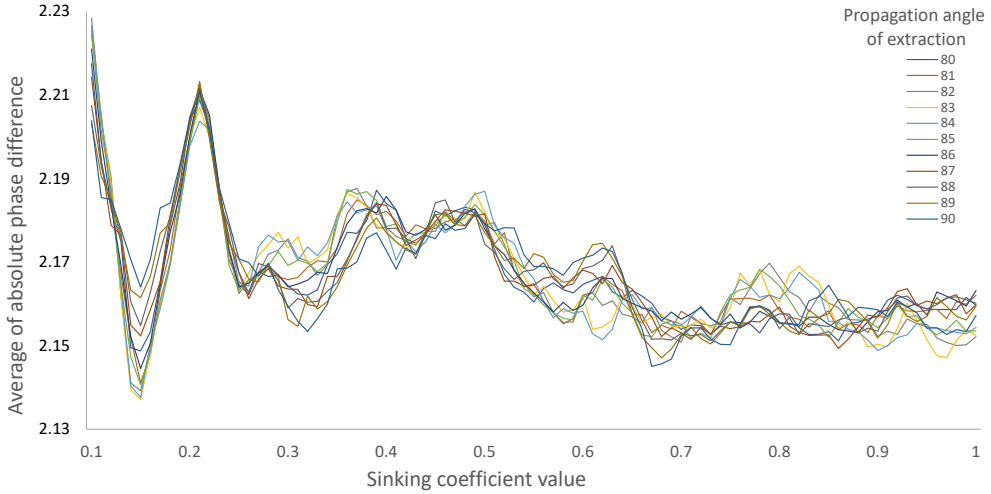

Fig. 3.7. Parameter variation law.

In order to understand the effect of the parameters in the final results, Fig. 3.7 shows the relationship between the error factor (the average of the absolute values of the phase differences over the whole interferogram) and the sinking coefficient when the propagation angle of extraction changes. The searching range is expanded to $0 \sim 1$ and the step size is reduced to 0.01. It can be seen that as the sinking coefficient increases, the factor gradually decreases and its fluctuation becomes smaller. Taking the curve of the propagation angle of extraction of 90^o as an example, the minimum values are obtained periodically at 0.15, 0.32, and 0.67, respectively. This periodic phenomenon is due to the use of the wrapped phase for verification. The sinking coefficient controls subsidence value, after transforming subsidence into wrapped phase, the simulated deformation from the integer multiples values will have similar phases. Therefore, once one value of sinking coefficient can minimize the error factor, so as its integer π multiples. This miscalculation can be avoided by setting the minimum estimated sinking coefficient as the final optimized result.

When the the propagation angle of extraction is 83^o, the sinking coefficient which minimizes the error factor is 0.15. Fig. 3.8 shows the relationship between the error factor and the propagation angle of extraction when the sinking coefficient is 0.15. It can be seen that as the propagation angle of extraction increases, the error factor first decreases and then increases, and the minimum value is obtained when the mining influence propagation angle is 83^o. It is worth noting that in Fig. 3.7, not all curves are at their minimum value when the sinking coefficient is 0.15. For example, when the mining influence propagation angle is 89^o, the sinking coefficient that minimizes the average of the phase difference is 0.68. When the propagation angle is 90^o, the sinking coefficient which minimizes the average value of the phase difference is 0.67. It is indicated that the optimal value of

one parameter is affected by other parameters, which is why the brute force is used in this section to optimize all values at the same time, instead of determining the optimal parameters in turn, although that would cause a lower computational burden.

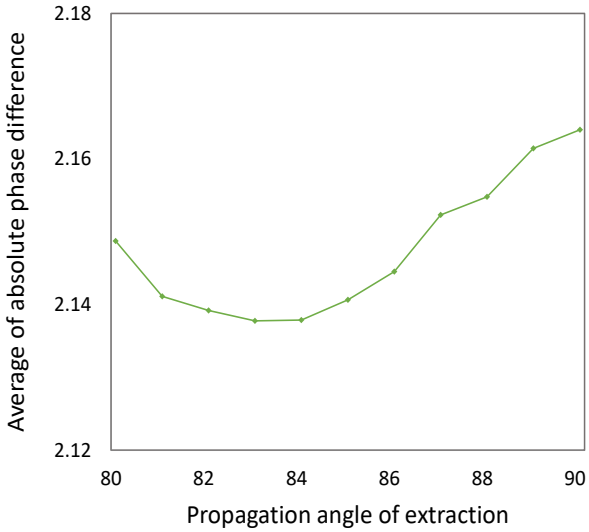

Fig. 3.8. Relationship between phase difference and propagation angle of extraction.

3.4.2 Analysis of the Parameter Optimization

The searching range, step size and final optimization results of PMCBOs are shown in Table 3.3. The setting of step size and search range need to consider the balance between the calculation burden and the experiment accuracy.

It can be seen that, compared with the parameters before optimization, the sinking coefficient, tangent of the main effect angle and the propagation angle of extraction become smaller. Offset x and y change to 150 and 90 from 0, means the basin shifts 150 m towards west and 90 m towards south.

The subsidence coefficient represents the ratio of the surface subsidence value to the thickness of the coal seam. The non-optimized sinking coefficient represents the ratio of the sinking value to the thickness of the coal seam when the ground surface becomes stable and no longer sinks. In this experiment, the working surface was still being mined during SAR imaging. The surface deformation during this time period was still continuous and did not reach stability. Therefore, the surface deformation value was smaller than it is when it is stable, so the corresponding sinking coefficient should be smaller.

Table 3.3: Optimization of PMCBOs.

	sinking coefficient	tangent of main effect angle	propagation angle of extraction	offset x	offset y
Maximum value	0.5	1.9	89	180	180
Minimum value	0.05	1.6	81	0	0
Step size	0.05	0.05	2	30	30
Number of calculations	10	7	5	7	7
Optimal solution	0.15	1.75	83	150	90
Before optimized	0.68	2	85	0	0

The subsidence basin has expanded due to the influence of the surrounding faults and goafs. The tangent of main effect angle represents the relationship between the depth of the mining and the radius of the sinking basin. According to Eq. (2.33), $r = H/\tan\beta$, the tangent of the main effect angle becomes smaller, means the sinking basin becomes larger. This is consistent with the actual situation.

When the inclined coal seam is mined, the inflection point is not directly above the calculation boundary, but it presents an offset to the direction of the diphead. The angle between the offset point and the ipsilateral calculation boundary and the horizontal line in the downhill direction is the propagation angle of extraction. When the propagation angle of extraction becomes smaller, it means the inflection point moves towards diphead. The diphead direction is the direction in which the basin spreads.

The positive directions of the two offsets are the west and south directions, respectively. These two directions are the direction of the fault and the adjacent goaf.

Compared to rock formations without the influence of other geological structures and mining activities, the faults and goafs contain more pores and fractures. Once the surrounding rock formations move, these pores and cracks are further compacted, causing the surface to sink. When the faults and goafs are close to the mining working face, the ground surface above them could be induced to sink. For coal mining, when the sinking basin caused by the working face being mined and the sinking basin caused by the further compaction of the rock are very close, they are connected together, it looks like there is a displacement of the sinking basin caused by the mining face. Due to the lack of information on adjacent working faces and faults, this experiment has only modeled the 15235 working face. To compensate for the basin offset, two offset parameters are set. It can be seen from Table 3.3 that the basins with optimized parameters have an offset of 150m and 90m respectively in the west and south directions compared to the basin without parameter optimization. This phenomenon can also be seen in Fig. 3.6. Compared to the modeling of all surrounding geological structures and goafs, it is clear that setting two offset parameters is more efficient, although there could be some slightly shape mismatch. As it can be seen in the residual interferograms part of Fig. 3.3, there are clear residual phases at the right of the modeled basin. Through the calculation of RMSE in Section 3.3.3, it is shown that the benefits outweigh the disadvantages.

3.5 Summary

In this section, a new method to extract large gradient deformation using PSI and an external model is proposed. It is inspired by Fan's fusion method [64]. The proposed method uses the original interferograms to optimize the model parameters to reduce the dependence of the monitoring results on the model parameters, and to improve the consistency between the model simulation results and the interferograms.

The 15235 working face in the China Fengfeng mining area was used to evaluate the presented method in this section. Experiments show that the PIM model with optimized parameters can effectively reduce the fringes in the original interferograms. By reducing the phase ambiguity between PS points and extracting partial deformation in a nonlinear form, the PIM model can help PSI obtain more accurate time-series deformation. Through the verification of the leveling data, the proposed method reduces the monitoring error by 35.2% comparing to the traditional PSI, and by 20.4% comparing to PSI with non-optimized modeling.

The methods and results of parameter optimization are discussed and analyzed. The optimization of the model parameters can prevent surrounding geological structures and goafs from effecting the modeling, and it can also avoid unsuitable parameters affecting the final PSI results.

There are still open issues though. If the impact of geological structures and goafs on the model could be removed, the modeling would be more accurate. The optimization of the model parameters with high efficiency and high precision would allow a better modeling result.

4

Chapter 4

PLR: A filter for SAR Amplitude Information based Offset Tracking

Compared with DInSAR, offset tracking (OT) technology presents higher robustness in incoherent areas and it has the capability to retrieve larger deformations. Therefore, although less precise than DInSAR, OT is a powerful tool in situations when DInSAR fails. In addition, with the unprecedented development of SAR missions, such as Sentinel-1, TerraSAR-X, TanDEM-X, ALOS-2, COSMO-SkyMed, RADARSAT-2, PAZ, Gaofen-3, the planned NISAR, the quantity and quality of SAR acquisitions are constantly improving. Low relative Doppler centroids, short spatial and temporal baselines contribute to the higher accuracy and reliability of subsidence monitoring with any of the available methodologies. Moreover, the accuracy of OT largely depends on the spatial imaging resolution and correlation. Due to the launch of satellites with high-resolution SAR sensors, a better monitoring accuracy can be achieved by OT if high correlation or signal to clutter ratio is guaranteed [24].

The offset related to the mining induced ground deformation is usually continuous and distributed. For the detection of this kind of offset, tracking methods based on the local cross-correlation (CC) of amplitude patches, such as [65], can suffer of patch-like (PL) artifacts that produce ghost deformations in the results. PLs usually appear when scatters with very high amplitudes change location, reflectivity or simply disappear between the two SAR images involved in the CC. The shape and size of PLs are usually the same as the one of the patches involved. PLs are usually independent of the real deformation,

and so, they have to be regarded as errors. To preserve the reliability of the deformation results, PLs must be reduced as much as possible.

Studies like SPOT-CR and PT are addressed to avoid the influence of the Patch-Like (PL) [66, 67]. Their rationale is tracking only the offset of pixels with stable scattering characteristics. The initial processing steps are common to the traditional Persistent Scatterer Interferometry (PSI). The images of the stack are co-registered using an external DEM and the orbital information, which allows to remove the topographic component of the interferograms and, thus, generate the differential interferograms. Firstly, stable pixels are selected, then OT is performed using only these pixels in the CC. These methods can effectively avoid the problem of scattering characteristic changes, the need of any amplitude weighting and they can also reduce the computational burden. But, because only a reduced number of pixels are usually selected, a lot of significant information may be lost. Moreover, if the surface targets are mainly distributed scatterers, as it happen in mining areas, there will be just few qualified pixels to be used for OT.

Instead of stable pixel selection an amplitude filter is proposed in this Chapter, which would reduce the chances of PL effects by replacing those amplitudes higher than an adaptive threshold with zeros. Therefore, it is named as the Patch Like Reduction (PLR) filter.

In order to verify the feasibility of the proposed methodology and evaluate its performance, it has been tested with TerraSAR-X data that covers a mountainous area in Daliuta (China) where mining activity induced severe subsidence in the surface. The advantage of the proposed approach in terms of deformation monitoring has been assessed and discussed. The deformation time-series have been compared with in-field ground GPS measurements. Although there are no large deformations in Barcelona airport (Spain), Andorra and Mexico city (Mexico), covered with Radarsat-2, TerraSAR-X and Sentinel-1B data respectively, these data sets have been used to establish a method to determine the PLR threshold from the images' reflectivity histograms.

The Chapter is organized as follows. In Section 4.1, the conventional OT methods are reviewed, and the causes of PL are identified. The proposed method is detailed in Section 4.2. InSection 4.3, the data sets used to verify the performance of the method are introduced. In Section 4.4 and Section 4.5, the performance of the method is evaluated comparing the results with in-field GPS data. In addition, the impact of the key processing parameters in terms of resolution and accuracy of the results are reviewed in order to select those values that helps to produce better results. Finally, conclusions are given in Section 4.6.

4.1 Review of the Conventional OT

4.1.1 Review of the Existing Imaging Matching Methods

After the co-registration of the master (primary) and slave (secondary) images (usually with the help of an external DEM), OT detects the pixel offsets between them by searching for the maximum value of the cross-correlation (CC) applied to small patches of the images. We can divide the offsets into two types according to the scatterers characteristics:

distributed offsets and single scatterer offsets. Distributed offsets will appear in areas with distributed scatterers, this is when in each resolution cell there are many scatterers contributing to the backscattering but none highlights over the others. They possess a medium or low signal-to-noise ratio and can only be exploited if they form homogeneous groups of pixels that are large enough. On the contrary, single scatterer offsets will appear with deterministic scatterers, when in a resolutions cell there is a single scatterer that is locally predominant over the rest. They are characterized by a high signal-to-noise ratio and they can be processed individually. For example, the subsidence bowl caused by mining activities will cause a distributed offset, neighbouring pixels should present in principle similar behaviours. On the contrary, deterministic individual targets may present the same behaviour or, under some circumstances, a completely different one. A crane or a bulldozer can behave as a deterministic targets and can change its location between two passes of the satellite and, as a consequence, the offset does not represent the mining induced subsidence.

After the coarse registration of the primary and secondary images, OT detects the pixel offset between both by searching for the maximum cross-correlation (CC) value. Although based in the same principles, there are different CC calculation methods. Due to its simplicity, the Normalized Cross-Correlation (NCC) is one of the most commonly used. A window in the master image, named as *reference template*, is searched in the slave image with a moving window, named as *search template*.

The NCC of the pixel in the center of the search template is calculated with,

$$\mathrm{NCC}_{(i,j)} = \frac{\sum_{k,l}\left(s_{(i+k,j+l)} - \mu_s\right)\left(r_{(k,l)} - \mu_r\right)}{\sqrt{\sum_{k,l}\left(s_{(i+k,j+l)} - \mu_s\right)^2\left(r_{(k,l)} - \mu_r\right)^2}} \tag{4.1}$$

Where (i, j) indicates the pixel's position in the search template, (k, l) the pixel's position in the reference template, r the pixel's value of the reference template, s the pixel's value of the search template, μ_r the average value of the reference template and μ_s the average value of the search template. In SAR applications, usually the normalization is ignored.

The relative position of the CC peak indicates the bi-dimensional direction and magnitude of the offset between the center pixels of the reference and the search templates. The computational burden of this approach in the spatial domain is quite high. Since the CC calculation is a convolution operation in the spatial domain, it can be converted to a product in the spectral domain, which is a much more efficient way to determine the CC [65]. Taking advantage of the Fast Fourier Transform (FFT),

$$CCF(i,j) = IFFT\left(F(u,v)\cdot G^{*}(u,v)\right) \tag{4.2}$$

Where $F(u, v)$ and $G(u, v)$ are the reference and search templates in the spectral domain,

$$F = FFT\left(|r|\right); G = FFT\left(|s|\right) \tag{4.3}$$

* denotes complex conjugate and $IFFT$ means the Inverse FFT. In this case, only the amplitude of the complex images is used. By calculating CC in the frequency domain, the computational efficiency can be greatly improved.

In addition, the CC can be also calculated considering also the phase of the images. CCFP is Eq. (4.2) but with,

$$F = FFT(r); G = FFT(s) \tag{4.4}$$

Using the images' phases can lead to better results only if the interferometric phase quality is good. This is not usually the case on heavily decorrelated areas with strong deformations, so in such scenarios it is better to work only with the amplitude.

In general, none of the above methods is significantly better than the other. NCC is simple but time consuming. CCFP uses phase information, and naturally suffers from problems when decorrelation is significant. CCF has a higher computational efficiency but, as the others, it is easily affected by PL [68, 69]. In this Chapter CCF is being used and efforts have been dedicated to reduce the influence of PL in the results.

4.1.2 The Amplitude Distribution and its Influence

4.1.2.1 Amplitude Distribution

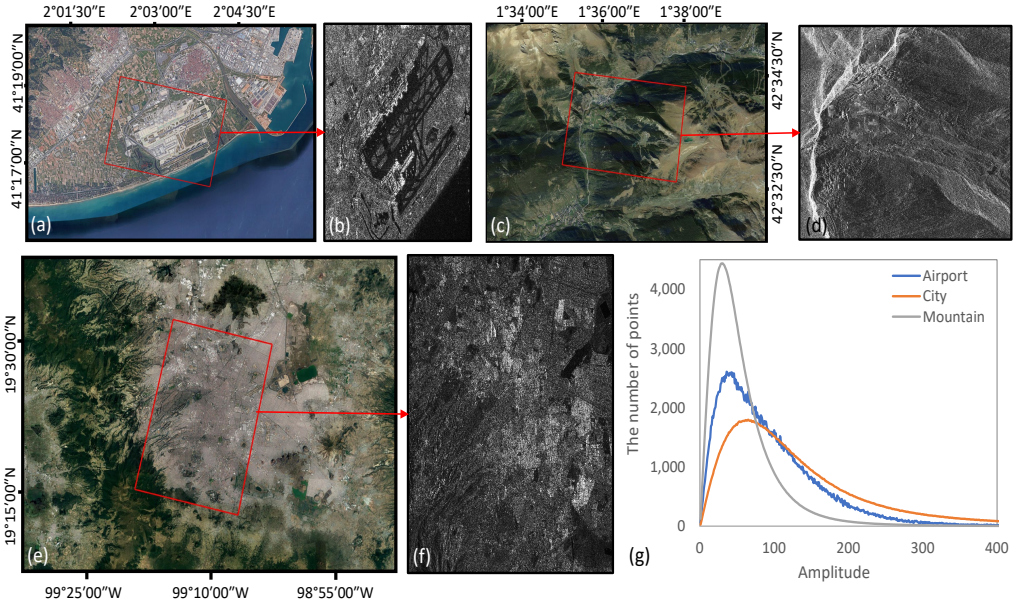

Fig. 4.1. Amplitude distribution curves of different ground features. The red rectangle in Figure (a) (c) (e) is the coverage of SAR image. Figure (b) (d) (f) are the corresponding SAR amplitude image. In Figure (a), there is an airport and some other human structures in Barcelona, Spain.
Figure (c) contains a mountain located in the Principality of Andorra. Figure (e) covers the Mexico City, which is one of the biggest cities in the world. Figure (g) shows the amplitude distributions of these three different cases. The abscissa represents the amplitude value, and the ordinate represents the number of the pixels with corresponding amplitude value.

Fig. 5.6 shows the amplitude distribution of SAR images obtained by different sensors with different incident angles, bands and imaging modes over different areas. The information of each case is presented in Table 4.1. It can be seen from Fig. 5.6(g) that the amplitude distribution obeys a Rayleigh distribution [70], and the scale parameter σ of the Rayleigh distribution ranges from 30 (mountainous area) to 65 (city) due to different backscattering amplitudes. The Rayleigh's probability density function can be written as,

$$p = \frac{x}{\sigma^2} e^{-x^2/(2\sigma^2)} \tag{4.5}$$

while its cumulative function distribution as,

$$c = 1 - e^{-x^2/(2\sigma^2)} \tag{4.6}$$

In addition, it can be seen that the amplitude values of most pixels are between 0-200. Small number of pixels leads to the large fluctuation of the blue curve in Fig. 5.6(g).

Table 4.1: Information of different sensors.

SP. / LF.	Sensor	Incident angle	Resolution	polarization	Image mode	Band	Acquiring date
Airport	RST2	29°	5.1m∗4.7m	HH	Fine	C	Jan 20, 2010
Mountain	TSX	39°	0.23m∗0.59m	HH	Staring	X	Jul 22, 2014
City	Sentinel-1B	44°	14.0m∗2.3m	VV	IWS.	C	May 26, 2017

'SP.' is the abbreviation of 'Sensor parameter'. 'LF.' is the abbreviation of 'Landform'. 'IWS.' is the abbreviation of ' interferometric wide swath'. The format of resolution is azimuth∗slant-range.

4.1.2.2 Effect of Pixels with High Amplitude

If there is one or several pixels with very high amplitude with respect to the rest in the reference window, the location of the peak of the correlation coefficient will be driven by just these few pixels. Moreover, this phenomenon will last until the high-amplitude pixel values are no longer located within the search window. The consequence is that the detected offset will show constant values in a patch lasting the bidimensional size of the correlation window. In some cases the offset can correspond to the real deformation associated to the mining activity but, in others, just to independent changes on the location or reflectivity of these bright pixels.

An OT experiment is carried out to demonstrate the influence of the high amplitude values with two TerraSAR-X SLC images acquired on December 2nd, 2012 and March 22th, 2013, from the data set described in Section 4.3. The matching template size is set as 64×64. No window function is applied. The offset along LOS direction and the two amplitude images are shown in Fig. 4.2. It can be seen that these bright pixels causes, in the best case, a loss of resolution in the offset map as a patch around them will have the

same value, such as the situation in the black circle 3, or, in the worst, offsets not related with the mining activity.

The quality of the OT result can be evaluated with any of the three mainstream indicators: SNR [65], STD [71], and Q [25]. SNR, Std and Q are the commonly used methods used to estimate the accuracy of OT, which can be respectively calculated by Eq. (4.7), Eq. (4.8) and Eq. (4.9).

$$SNR = \frac{\gamma_{\max}}{\bar{\gamma}} \tag{4.7}$$

$$\sigma_{STD} = \sqrt{\frac{3}{2N}} \frac{\sqrt{1-\gamma^2}}{\pi\gamma} \tag{4.8}$$

$$Q = \frac{\gamma_{\max} - \bar{\gamma}}{\bar{\gamma} - \gamma_{\min}} \tag{4.9}$$

where γ is the CC result, $\gamma_{\max}$, $\gamma_{\min}$ and $\bar{\gamma}$ are the maximum CC, the minimum CC and the average value of the CC in the estimation window, respectively. σ_{STD} is the STD of the pixel-offset estimation error in the unit of pixel, N is the number of samples in the estimation window, Q is the quality of the estimation. It can be seen that all indicators describe the result quality through γ. High γ means the reference template and search template match well.

It can be seen from Fig. 4.2(l)-(n) that none of the three methods can detect the error caused by PL. Some PL areas are reckoned reliable such as the situation in circles 1, 4 and 5. Fig. 4.2(o)-(q) shows the relationship between SNR, Std, Q values and the real error obtained by GPS measurements, which also support this view. Because the bright pixels do indeed have shifts, the correlation coefficient has retrieved the proper shifts although they are not representative of the local subsidence. For highly contrasted areas due to strong topography, such those with foreshortening or mountain ridges, γ can be high but the offsets not accurate. All these offsets that do not represent the distributed deformation caused by mining activities have to be eliminated or, at least, minimized.

4.1.3 Relationship between Amplitude Distribution and OT Accuracy

In order to improve the accuracy of OT, pixels with higher amplitudes have to be removed to reduce PL. So, it could be a good policy to replace them by a low amplitude value. A priori, it is not clear which is the optimal upper threshold and if it can be selected case independently. Different experiments have been carried out with the data sets detailed in Table 4.1 in which mild or no deformation is expected and, thus, the average values of the detected offsets can be regarded as a measure of the error. The datasets correspond to a city, a mountainous area and an airport. The upper threshold for setting the amplitudes to zero is increased from 90 to the max in steps of 30. As the amplitude distributions are different in each area, the offset error is plotted as a function of the cumulative pixels in Fig. 4.3. The cumulative values can be easily calculated from Eq. (4.6) using the scale parameter σ of the distribution and the amplitude value. A cumulative value of

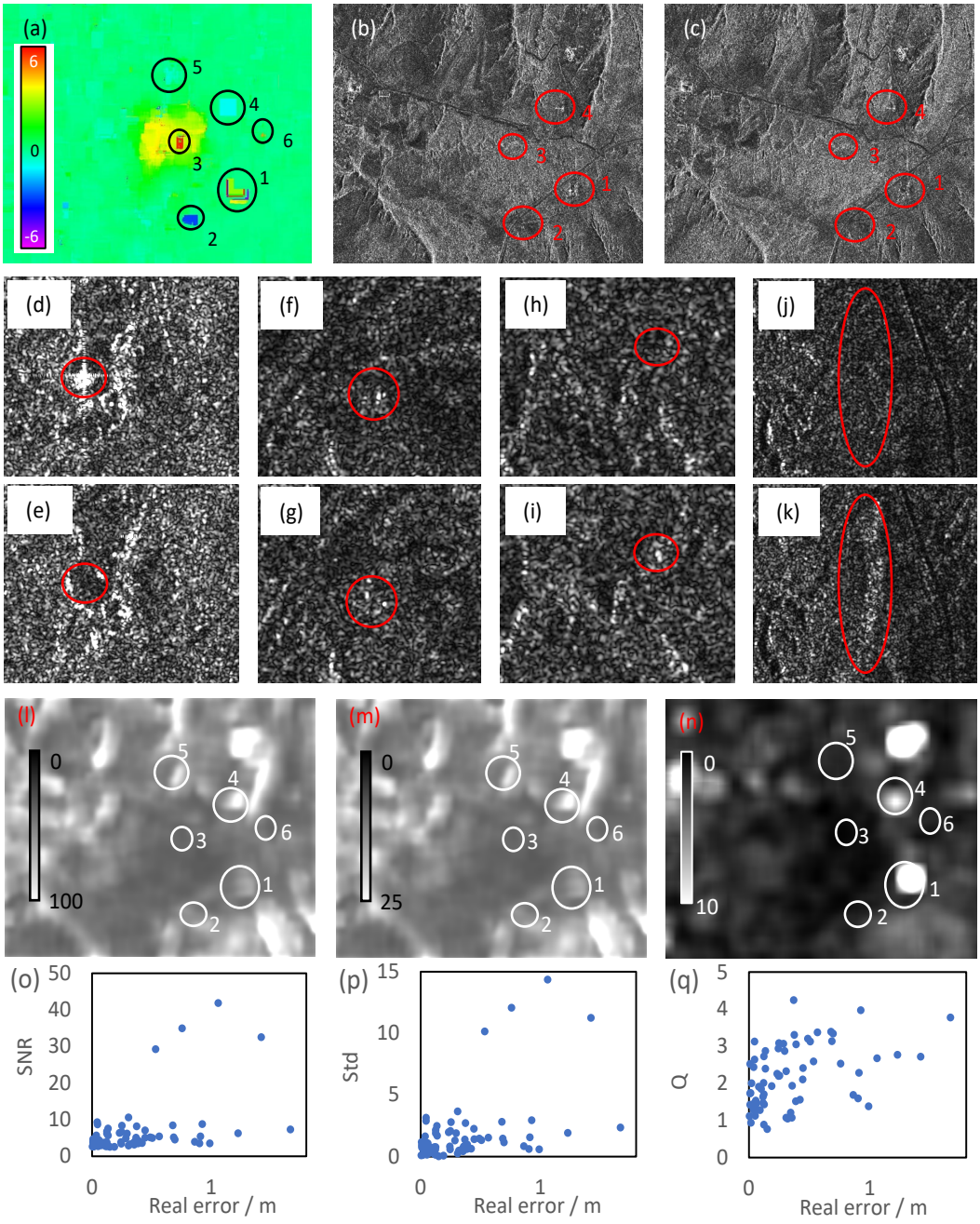

Fig. 4.2. The reason of PL and result evaluations. (a) Range offsets. (b) and (c) The amplitude images before and after the deformation. (d) and (e) Zoom of the red circles 1 in (b) and (c). (f) and (g) Zoom of the red circles 2 in (b) and (c). (h) and (i) Zoom of the red circles 3 in (b) and (c). (j) and (k) Zoom of the red circles 4 in (b) and (c). (l) SNR map. (m) Std map and (n) Q. Correlation between real error and SNR (o), Std (p) and Q (q).

0.9 indicates that the threshold is set to a value that sets to 0 the 10% of pixels with the highest values. It can be seen that, for the three cases, near 0.992 the error reaches the minimum and this can be established as a scenario-independent threshold. From Eq. (4.6), the threshold can be thus set as a function of the scale parameter and the cumulative threshold,

$$x = \sqrt{2}\sigma\sqrt{\ln\left(1/(1-c_{thr})\right)} = 3.1\sigma \tag{4.10}$$

The threshold would allow to remove the high amplitude pixels which are prone to induce PL but with no impact in the accuracy of OT.

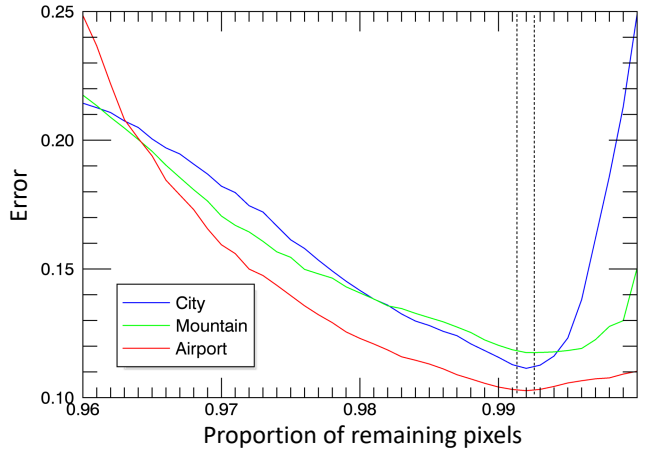

Fig. 4.3. Relationship between errors and the proportion of remaining pixels.

4.2 Proposed Method

The overall scheme of the proposed OT process is shown in Fig. 4.4(a). Similar to the traditional OT, it mainly consists of a coarse registration [72], a base banding for the proper interpolation [22] and the offset detection. The innovation of this Chapter is the PLR amplitude filter applied to both the primary and secondary images to eliminate the chances of PL in the results. The scheme of PLR is shown in Fig. 4.4(b).

On the one hand, Section II has demonstrated that the PLR can effectively reduce the appearance of PL. On the other hand, in mining areas the relevant information is mainly the distributed deformation. Therefore, it is reasonable to eliminate pixels with the highest amplitude values in order to obtain offsets that represent the sought deformation. According to the experiment in Section II-C, it is recommended to set the upper boundary to $\rho = 2.2\sigma$. ρ is the threshold that makes the number of the retained pixels be the 92% of all pixels.

The amplitude filter is defined as,

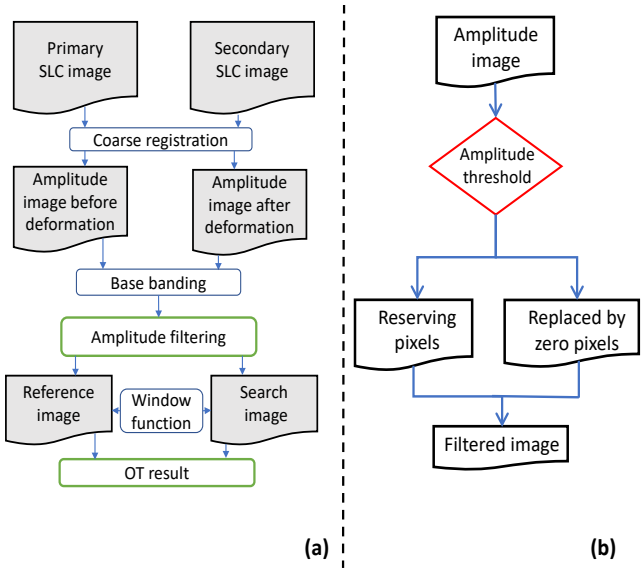

Fig. 4.4. Scheme of the proposed methods. (a) Overall scheme of the OT process. (b) Scheme of the amplitude filter.

$$A_{M(i,j)} = \begin{cases} A_{(i,j)}, & A_{(i,j)} \leq \rho \\ 0, & A_{(i,j)} \geq \rho \end{cases} \tag{4.11}$$

All pixels in the amplitude image are then divided into retained and discarded pixels. The filtered image is obtained after replacing the values of the discarded pixels with 0.

4.3 Study Area and Data Sets

A deformation area located in Daliuta Town, China (shown in Fig. 4.5) is selected to assess the performance of the proposed methods. This area is in the largest coal producing region in China. The coal seam is thick and shallow with loose layers, which leads to a so large deformation on the ground that is beyond the DInSAR monitoring capabilities. The working panel of interest is named as 52304, with a length of 4,548 m, a width of 301 m, a depth of 235 m and a thickness of 7 m. It was started on November 1st, 2012 and terminated on March 25th, 2013.

Real Time Kinematic (RTK) GPS measurements were collected along the mining direction and its perpendicular direction and will be used for the OT results validation. The red circles in Fig. 4.5 represent the location of these 71 GPS stations. A total of 45 of the stations are located along the mining direction and spaced 20 m while the remaining 26 are located along its perpendicular direction and spaced 25 m.

In this Chapter, 19 spotlight TerraSAR-X SLC images are employed to obtain the ground-deformation time series with a pixel spacing of 0.91×0.86 m (range × azimuth), a heading direction of 189.53°, a wavelength of 3.11 cm, a local incident angle of 42.43°, a

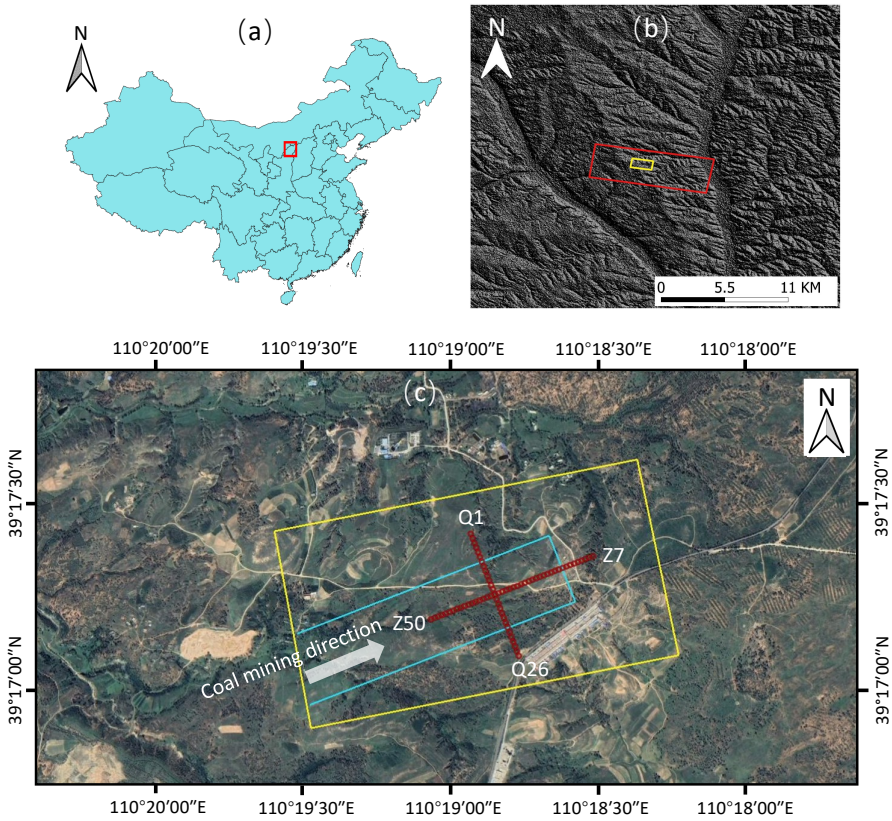

Fig. 4.5. Location and topography of the study area. The red rectangle in Figure(a) is on behalf of the study area in this experiment. The red rectangle in Figure(b) means the SAR image coverage. The yellow rectangles in Figure(b) and (c) represent the region of interest. The cyan rectangle in Figure(c) is the location of a working panel. The red circles represent the GPS station and the white letters and numbers are their names. The white arrow means the mining direction.

revisit period of 11 days and with HH polarization,. These images were acquired during the period from November 10th, 2012 to July 10th, 2013.

4.4 Results

In order to minimize the influence of the temporal decorrelation, images with the shortest temporal baselines are related in consecutive pairs. The deformation time series are obtained by integrating the deformation increments along consecutive pairs. SAR images are base-banded before OT to allow the correct interpolation of the slave image. The size of the search template is set to 64×64 pixels with a triangular window function to ensure a narrow correlation peak and, at the same time, trying to preserve the deformation resolution. Images are oversampled by a factor of 2 prior the cross correlation to reduce

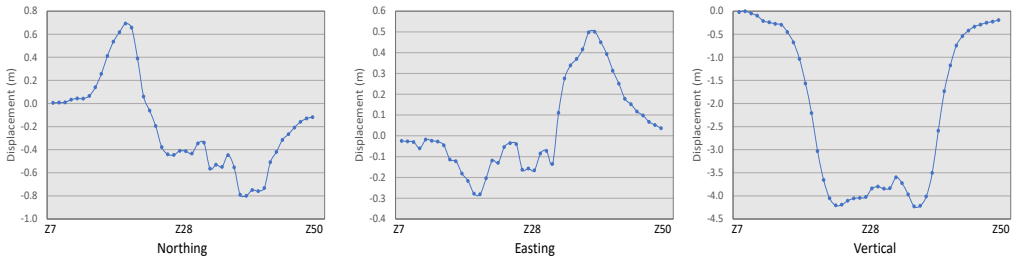

Fig. 4.6. The northing, easting and vertical surfce displacements measured by GPS.

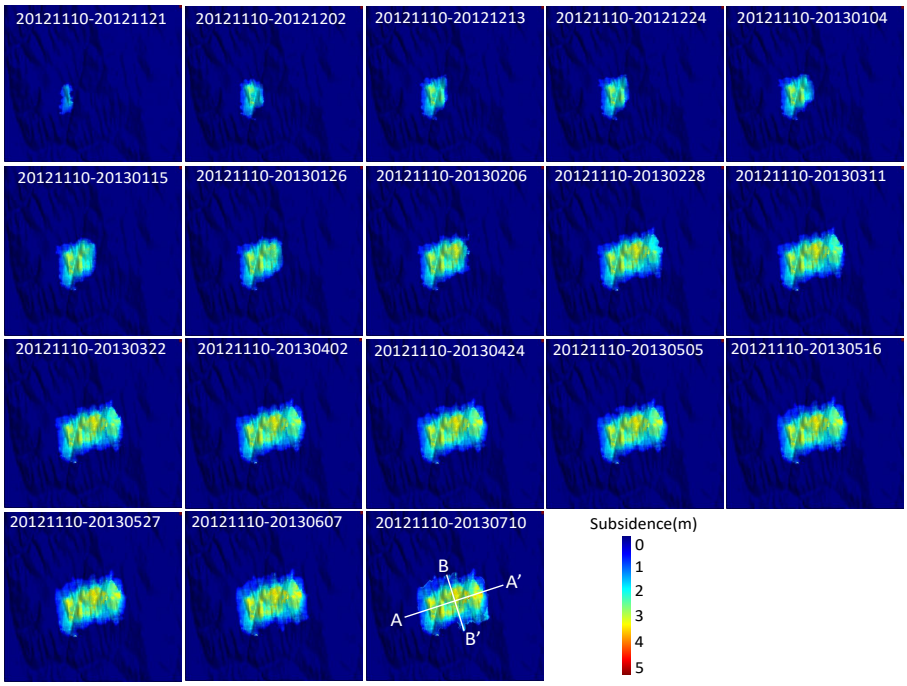

Fig. 4.7. Time series vertical deformation obtained by OT with PLR.

bias errors and noise [65].

If it is assumed that the deformation is mainly vertical [73], the detected slant-range offsets are converted into vertical deformation with,

$$S_{\text{sub}} = \frac{P_{\text{offset}} \cdot R_{\text{size}}}{\cos\theta} \tag{4.12}$$

Where P_{offset} is the pixel range offset before and after the deformation in the range direction, S_{sub} is the vertical deformation, θ the local incident angle and R_{size} the pixel size in the range direction. Azimuth offsets can not be related to a vertical deformation and, thus, they are ignored in the time-series retrieval. Fig. 4.6 shows the displacements in three directions measured by GPS from December 7th, 2012 to March 28th, 2013.

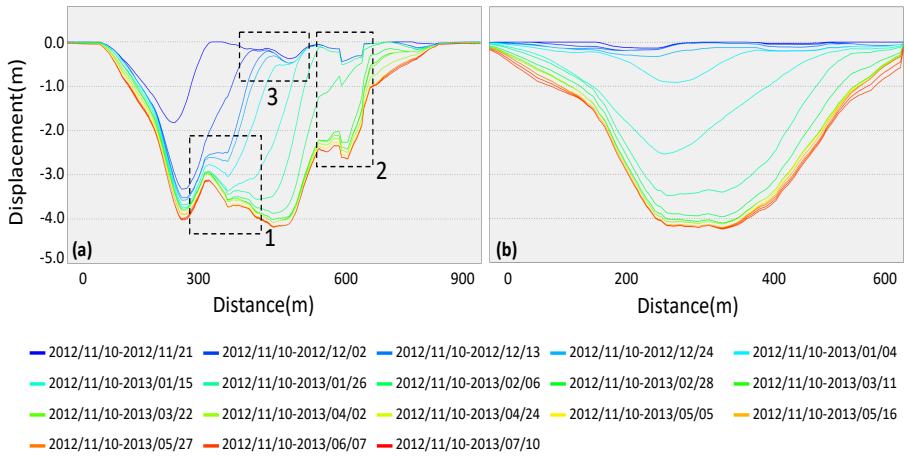

Fig. 4.8. Time series subsidence profiles in the mining direction AA' (a) and perpendicular mining direction BB' (b).

It can be seen that the horizontal deformation is only about one-tenth of the vertical deformation. Its magnitude is very close to noise and error, thus it is difficult to extract it effectively.

As Fig. 4.7 shows, the deformation area was growing with the mining activity from November 10th, 2012 to March 11th, 2013. After March 11th, 2013 the shape of the subsidence basin started to be stable. This temporal behaviour is consistent with the reported mining activity.

Two profiles AA', along the mining direction, and BB', perpendicular to the mining direction, are used to quantitatively analyze the mining induced subsidence. Their positions are marked in Fig. 4.7, and the deformation time series are shown in Fig. 4.8. As it can be seen, the maximum subsidence value of curve AA' changes greatly from November 10th, 2012 to December 2nd, 2012. The deformation is up to 1.8 m during the first 11 days while the average deformation rate is 164 mm/day. From November 21st, 2012 to December 2nd, 2012, the ground sinks up to 1.5 m with an average velocity is 136 mm/day. Such large deformation rate definitely exceeds the monitoring capabilities of classical DInSAR techniques. In addtion, they may cause cracks, landslides and even collapses on the surface. The maximum deformation value is 4.2 m when the ground tended to be stable.

Different from the sinking evolution seen along AA', changes along BB' are not visible at the beginning of the mining activity because the gallery had not reached yet their position. The surface started to drastically experience subsidence from January 4th, 2013 to January 26th, 2013. Since BB' is perpendicular to the mining direction, the sinking of BB' presents a bowl shape. This is different from the results in AA', where the subsidence develops from left to right.

BB' has a relatively regular shape, while AA' has many bends as the basin develops, as shown in the black dashed rectangular boxes 1, 2 and 3 in Fig. 4.8. In rectangle 1, the local uplift appears with the deformation increase. Usually and in order to reduce

surface subsidence caused by underground mining, the coal seams are not all dugout. Some columnar coal is left behind to support the roof of the coal seam. The local uplift may be caused by the support of these reserved coal pillars. The depression in rectangle 2 may represent a local collapse because its shape changes with the basin development and lasts until the end. There is also a depression in rectangle 3, but it is smoother compared with the one in rectangle 2. Besides, this depression was annexed by the deformation that spread here, instead of keeping its shape until the end like the depression in rectangle 2. These phenomena indicate that the depression is not caused by a local collapse. One possible explanation is that there was an underground cavity here, which was formed naturally or caused by other mining activities. Subsequent geological activities activated the void, compacted it, and caused the surface to sink.

4.5 Discussion

4.5.1 PL Elimination

Fig. 4.2(a) shows the location of different PLs in the results with the original processing approach. The proposed PLR is applied and the results are shown in Fig. 4.9. For both processings, the shape and size of the subsidence basins are very similar, but the proposed filter can effectively eliminate PL effects.

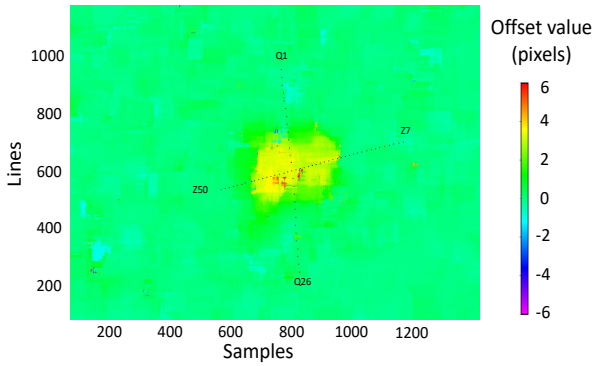

Fig. 4.9. OT results with the application of the proposed PLR filter. The positions of GPS station are marked with $Z7 - Z50$ and $Q1 - Q26$.

Taking GPS as the ground truth, the root mean square errors (RMSE) of the two OT results, with and without PLR, are calculated separately. In order to reduce location errors, 3×3 averaging windows are set centered at the location in slant-range coordinates of each GPS observing station. The 9 pixels averaged deformation is taken as the final result to compare with the GPS measurements. The RMSE of the OT results with and without the filter are 53.6 mm and 68.4 mm respectively, which means that the monitoring accuracy has been improved 21.6% with the filter.

Fig. 4.10 demonstrates how the PLR is able to reduce PLs. One reference template and its corresponding search template are selected on a stable position, marked with the

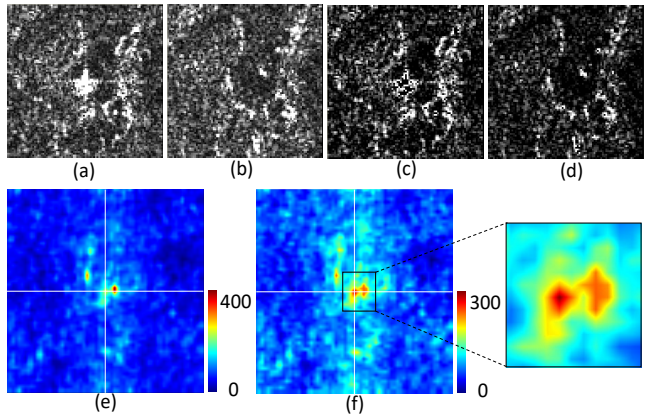

Fig. 4.10. Comparison between the amplitude image before and after amplitude filtering. Graph (a) and (b) show the reference template and search template without amplitude filtering, graph (e) is their correlation map. Graph (c) and (d) show the same templates with amplitude filtering, graph (f) is their correlation map. White lines in the middle of graph (e) and (f) help locate the peak.

black circle 1 of Fig. 4.2(a), prone to generate PL. It can be seen that, the reference template in Fig. 4.10(a) has a strong scatter whose amplitude dramatically changes in Fig. 4.10(b), which causes an offset not related to deformation of the CC peak. After PLR, other stable scatters dominate the correlation, so the highest peak appears, as expected with an area with no deforation, in the center. Although the value of the correlation coefficient is reduced, the amplitude filter avoids the influence of unexpected ground feature changes and, therefore, reduces the chances of PL.

4.5.2 Deformation Resolution

It is well known that the selection of the template size is a compromise between deformation precision, driven by the sharpness of the CC peak, and the deformation spatial resolution. For the former the larger the better, as large correlation windows provide better precision in the deformation values. For the latter it is just the contrary, short correlation windows allow a better spatial deformation resolution but with less reliable values. It has to be be noticed that the averaging effect of large windows causes that detected offsets may be smaller than the real ones when deformation gradients are present.

A simulated reference template with random amplitude values ranging from 0 to 200 is used to reveal the relationship between the template size, the deformation resolution and the error. A deformation area, which size can be modified, with a uniform 1 pixel offset is introduced in the search template. Then, the offset in the center of the deformation area between both templates is detected and its SNR calculated as well.

Fig. 4.11 shows that the best offset estimations occur when the search template and the deformation area have similar sizes, presenting also the highest SNR. Being the deformation homogeneous, when the search window is increased compared with the deformation area the offset starts to be underestimated and this underestimation increases

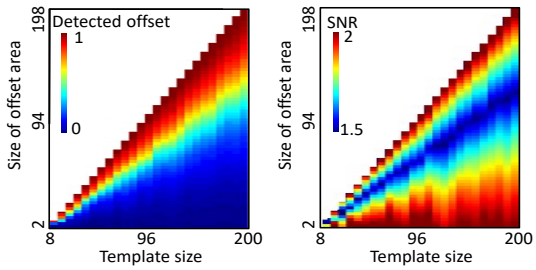

Fig. 4.11. Relationship between the deformation resolution and the template size.

as the size difference enlarges. On the extreme with a tiny deformation area and a large search window, the deformation is completely missed as the stable area dominates. The behavior of the SNR is quite different, the worst SNRs are obtained when the deformation area is around half of the search window. In this case, the CC has to adjust to two different behaviors with similar weights in the process. On the other extremes, either similar deformation area and search windows or small deformation area and large search window, the deformation or the stable area dominates and so the SNR is the highest.

The results of different template sizes with a non-uniform deformation are shown in Fig. 4.12. It is clear that small template sizes are able to follow the deformation variations but with noisier estimations. Large template sizes lead to clearly less accurate results.

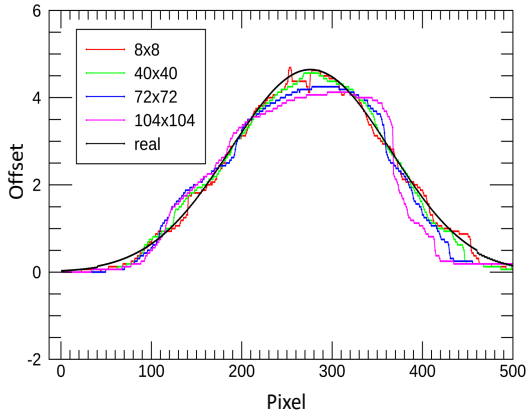

Fig. 4.12. Results of OT with different template sizes.

4.5.3 Effects of Different Window Functions

One way to keep the advantages of the large template while improving the accuracy at the same time is the use of a window function on the templates. The triangular and hamming windows have been tested and the results shown in Fig. 4.13. The improvement is obvious. The triangular window leads to s smoother result, while the offset with hamming window is closer to the real value.

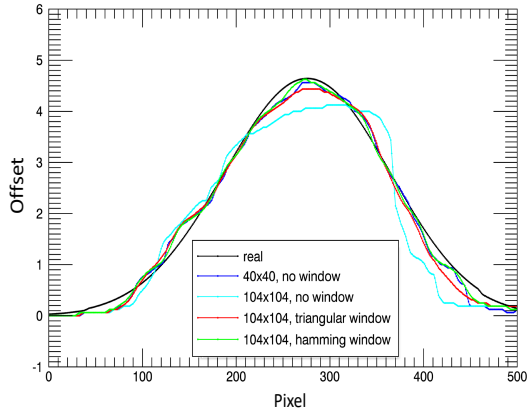

Fig. 4.13. Results of OT with different windows.

4.6 Conclusion

In this Chapter, the causes of the appearance of PL in deformation monitoring results with OT have been studied. It has been found that the changes of high amplitude pixels in the images disturb the cross correlation calculations. Thus, the elimination of these high amplitude values can avoid, or at least reduces, the chances of PL. The selected threshold for eliminating pixels has an impact on the quality of the final results. Setting it too high does not affect the appearance of PL, setting it too low increase the noise of the final results. Considering that amplitude SAR images follow a Rayleigh distribution and using three different data sets, it has been found that eliminating the highest 0.08% values produces the optimal results. Therefore, an amplitude filter named as PLR is proposed. PLR reduces the PL by replacing the highest amplitude values with zero. In order to have a image independent criterion, the threshold is defined as a function of the scale parameter of the Rayleigh distribution.

To validate the feasibility of the proposed amplitude filter, it has been tested with the TerraSAR-X data and the results validated with in-field GPS data acquired over Daliuta area in China. It has been shown that with the filter the monitoring accuracy is improved by a 21.6% with respect the non-filtered version of OT.

In addition, the effect of the different template size and tapering window functions have been investigated. The template size is a compromise between deformation spatial resolutions and accuracy and it can be determined according to the allowable error and the desired deformation resolution. The tapering of the images with a window function prior the cross-correlation can help to preserve the deformation resolution under the premise of a given template size. The triangular window can make the results smoother than those obtained with a Hamming window.

5

Chapter 5

ACE-OT: Polarization SAR Data based Amplitude Contrast Enhancement Algorithm for Offset Tracking Applications

As more SAR satellites with polarimetric capabilities are available, it is feasible to improve OT performance taking advantage of polarimetry. As one of the few OT methods using polarimetry, the polarimetric similarity tracking method was proposed to improve the accuracy of OT [25]. The multiple offset results are obtained through different polarization channels, and the hypergeometric Bessel function is applied to estimate the most likely result. This method can improve OT reliability and can be implemented into any kind of multivariate remote sensing data such as multichannel optical images. However, the polarimetric data are simply regarded as simply redundant observations, while the scattering information contained in them is not utilized. Another polarimetric data based OT method proposed by Wang defined the cross correlation according to the vector constructed by Pauli decomposition [27]. This method is able to exploit the scattering information and improve the OT accuracy, but due to the characteristics of the Pauli decomposition, the effect of the single scattering in the image is emphasized, while the ef-

fect of the volume scattering and the double scattering is being reduced. Besides, instead of doing optimization, the different kinds of reflections are simply added when calculating the correlation between two images, which does not fully exploit the potentiality of polarimetric data.

For PSI, polarimetric data based amplitude and phase optimizing methods improve the performance of deformation detection and characterization by increasing the density and quality of valid pixels with respect to the single polarization case [29–32,34–40,74–79]. The main idea of polarimetric optimization is to construct a polarization space and find the optimal projection of the polar vector in this space.

However, these optimization methods are not suitable for the OT case as they are based on optimizing the phase quality. Compared with the phase, the amplitude is more robust to the loss of coherence, which is the reason why OT is still a powerful alternative to DInSAR despite its lower accuracy. Therefore, this paper does not consider coherence-based phase optimization methods. For the methods where the optimization criterion is the amplitude deviation [35, 36] the information of targets at more than two different moments are required. The basic OT processing works with image pairs. Besides, the optimization methods for DInSAR assume that the offset caused by the deformation is very small, at least within one pixel. This assumption does not hold for the OT case. The offset detected by OT could be several pixels. Therefore, the existing polarimetric optimization algorithms for DInSAR are not suitable for OT.

For the amplitude information based OT, contrast is one of the most important indicators to estimate the suitability of the images for the method. The cross-correlation between two images can not be properly calculated if distinctive features are not present. Image contrast, this is the energy distribution, is an effective quantitative indicator to measure the presence of distinctive features in a SAR image. Larger contrasts imply richer feature information. Therefore, inspired by Yang [80, 81], an amplitude optimization method based on contrast enhancement is proposed in this paper. The method improves the image contrast by searching the optimal polarization combination leading to the largest contrast according to the scattering mechanisms of ground objects, and therefore is named as Amplitude Contrast Enhancing Offset Tracking (ACE-OT).

Two different PolSAR data sets are used to assess the performance of the proposed method. One is dual-pol TerraSAR-X images over Daliuta (China), which is affected by strong mining-induced subsidence. The deformation time series are obtained by the proposed ACE-OT. The other data set is quad-pol Radarsat-2 images acquired over the Barcelona airport. Because the deformation in this area is too small to be detected by OT, this data set is used for simulation experiments to evaluate the capability of the proposed method on separating the scattering mechanisms and improving the amplitude contrast.

The chapter is organized as follows. In Section 5.1, the proposed method is introduced. The data set and result are described in Section 5.2. Some discussion are performed in Section 5.3. Finally, conclusions are given in Section 5.4.

5.1 Methodology

The overall scheme of the proposed method is shown in Fig. 5.1(a). Similar to the conventional OT, images need to be co-registered and base-banded before their interpolation and cross correlation calculation. The scheme of the amplitude enhancement method is shown in Fig. 5.1(b). One step is marked with a dotted line because it can only be applied with quad-pol data. The amplitude filtering introduced in Chapter 4 is carried out before the offset tracking processing.

Instead of only enhancing part of the image [80], the proposed method can improve the contrast of the whole image. In the particular case of a monostatic system, as the sensors considered in this paper, the cross-polar channels should be equal, i.e. $S_{HV} = S_{VH}$.

The enhancement algorithm is mainly composed of three steps: orientation elimination, similarity parameter acquisition and contrast optimization.

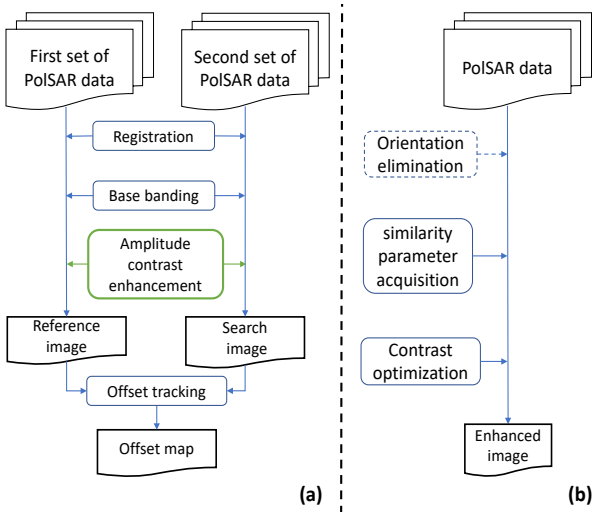

Fig. 5.1. Scheme of the proposed ACE-OT. (a) Overall scheme of the OT process. (b) Subscheme of ACE-OT.

5.1.1 Orientation Elimination

The complex back scattering matrix **S** for a monostatic radar can be defined as [82–85]:

$$[\mathbf{S}] = \begin{bmatrix} S_{HH} & S_{HV} \\ S_{VH} & S_{VV} \end{bmatrix} \quad (S_{HV} = S_{VH}) \tag{5.1}$$

where S_{HH}, S_{HV}, S_{VH}, S_{VV} are the different polarimetric channels of the target response. The subscript means the polarization of the received and transmitted signals.

It can be seen from Fig. 5.2 that after the reflection, the polarization ellipse of the received signal is rotated by an angle φ with respect to the transmitted one. The angle φ depends on the geometric relationship between the antenna and the target, and the

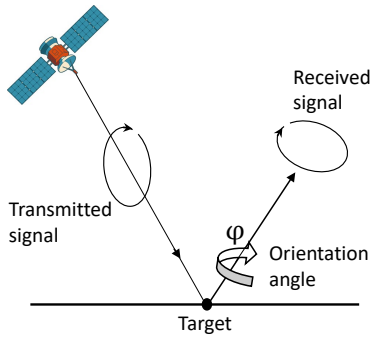

Fig. 5.2. Polarization ellipse rotation of the target reflection with respect the transmitted one.

properties of the target. Scattering matrices of some targets are orientation independent, while others are not [86]. The ellipse orientation could change the phase information in the received signals, it is thus necessary to eliminate it with Eq. (5.2)

$$\left[\mathbf{S}^0\right] = [\mathbf{J}(-\varphi)] \cdot [\mathbf{S}] \cdot [\mathbf{J}(\varphi)] = \begin{bmatrix} S^0_{HH} & S^0_{HV} \\ S^0_{VH} & S^0_{VV} \end{bmatrix} \tag{5.2}$$

where

$$[\mathbf{J}(\varphi)] = \begin{bmatrix} \cos\varphi & -\sin\varphi \\ \sin\varphi & \cos\varphi \end{bmatrix} \tag{5.3}$$

The orientation φ can be obtained by the Huynen decomposition [86]

$$\varphi = \frac{1}{2} \cdot \arctan \frac{2 \cdot \mathrm{Re}\left\{S^*_{HV}\left(S_{HH} + S_{VV}\right)\right\}}{\left|S_{HH} - S_{VV}\right|^2} \tag{5.4}$$

where *Re* means retaining the real part of a complex number and $*$ means complex conjugate.

After the operation by Eq. (5.2), (5.3) and (5.4), the influence of the ellipse orientation on the following calculations can be avoided. This step can not be applied to dual-pol data because the orientation φ can not be determined with Eq. (5.4)

5.1.2 Similarity Parameters Acquisition

The proposed method defines three similarity parameters according to [80]. The first two parameters r_1 and r_2 describe two basic scattering mechanisms: single reflection and double reflection from a target, as shown in Eq. (5.5) and (5.6). r_1 is large in calm sea areas or smooth surfaces like roads, roofs or fields. r_2 is small in the previous cases but large in urbanized areas. The third parameter, r_3, is the polarization entropy [87], which is very good for measuring the randomness of targets like those affected by volume scattering, shown in Eq. (5.7).

$$r_1 = \frac{\left|S^0_{HH} + S^0_{VV}\right|^2}{2\left(\left|S^0_{HH}\right|^2 + \left|S^0_{VV}\right|^2 + 2\left|S^0_{HV}\right|^2\right)} \tag{5.5}$$

$$r_2 = \frac{\left|S^0_{HH} - S^0_{VV}\right|^2}{2\left(\left|S^0_{HH}\right|^2 + \left|S^0_{VV}\right|^2 + 2\left|S^0_{HV}\right|^2\right)} \tag{5.6}$$

$$r_3 = -\sum_{i=1}^{3} P_i \log_3 P_i \tag{5.7}$$

$$P_i = \frac{\lambda_i}{\sum_{k=1}^{3} \lambda_k}, \quad \sum_{k=1}^{3} P_k = 1 \tag{5.8}$$

$$\mathbf{k}_T = \frac{1}{\sqrt{2}} \begin{bmatrix} S^0_{HH} + S^0_{VV} \\ S^0_{HH} - S^0_{VV} \\ 2S^0_{HV} \end{bmatrix} \tag{5.9}$$

$$\mathbf{T} = \frac{1}{L} \sum_{n=1}^{L} (\mathbf{k}_T \cdot \mathbf{k}_T^+) \tag{5.10}$$

r_3 can be obtained by Eq. (5.7), (5.8), (5.9) and (5.10). Where $\mathbf{k}_T$ is the Pauli spin matrix, λ_i the eigenvalues of the polarization coherence matrix $\mathbf{T}$ by singular value decomposition, P_i the pseudo probability obtained from the eigenvalues, L the look number, and $+$ the Hermitian or conjugate transpose. In this paper, $\mathbf{T}$ is calculated with a 3×3 averaging window.

The values of r_1, r_2 and r_3 range from 0 to 1. The larger the parameter, the stronger the corresponding reflection type. For example, a large r_1 value represents that the reflection is mainly a single bounce.

5.1.3 Contrast Optimization for Quad-pol Data

The Optimization of Polarimetric Contrast Enhancement (OPCE) can increase the contrast between two kinds of targets [85, 88, 89]. Assuming $\mathbf{T}_\mathrm{A}$ and $\mathbf{T}_\mathrm{B}$ are the average scattering matrices of two ground targets, $\bar{\mathbf{K}}(\mathbf{T}_\mathrm{A})$ and $\bar{\mathbf{K}}(\mathbf{T}_\mathrm{B})$ are their Kennaugh matrices. The Kennaugh matrix can be obtained according to,

$$\bar{\mathbf{K}} = \left\langle \mathbf{A}_4^* \left([\mathbf{S}^0] \otimes [\mathbf{S}^0]^*\right) \mathbf{A}_4^{-1} \right\rangle \tag{5.11}$$

where $\otimes$ represents the tensor product and $\mathbf{A}_4$ is,

$$\mathbf{A}_4 = \begin{bmatrix} 1 & 0 & 0 & 1 \\ 1 & 0 & 0 & -1 \\ 0 & 1 & 1 & 0 \\ 0 & j & -j & 0 \end{bmatrix} \tag{5.12}$$

The OPCE optimization consists on finding $\mathbf{g} = (1, g_1, g_2, g_3)^t$ and $\mathbf{h} = (1, h_1, h_2, h_3)^t$ that maximizes the power ratio of $\mathbf{T}_\mathrm{A}$ and $\mathbf{T}_\mathrm{B}$ with constrains, i.e.,

$$\begin{aligned} \text{maximize} \quad & \frac{\mathbf{h}^t[\bar{\mathbf{K}}(\mathbf{T}_\mathrm{A})]\mathbf{g}}{\mathbf{h}^t[\bar{\mathbf{K}}(\mathbf{T}_\mathrm{B})]\mathbf{g}} \\ \text{subject to} \quad & g_1^2 + g_2^2 + g_3^2 = 1 \\ & h_1^2 + h_2^2 + h_3^2 = 1. \end{aligned} \tag{5.13}$$

Yang. [80] assumed that the optimal function should contain the scattering characteristics of the target. However, under normal circumstances, we cannot know the optimal functional form. Therefore, Generalized Optimization of Polarimetric Contrast Enhancement (GOPCE) assumes that the functional form includes two factors. One factor is the received energy, which is mentioned in OPCE, and the other is the scattering characteristics of the target. Same as $\mathbf{h}$ and $\mathbf{g}$, $\mathbf{x}$ helps find the maximum power ratio of $\mathbf{T}_\mathrm{A}$ and $\mathbf{T}_\mathrm{B}$.

$$\begin{aligned} \text{maximize} \quad & \frac{\frac{1}{M}\sum_{\mathbf{T}_\mathrm{A}}\left[\sum_{i=1}^{3} x_i r_i(\mathbf{T}_\mathrm{A})\right]^2}{\frac{1}{N}\sum_{\mathbf{T}_\mathrm{B}}\left[\sum_{i=1}^{3} x_i r_i(\mathbf{T}_\mathrm{B})\right]^2} \times \frac{\mathbf{h}^t[\bar{\mathbf{K}}(\mathbf{T}_\mathrm{A})]\mathbf{g}}{\mathbf{h}^t[\bar{\mathbf{K}}(\mathbf{T}_\mathrm{B})]\mathbf{g}} \\ \text{subject to} \quad & g_1^2 + g_2^2 + g_3^2 = 1 \\ & h_1^2 + h_2^2 + h_3^2 = 1 \\ & x_1^2 + x_2^2 + x_3^2 = 1 \end{aligned} \tag{5.14}$$

where M and N denote the selected pixel numbers of $\mathbf{T}_\mathrm{A}$ and $\mathbf{T}_\mathrm{B}$, respectively. It can be seen from Eq. (5.14) that the contrast can be improved by enhancing the desired target $\mathbf{T}_\mathrm{A}$ versus the undesired target $\mathbf{T}_\mathrm{B}$.

For the OT applications, the contrast of the whole image needs to be enhanced instead of only two kinds of targets. The contrast calculation proposed by Cumming [41] can be applied as the optimizing criteria:

$$C = \frac{E\left(|I|^2\right)}{[E(|I|)]^2} \tag{5.15}$$

where I is intensity and E the mathematical expectation.To obtain the maximum contrast, the optimal equation is established according to GOPCE.

$$
\begin{aligned}
& \mathrm{OP} = \left[\sum_{i=1}^{3} x_i r_i\right]^2 \times \mathbf{h}_m^t[K]\mathbf{g}_m \\
\text{subject to} \quad & \mathbf{g} = (1, g_1, g_2, g_3)^t \\
& \mathbf{h} = (1, h_1, h_2, h_3)^t \\
& \mathbf{x} = (x_1, x_2, x_3)^t \\
& g_1^2 + g_2^2 + g_3^2 = 1 \\
& h_1^2 + h_2^2 + h_3^2 = 1 \\
& x_1^2 + x_2^2 + x_3^2 = 1
\end{aligned}
\tag{5.16}
$$

The optimal polarization states **g**, **h**, and **x** are the same as those of the GOPCE. The maximum contrast can be achieved after finding these optimal states. From Eq. (5.16) it is known that **g**, **h**, and **x** could be the coordinates of a point that is on a spherical surface with a radius of 1 and a centered at the origin of coordinates, $(0, 0, 0)$. Therefore, the original 9 parameters to be optimized can be reduced to 6, i.e.,

$$
\begin{aligned}
\mathbf{g} &= (1, \sin\alpha\cos\theta, \sin\alpha\sin\theta, \cos\alpha)^t \\
\mathbf{h} &= (1, \sin\beta\cos\gamma, \sin\beta\sin\gamma, \cos\beta)^t \\
\mathbf{x} &= (1, \sin\delta\cos\epsilon, \sin\delta\sin\epsilon, \cos\delta)^t
\end{aligned}
\tag{5.17}
$$

For a multi-parameter optimization problem, many approaches can be applied, such as the Newton-Raphson method, quasi Newton method, and the Conjugate Gradient Method (Conjugate Gradient Method (CGM)). Due to its low computational burden and high computational efficiency, CGM [90] is applied to obtain **g**, **h**, and **x** for maximizing the contrast in Eq. (5.15). The enhanced amplitude image can be generated once the parameters **g**, **h**, and **x** are obtained.

5.1.4 Contrast Optimization for Dual-pol Data

Since dual-pol SAR is quite common as some polarimetric sensors can not provide full-pol data, like Sentinel-1, it is necessary to consider their capabilities for contrast enhancement. There are two kinds of combinations for dual-pol data: two co-polar channels (i.e., $HH - VV$) and a co-polar and a cross-polar channels (i.e., $HH - VH$ or $VV - HV$). As the processing and the behaviour of the enhancement strongly depends on the presence of a cross-polar channel, they will be presented separately.

5.1.4.1 Enhancement with $HH - VV$

The lack of cross-pol data makes impossible to eliminate the orientation. Consequently, the contrast enhancement starts with the calculation of the similarity parameters. r_1, r_2 and r_3 are defined as:

$$r_1 = \frac{|S_{HH} + S_{VV}|^2}{2\left(|S_{HH}|^2 + |S_{VV}|^2\right)} \tag{5.18}$$

$$r_2 = \frac{|S_{HH} - S_{VV}|^2}{2\left(|S_{HH}|^2 + |S_{VV}|^2\right)} \tag{5.19}$$

$$r_3 = -\sum_{i=1}^{2} P_i \log_2 P_i \tag{5.20}$$

As in the quad-pol case, r_3 is calculated by the pseudo probabilities obtained from the eigenvalues of the polarization coherence matrix $\mathbf{T}$. From Eq. (5.21) it is known that due to the lack of the cross-pol data, $\mathbf{k}_T$ becomes a two-dimensional vector, $\mathbf{T}$ thus turns into a 2×2 matrix. Therefore, only two eigenvalues can be obtained, instead of the three of quad-pol data, and the pseudo probabilities are calculated with Eq. (5.22)

$$\mathbf{k}_T = \frac{1}{\sqrt{2}} \begin{bmatrix} S_{HH} + S_{VV} \\ S_{HH} - S_{VV} \end{bmatrix} \tag{5.21}$$

$$P_i = \frac{\lambda_i}{\sum_{k=1}^{2} \lambda_k}, \quad \sum_{k=1}^{2} P_k = 1 \tag{5.22}$$

Although values for r_3 can be obtained, the absence of cross-pol data make them potentially inaccurate and noisy. The entropy maps obtained from $HH - VV$ data are compared with those obtained with quad-pol data. Sections 5.2.2.2 and Section 5.3 show and discuss the results. Therefore, this lack of reliability of r_3 forces it to do not allow its participation in the contrast enhancement.

The scattering matrix in this case becomes:

$$[\mathbf{S}] = \begin{bmatrix} S_{HH} & 0 \\ 0 & S_{VV} \end{bmatrix} \tag{5.23}$$

With $\mathbf{S}$ the Kennaugh matrix $[\mathbf{K}]$ can be obtained. The optimization equation is defined as:

$$\begin{aligned} \text{OP} = & \left[\sum_{i=1}^{2} x_i r_i\right]^2 \times \mathbf{h}_m^t [\mathbf{K}] \mathbf{g}_m \\ \text{subject to} \quad & \mathbf{g} = (1, g_1, g_2, g_3)^t \\ & \mathbf{h} = (1, h_1, h_2, h_3)^t \\ & \mathbf{x} = (x_1, x_2)^t \\ & g_1^2 + g_2^2 + g_3^2 = 1 \\ & h_1^2 + h_2^2 + h_3^2 = 1 \\ & x_1^2 + x_2^2 = 1 \end{aligned} \tag{5.24}$$

Once the optimized equation is established, CGM is used to find **g**, **h**, and **x** that maximize the contrast.

5.1.4.2 Enhancement with $HH - VH$ or $VV - HV$

As there is only one co-polar channel, xx, r_1 and r_2 will be identical. Therefore, only r_1 and r_3 participate in the contrast enhancement. They are defined as:

$$r_1 = \frac{|S_{\mathrm{xx}}|^2}{2\left(|S_{\mathrm{xx}}|^2 + 2\,|S_{HV}|^2\right)} \tag{5.25}$$

$$r_3 = -\sum_{i=1}^{2} P_i \log_2 P_i \tag{5.26}$$

$$P_i = \frac{\lambda_i}{\sum_{k=1}^{2} \lambda_k}, \quad \sum_{k=1}^{2} P_k = 1 \tag{5.27}$$

$$\mathbf{k}_T = \frac{1}{\sqrt{2}} \begin{bmatrix} S_{xx} \\ 2S_{hv} \end{bmatrix} \tag{5.28}$$

The scattering matrix becomes:

$$[\mathbf{S}] = \begin{bmatrix} S_{HH} & S_{HV} \\ S_{HV} & 0 \end{bmatrix} \text{ or } \quad [\mathbf{S}] = \begin{bmatrix} 0 & S_{HV} \\ S_{HV} & S_{VV} \end{bmatrix} \tag{5.29}$$

With **S** the Kennaugh matrix, $[\mathbf{K}]$ can be obtained. The optimization equation is defined as:

$$\begin{aligned} \mathrm{OP} &= (x_1 r_1 + x_3 r_3)^2 \times \mathbf{h}_m^t [K] \mathbf{g}_m \\ \text{subject to} \quad & \mathbf{g} = (1, g_1, g_2, g_3)^t \\ & \mathbf{h} = (1, h_1, h_2, h_3)^t \\ & \mathbf{x} = (x_1, x_3)^t \\ & g_1^2 + g_2^2 + g_3^2 = 1 \\ & h_1^2 + h_2^2 + h_3^2 = 1 \\ & x_1^2 + x_3^2 = 1 \end{aligned} \tag{5.30}$$

5.2 Data Sets and Results

5.2.1 Data Sets

To validate the proposed amplitude contrast enhancement method, two different scenarios, an airport and a mountainous area, and two SAR data sets, have been selected. The first

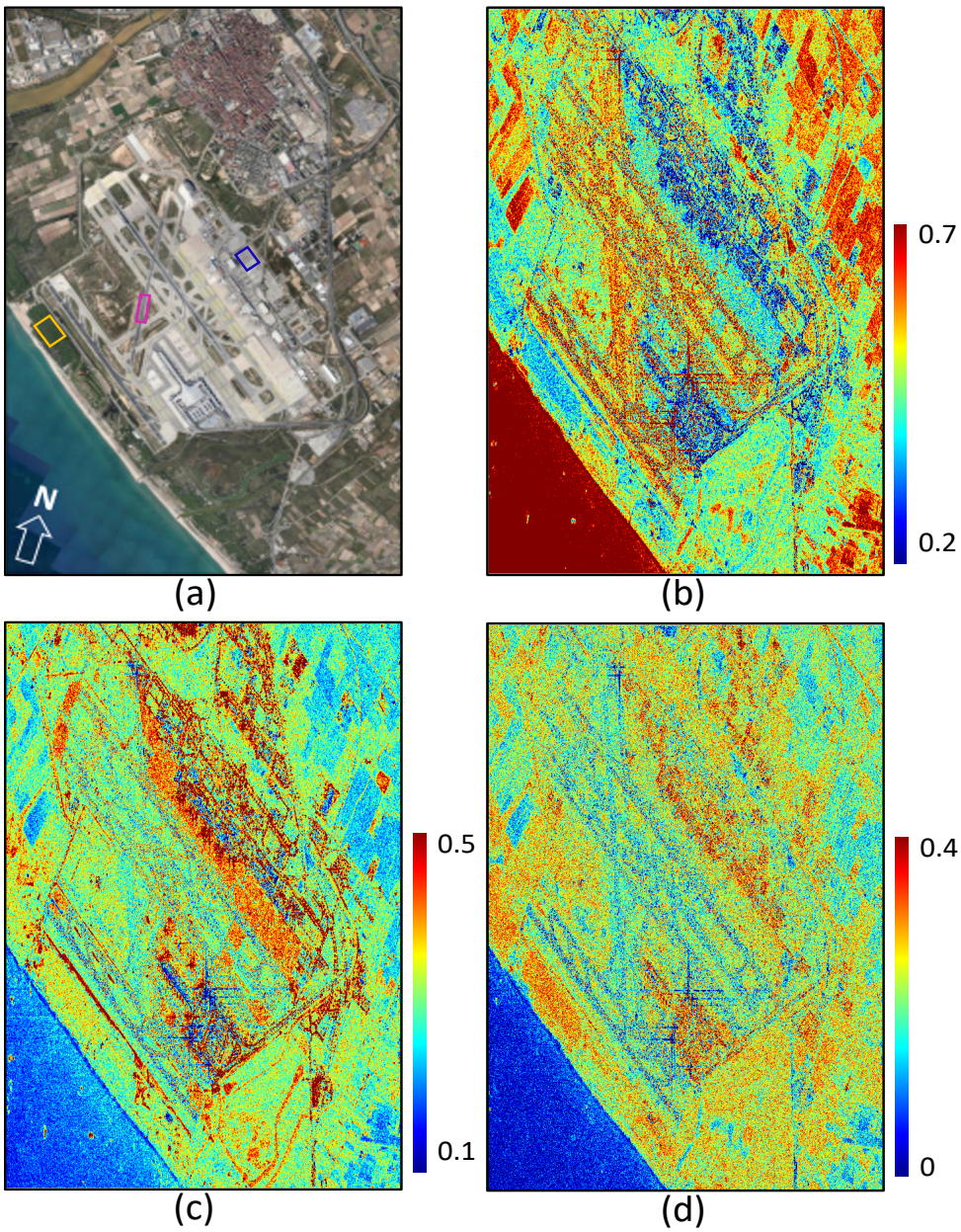

Fig. 5.3. Temporal average scatter mechanism maps obtained from quad-pol Radarsat-2 images. (a) Optical image from Google Earth. (b) Value of similarity parameter r_1, related to the measurement of single reflections. (c) Value of similarity parameter r_2, related to the measurement of double reflections. (d) Value of similarity parameter r_3, i.e., polarization entropy, related to the measurement of randomness. The features highlighted with orange, magenta and blue rectangles in (a) are a farmland with vegetation, a road and a building, respectively.

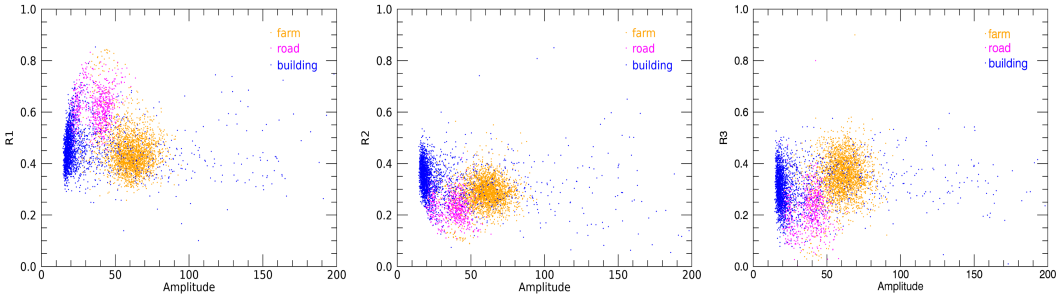

Fig. 5.4. Relationship between amplitude and similarity parameters of different ground features. Scatter plots of (a) amplitude vs r_1, (b) amplitude vs r_2, and (c) amplitude vs r_3.

data set consists of 31 stripmap quad-pol Radarsat-2 images over the Barcelona airport (Spain), acquired from June 2010 to July 2012. The resolution is 5.1 m in azimuth and 4.7 m in range. Radarsat-2 works at C-band and has a revisit period of 24 days. The processing has been applied over an area of 902 × 602 pixels. Since the real deformation is too small to be detected by OT, simulated offsets have been added to the images.

The other test site is located in Daliuta (China), a mountainous area affected by large ground deformations caused by coal mining activities. The data set covering this area consists of 20 TerraSAR-X SPOT dual-pol images (HH and VV), acquired from April 2014 to December 2014, with a resolution of 2.2 m in azimuth and 1.2 m in range. TerraSAR-X works at X-band and has a revisit period of 11 days. The processing has been applied over an area of 376 × 399 pixels.

Besides the PolSAR images, a SRTM DEM with a resolution of 90 m has been used to help with the image co-registration [72].

5.2.2 Results

5.2.2.1 Results of Airport Test Site

Because the proposed method performs contrast enhancement based on the scattering mechanism of the ground targets, it is very important whether the scattering types are correctly retrieved. Fig. 5.3 shows the reflection types in the airport area, calculated from the temporal average of the 31 Radarsat-2 images, as well as the optical image to help recognize ground features. As expected, the value of r_1 is large in airport runways, sea, bare land, and roofs of large buildings, r_2 is large in urbanized areas and r_3 is large in vegetated areas and areas with complex structures that induce volume scattering, such as the airport terminal.

Three typical ground features (farmland with vegetation, roads, and buildings) are selected to analyze their scattering characteristics. Their locations are marked with orange, magenta, and blue rectangles in Fig. 5.3(a). The scatter plots between the amplitude and the three similarity parameters are shown in Fig. 5.4. The average amplitudes of the two co-polar and one cross-polar channels are used as the abscissa for all samples. It can be seen that the three features present different amplitude distributions. The building has

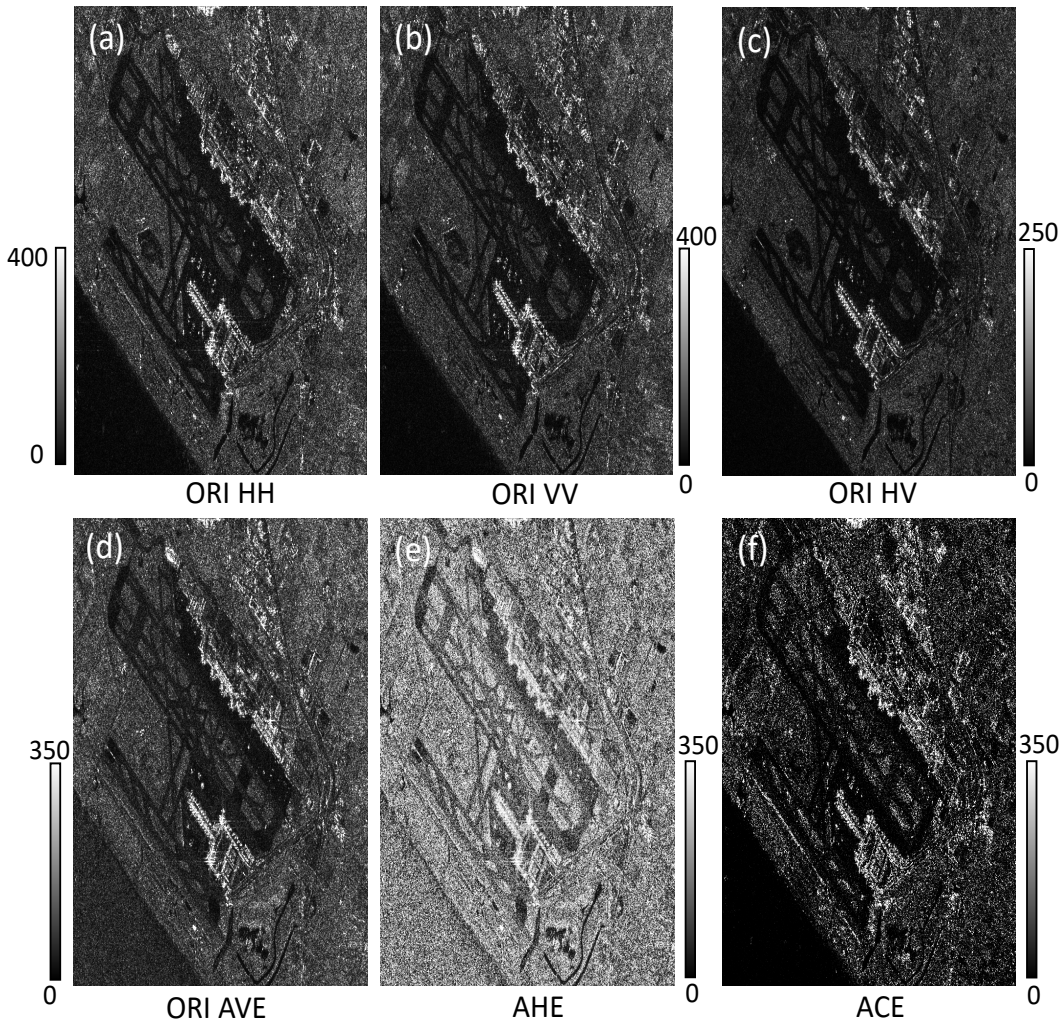

Fig. 5.5. Amplitude comparison before and after the application of the two contrast enhancements. The images are acquired on January 20, 2010. (a), (b) and (c) show the original HH, VV and HV amplitudes (the file values no-radiometrically corrected), respectively. (d) is the averaged amplitude from the four polarimetric channels, (e) is the AHE contrast enhanced amplitude, (f) is the ACE contrast enhanced amplitude. (d), (e) and (f) use identical scale bars for a better comparison.

the largest concentration of low amplitudes while the farmland just the contrary. Usually, the buildings have high values in the amplitude image. In the case of the airport however, due to the smoother roof and regular geometry, the building could have lower amplitude values. At the same time, the building presents the highest dispersion of values as the higher amplitudes also correspond to buildings. Both farm and road have a lower dispersion of amplitudes.

From Fig. 5.4, one easily finds that r_1 of the road presents the largest values, r_2 of

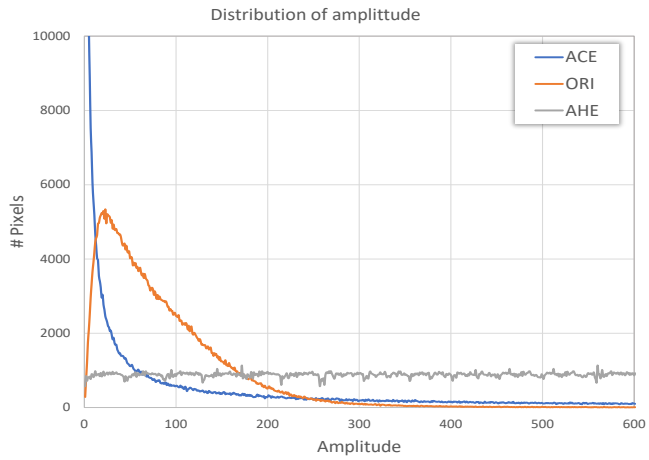

Fig. 5.6. Amplitude distribution for the original averaged polarimetric channels and the contrast optimized with Adaptive Histogram Enhancement (AHE) and Amplitude Contrast Enhancement (ACE) images.

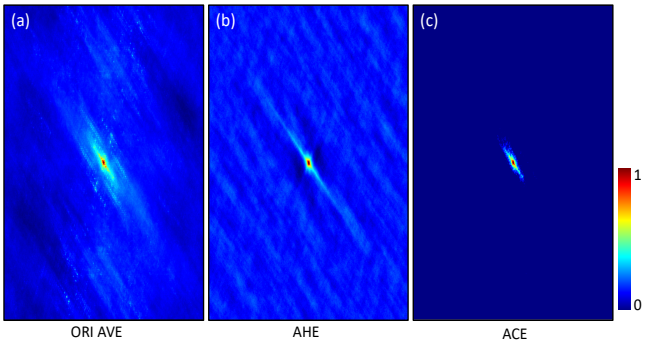

Fig. 5.7. Cross correlation comparison before and after contrast enhancements with January 15, 2011 and July 2, 2011 images. (a) is the cross-correlation obtained from the average amplitudes of the original HH, VV and HV channels, (b) and (c) are the cross-correlation maps obtained from the images enhanced with AHE and ACE, respectively.

the building is the largest and r_3 of the farm is the largest. The scattering characteristics of the three ground features in Fig. 5.4 are consistent with the results in Fig. 5.3, which means r_1, r_2 and r_3 can represent the single, double and random reflection, respectively.

After the validation of the scattering mechanism separation, the amplitude contrast enhancement is applied to Radarsat-2 images and the result is shown in Fig. 5.5. There are many methods to enhance image contrast, but as far as the authors know, they are based on pure image processing and they do not consider or take advantage of the scattering mechanisms information present in the data. A classical method called Adaptive histogram equalization (AHE) has been selected to compare with the proposed method [91]. Adaptive histogram equalization involves applying contrast enhancement based on the local region surrounding each pixel. Each pixel is mapped to an intensity proportional

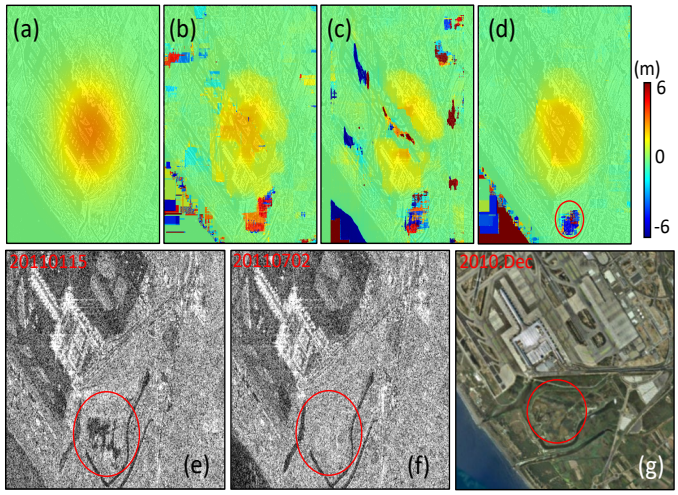

Fig. 5.8. OT result. (a) is the simulated deformation in slant-range, (b) the deformation obtained with the original averaged channels, (c) and (d) the deformation obtained with images enhanced with AHE and ACE, respectively. (e) and (f) are a detailed view of the HH channel amplitude acquired on January 15, 2011 and July 2, 2011, respectively. (g) is the optical image of the same area from Google Earth. The red circle in (d) highlights a swamp that causes a strong variation of the amplitude in the temporal time-span.

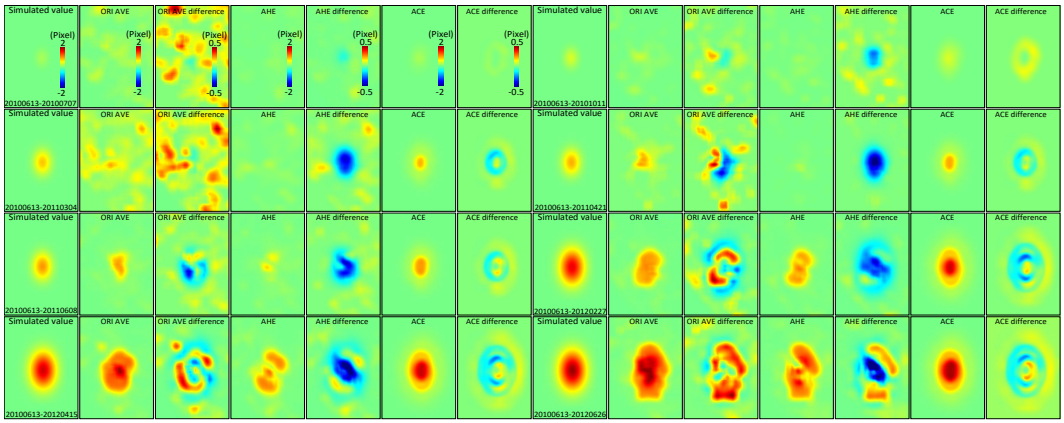

Fig. 5.9. Simulated deformation time-series using Radarsat-2 data. There are 8 different time spans. For each one 7 images are shown: the simulated slant-range deformation, the deformation obtained from the averaged polarimetric channels and its error, deformation obtained with AHE enhanced images and its error map, and, finally, deformation obtained with ACE enhancement and its error map.

to its rank within the surrounding neighborhood. This method of automatic contrast enhancement has proven to be broadly applicable to a wide range of images and to have demonstrated effectiveness. The contrast of each polarimetric channel is around 1.25, the contrast of their average amplitudes image is 1.12, while the AHE and ACE contrast

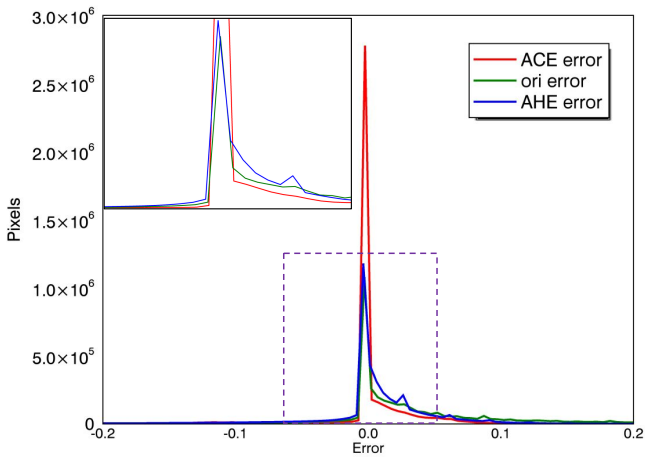

Fig. 5.10. The error distributions of the proposed method and two benchmark methods, calculated from the 8 time series simulated OT results with Radarsat-2 images.

are 1.74 (over the averaged amplitude image) and 2.76, respectively. Fig. 5.6 shows the amplitude distributions for each case. AHE only changes the amplitude values from the Rayleigh distribution to a continuous uniform distribution, without considering the scattering mechanisms, thus the contrast improvement is not so obvious. It can be seen that the airport runways and the sea area are brighter after AHE, while the received energy from these areas was small in the original images. This is due to the fact that the contrast enhancement is performed locally and based only on the averaged image. On the other side, with ACE, the areas with strong scatters are emphasized, such as the airport terminals and buildings, while the weak areas are emaciated, such as the airport runways, the roads and swamp in the bottom of the image. From the amplitude image and the three scatter mechanism maps we can see that there are many speckles in the farmland and some roads. These speckles can be associated to small towers, small bridges, small piers or even rocks which are highlighted by ACE, although they can also be noise in some cases. Generally speaking, the enhancement of all the features presents in the amplitude images lead to the improvement of contrast.

The cross correlations of the amplitude images with and without the enhancements are calculated and shown in Fig. 5.7. The images were acquired on January 15, 2011, and July 2, 2011. Fig. 5.7(a) shows the cross correlation calculated by the average amplitude of the original HH, VV, and HV polarization data, and Fig. 5.7(b) and (c) shows the cross correlation of the images enhanced by AHE and ACE respectively. It can be seen that after AHE, the gradient near the peak of correlation is larger, which is beneficial for offset tracking. However, the cross correlation coefficient also increase for almost the whole map, meaning that the two amplitude images, although having larger contrast, become more different after the enhancement. This is attributed to the contrast enhancement in areas with random behaviours, like the sea, or low signal, like runaways. In the case of ACE, the cross correlation peak is sharper and the gradient near the peak is increased, while the cross correlation coefficient decreases elsewhere.

To demonstrate the advantage of the enhancement method, an OT processing is carried

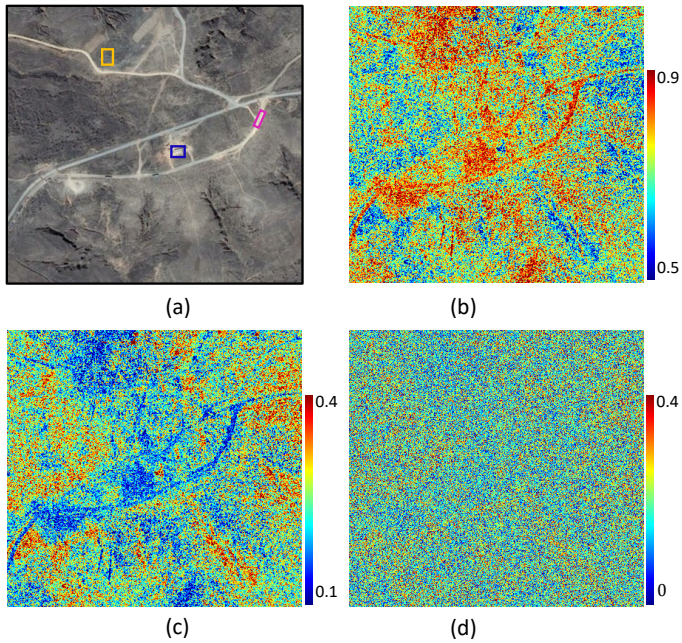

Fig. 5.11. Scatter mechanism maps derived from the averaged dual-pol polarimetric channels of TerraSAR-X dataset. (a) Optical image from Google Earth. (b), (c) and (d) are the values of similarity parameters r_1, r_2 and r_3. The features highlighted with in orange, magenta and blue rectangles in are a farmland, a road and a building, respectively.

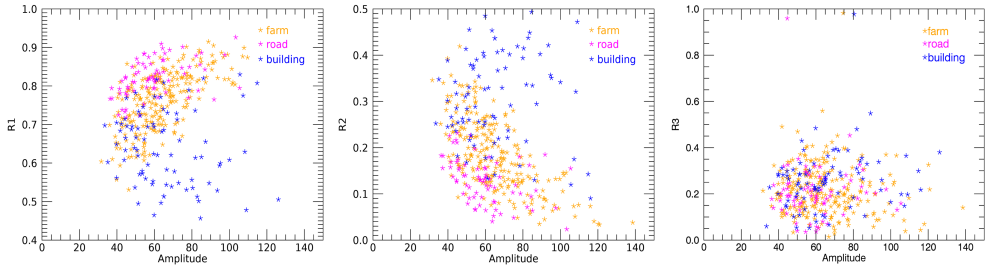

Fig. 5.12. Scatter plots of amplitude vs similarity parameters for different ground features. (a), (b) and (c) are amplitude vs r_1, r_2, r_3, respectively.

out with the same two images. A simulated offset in slant range direction is added on the second as the real deformation is extremely weak. The template size is set to 64×64 pixels with no windowing. The simulated offset, and the offset obtained with the original images, the images enhanced by AHE and ACE are shown in Fig. 5.8(a), (b), (c) and (d) respectively. It can be seen that the shape of the offset area in (b), (c) and (d) are similar to the simulated one, while it is clear that the result of ACE enhanced images is smoother and has fewer abnormal values. Non-realistic offsets are obtained in the lower left corners of Figure (b), (c) and (d), which belong to the sea. In an operational use of the method, the sea should be masked. Another wrong result is located in the area

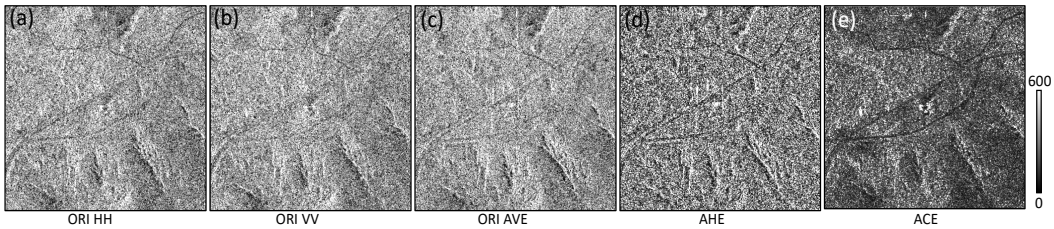

Fig. 5.13. Amplitude comparison before and after the contrast enhancement. (a) and (b) are the original HH and VV channels. (c) is the averaged channels. (d) and (e) are the contrast enhanced images by AHE and ACE, respectively.

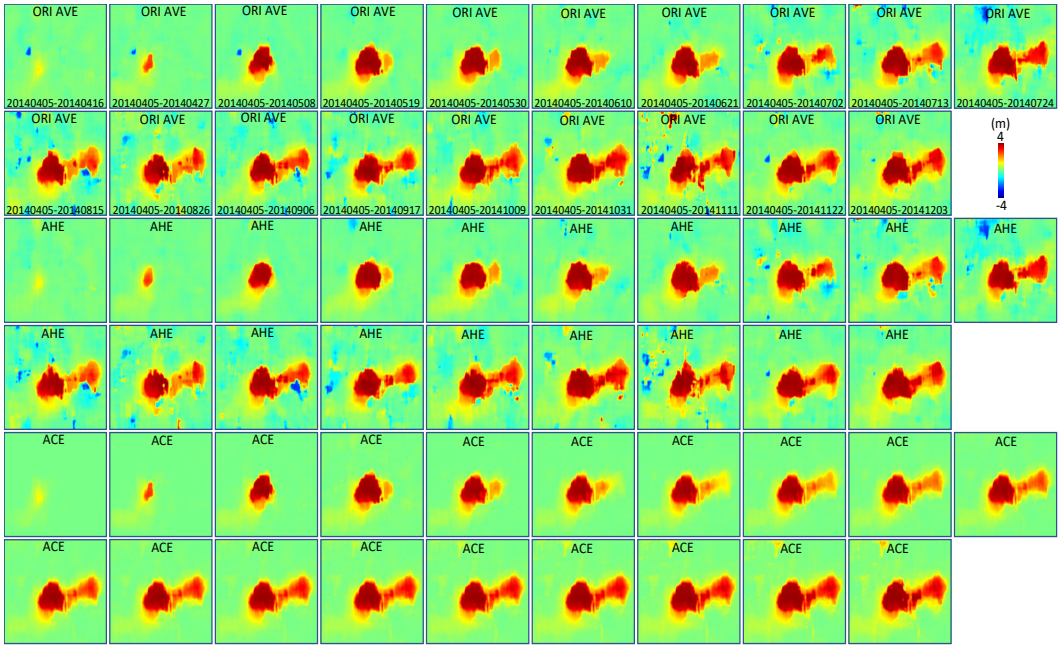

Fig. 5.14. Deformation time-series maps obtained from TerraSAR-X data. The first two rows are the deformation results obtained with the average image of the original HH and VV channels. The middle two rows and the last two rows are obtained with images enhanced by AHE and ACE, respectively.

highlighted with the red circle in Fig. 5.8(d) that is caused by dramatic changes on the amplitude. It is obvious from (d)-(f) that vegetation has disappeared in winter and grew up again in summer.

A simulated deformation time series is added to the 31 Radarsat-2 images mentioned in Section 5.2.1. The deformation rate is set to be linear. After the image enhancement and masking of sea and error prone areas, OT is applied with a template size of 64×64 pixels. The deformation time series over time are obtained and shown in Fig. 5.9. The sea area and the noisy area encircled in red in Fig. 5.8(d) have been masked. The image pair used corresponds to the deformation period indicated at the bottom of each deformation

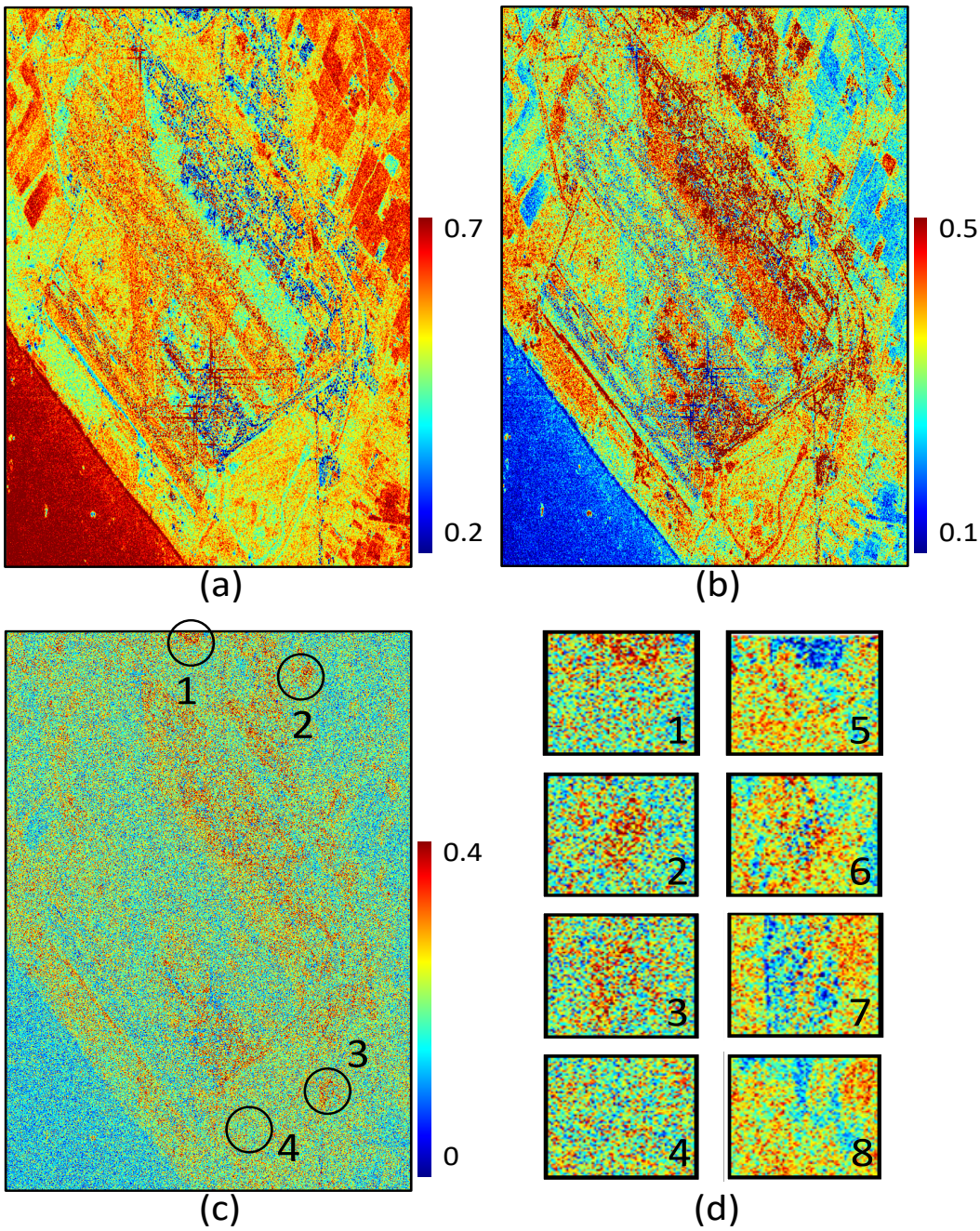

Fig. 5.15. Scatter mechanism maps obtained from the temporally averaged Radarsat-2 dual co-polar data, $\{HH, VV\}$. (a), (b) and (c) are the values of similarity parameters r_1, r_2 and r_3. The zoom of the areas encircled in black are shown in the rectangles labeled 1 to 4 in (d), 5-8 are the same areas shown in Fig. 5.3 (d) as references.

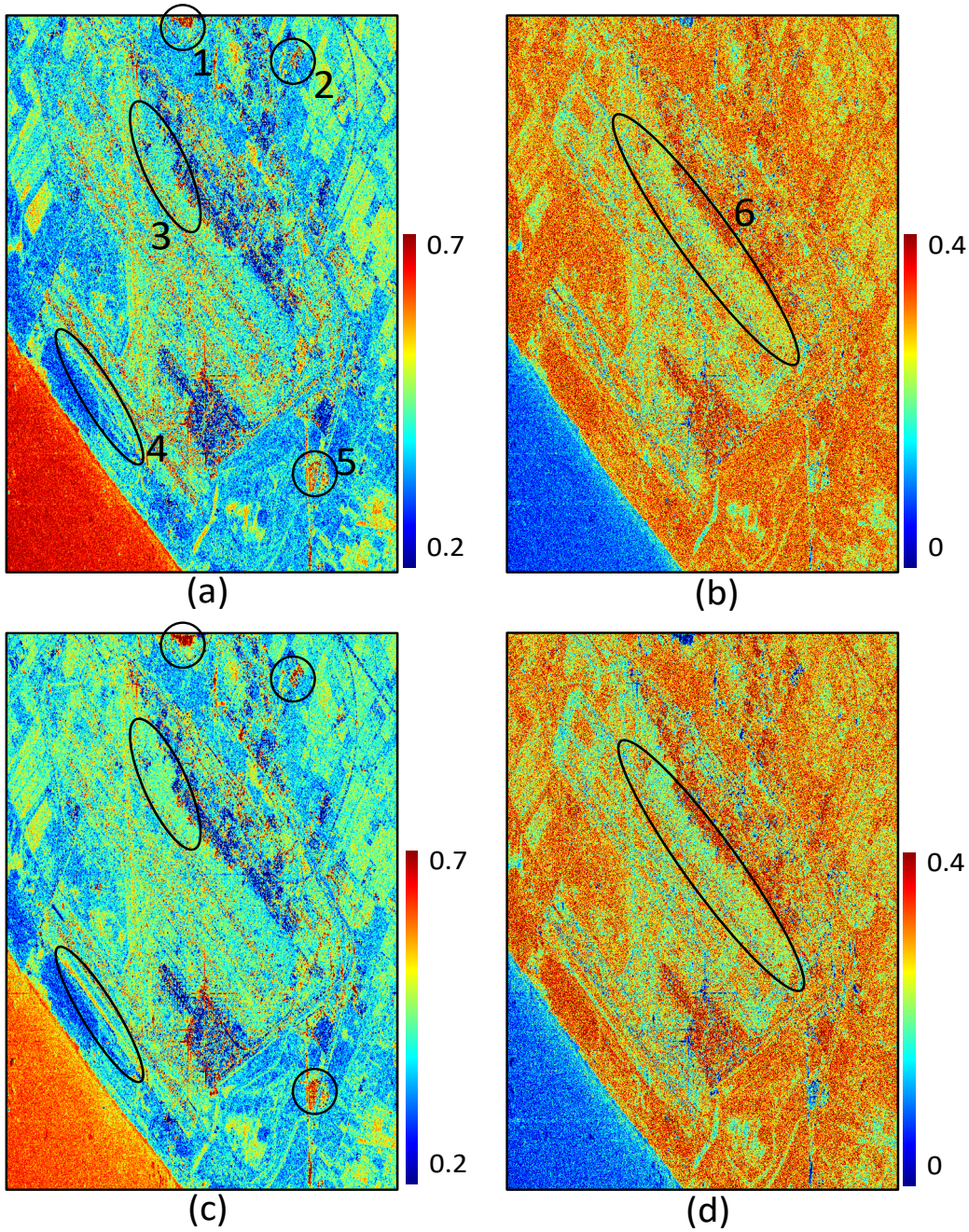

Fig. 5.16. Scatter mechanism maps obtained from the temporally averaged Radarsat-2 dual cross-pol data, $HH-VH$ and $VV-HV$. (a) and (b) are the values of similarity parameters r_1 and r_3 calculated with $VV-HV$. (c) and (d) are the values of similarity parameters r_1 and r_3 calculated with $HH-VH$.

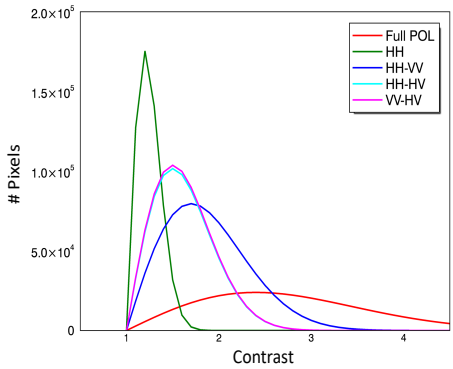

Fig. 5.17. Histograms of the ACE contrast enhancement using different combinations of polarimetric channels.

map. For each time span, the first column shows the simulated offset. The second is the offset obtained with averaged images while the third is the error, the difference between the retrieved deformation values and the real ones. The fourth is the offset obtained with images enhanced by AHE, and the fifth is the error. Finally, the sixth ad seventh are the results with the images enhanced by ACE. Deformation maps have color-scales ranging from -2 to +2 pixels while error maps from -0.5 to +0.5 pixels. Results for eight different periods are shown. The template size has a direct impact on the capability of OT to monitor non-spatially uniform deformations. These estimation errors are more noticeable in areas with larger deformation gradients, like the boundaries of the deformation bowl. Due to the averaging effect, some bias in the results can be found in areas with non-uniform deformation. The best results are obtained with ACE, no artifacts can be found outside the deformation bowl and the shape and values of deformation are determined with an acceptable degree of precision, around $\pm$ 0.2 pixels, for an OT estimation. The results with the original averaged images present artifacts outside the deformation bowl and their shape and values are not as precise as with ACE. Finally, AHE results are not satisfactory as well. The shape of the deformation bowl is worse estimated and the error values present a larger deviation.

The histograms of the error of the last time-span of Fig. 5.9,20100613-20120626 are shown in Fig. 5.10. It can be observed that the error distribution is not symmetric and biased to positive values. As expected, the ACE error histogram is the one that presents the lower dispersion, followed by the original averaged images and, closely, by AHE. The mean error for each case is -0.002,0.076 and 0.008 with error standard deviations of 0.073. 0.155 and 0.214, respectively. Clearly ACE is the method that provides the best results while AHE has the largest standard deviation of all.

5.2.2.2 Results in a Mountainous Area

The temporal average scattering mechanism decomposition results of mountainous area in Daliuta with 20 dual-pol $HH-VV$ TerraSAR-X images are shown in Fig. 5.11. Single reflections mainly happen on roads, farmlands with no vegetation, and valley flat areas. Double reflections distribute in hillsides, ridges, and building areas. The acquired entropy

is noisy and inaccurate due to the lack of cross-polar data. This is the reason that entropy does not participate in the enhancement processing for the $HH - VV$ case.

Same as in the airport test site, the scatter plots between the average amplitude and the similarity parameters of the three typical ground features (farmland, road, and building) are shown in Fig. 5.12. Compared with the farmland in the airport test site, the vegetation in the mountainous area is sparser and its height is lower, therefore the reflection is mainly single bounce. Although the amplitude difference between the three typical ground features in mountainous areas is small, it can still be seen that the group separation is clear in Figure (a) and (b). The lack of cross-polarization data leads to the confusion of different features about entropy.

It can be seen in Fig. 5.13 that the averaging do not improve the contrast. AHE and ACE make the building in the middle of the image sharper. On the other side, the road is clearer with ACE. Overall, the optimization effect is not as significant as in the airport test site due to the lack of cross-pol data. In addition, the contrast of the original data in the mountainous area is not as high as in the urbanized area.

After the enhancement, OT is applied to detect the deformation caused by coal mining. SAR images are base-banded before OT to accommodate the azimuth-varying spectra inherent to the spotlight mode and perform an alias-free interpolation. The size of the search window is set to 64×64 pixels to ensure a narrow correlation peak while retaining the deformation resolution.

The oversampling factor is set to 64 prior to cross correlation to reduce bias errors and noise [65]. The offset is converted, assuming that deformation is vertical, into subsidence, S_{sub}, with,

$$S_{\text{sub}} = \frac{P_{\text{offset}} \cdot R_{\text{size}}}{\cos\theta} \tag{5.31}$$

where P_{offset} is the measured offset in pixels before and after the deformation in the slant-range direction, θ is the local incident angle and R_{size} the pixel size in the range direction. The assumption that the deformation is vertical is realistic as the horizontal movement caused by underground mining is usually very small, about one-tenth of the vertical deformation [26].

Fig. 5.14 shows the subsidence time-series. The image pairs are the same as the deformation period indicated at the bottom of each deformation map. The first two rows are the result obtained with averaged images. The middle two rows and the last two rows are obtained with images enhanced by AHE and ACE, respectively. The deformation trends of the three result sets are similar, although the results with the first two sets are noisier and with more aretifacts outside the deformation bowl. It can be seen from the results that the deformation area was growing to the right during the entire observation period, and can be divided into two parts. The first sinking area resembles a triangle as a whole and was formed from April 5, 2014 to May 19, 2014. The subsidence values in this area are relatively large, reaching a maximum value close to 4 m. The second sinking area is strip-shaped and began to develop on May 19, 2014. The sinking area reached its maximum in early July 2014. After that, the sinking area remained basically unchanged, but the sinking values continued to increase. From the shape and development of the second sinking area, it can be seen that this is a typical underground mining caused

deformation. The coal seams in this area are thick and shallow. Therefore, it is speculated that the first sinking area was caused by mining at the same working face, but the surface collapsed, resulting in drastic changes in deformation and irregular shapes at the beginning of the observation.

5.3 Discussion

The proposed ACE-OT can improve the OT performance by the images contrast enhancement. The enhancement performance mainly depends on the capacity to separate the different scattering mechanisms. Since the current satellite SAR sensors can have up to four different polarization combinations (quad-pol $HH-VV-VH-HV$ and different dual-pol combinations, $HH-VH$, $VV-HV$ or $HH-VV$), it is necessary to compare their performance and evaluate the limitations of the dual-pol cases when extracting the similarity parameters. The 31 quad-pol Radarsat-2 images mentioned in Section 5.2.1 are used to simulate the different dual-pol combinations.

Fig. 5.15 shows the reflection mechanisms obtained considering only co-pol data, $HH-VV$. From Eq. (5.5), (5.6), (5.18) and (5.19) it can be found that the HH and VV data can distinguish single and double bounce effectively. However, due to the lack of cross-pol data, r_1 and r_2 are larger than those obtained by quad-pol data. The entropy obtained by the co-pol data has the same trend as the one obtained by the quad-pol data, the runways and bare land have low entropy values, while the buildings and land with vegetation have high entropy values. However, the lack of cross-pol data causes that many details are lost. For example, all boundaries become blurred and the lanes disappear. In addition, the entropy values in the black circles 1-4 in figure (c) are inconsistent with those from quad-pol data in Fig. 5.3. On the top of the black rectangle 5 and in the center of the black rectangles 6-7 in Fig. 5.15 (d), the entropy values obtained by quad-pol data are lower than those of its surroundings but it is just the opposite with $HH-VV$ data. For quad-pol data, in the black rectangle 8 there is bare land, that has low entropy values, that is surrounded by a vegetated area, with high entropy values. On the contrary, the results with dual-pol data of rectangle 4 show almost pure noise. These indicate that the lack of co-pol data not only causes a loss of details in the entropy map but also erroneous results.

Fig. 5.16 shows the scatter mechanisms obtained by $HH-VH$ and $VV-HV$ dual-pol data according to Eq. (5.25) and (5.26). It can be seen that the obtained single bounce contributions in Figure (a) and (c) are similar to the results obtained with quad-pol data, but the values of r_1 obtained by cross-pol data are smaller. For a small part of the farmlands (in the black circles 1, 2), the roads (in the black circle 4), and the parking lot (in the black circle 5), they have large r_1 values. But according to Fig. 5.3, quad-pol data shows that single bounce is weak and double bounce strong, which indicates that the $HH-VH$ and $VV-HV$ data cannot effectively distinguish between single and double bounce in these areas. Besides, in other areas r_1 values obtained by $HH-VH$ and $VV-HV$ data are inconsistent with each other. For example, in the black circle 3, the road has a lower single reflection value in Fig. 5.16 (a) than in Fig. 5.16 (c). This means that in these dual-pol combinations, the information of phase between the two channels cannot be unambiguously associated with scattering mechanisms. In other words, we

measure the reflected wave features (which depend on the incident polarisation), not the target features [92].

The entropy obtained from $HH-VH$ or $VV-HV$ data is similar to the one obtained by the quad-pol case, but some details are lost, and the values of r_3 obtained by cross-pol data are larger. For example, the boundary between the cement pavement and the aircraft runway in the black circle 6 is blurred, but it is perfectly clear in Fig. 5.3 (d).

The histograms of the optimized contrast for the four different polarization combinations plus HH are shown in Fig. 5.17. The contrast is calculated with Eq. (5.15) using a 3×3 moving averaging window. As it can be seen in Fig. 5.17, the initial image contrast represented by HH can be improved with the use of polarimetric data. The largest improvement is achieved with quad-pol data, followed by the dual-pol data with co-polar channels and finally the dual-pol with one co-polar and one cross-polar channels, almost with identical performance. Dual-pol with co-polar channels allows to better determine the reflection properties than the other dual-pol cases. Overall, the single reflection and double bounce obtained by two co-polar data are accurate. Although the entropy is unsatisfactory, it does not participate in the enhancement processing.

5.4 Summary

An Amplitude Contrast Enhancement (ACE) method taking advantage of polarimetric diversity is proposed in this paper in order to improve the performance of the images cross-correlation based OT deformation estimation. This method, which is inspired by [80], looks for the best combination of polarimetric reflection mechanisms to achieve the highest amplitude contrast in the images.

Two SAR data sets, one with 31 fully polarimetric Radarsat-2 images and the other with 20 dual polarization Terrasar-X images, have been used to evaluate the performance of the proposed method. The first dataset have been acquired over the Barcelona airport (Spain) while the second one over a mountainous mining area in Daliuta (China).

As benchmark, ACE has been compared with another contrast enhancement method. Among the different methods, the Adaptive Histogram Enhancement (AHE) has been selected as it works locally, which makes it comparable to ACE that does the same. The results show that the simulated offset added to the airport images can be better retrieved with ACE than with AHE. The former considers the scattering characteristics of the pixels when improving the contrast while the latter treats the data as a simple black and white image. The comparison of the original and retrieved deformation time-series has demonstrated the positive impact of the proposed contrast enhancement method in the performance of OT. Similarly, the large deformations caused by the coal mining activity in the mountainous area of Daliuta have been better obtained with ACE than with the original averaged polarimetric channels or AHE. The results have shown that subsidence values have reached values of almost 4 m in only 33 days. The comparison of the error maps for the three approaches indicates that ACE is able to provide more consistent results. Although the three methods are quite able to estimate the shape of the deformation bowl and their values, the results with the original images and AHE show non-consistent deformations throughout the deformation map. Non-consistent results

mean deformations that appear in a particular time interval but disappear in the next one, which obviously are not realistic.

The enhancing performances of the different polarization combinations, quad- and dual-pol, are discussed and analyzed. Firstly, the accuracy of the scatter mechanism extraction is validated. Among all dual-pol cases, $HH-VV$ combination presents the best performance obtaining the single and double reflections. The other dual-pol combinations, one co-polar and one cross-polar, can be quite inaccurate in some areas. Secondly, the performances among the different polarization combinations are then compared. As expected, quad-pol data achieves the highest contrast optimization. The performances of the combinations of one co-pol and one cross-pol data, $HH-VV$, are almost identical and clearly inferior to the combination of the two co-polar data, $HH-VV$.

6

Chapter 6
Conclusions and Future Lines

6.1 Main Conclusions

This PhD thesis is dedicated to improve the algorithms for obtaining large-gradient surface deformation based on SAR data. To this end, related researches have been carried out and three methods are proposed to optimize the existing algorithms. Specifically, a deformation resolving algorithm based on InSAR and an external model is proposed in **Chapter 3**, named as EMDD-PSI. In **Chapter 4**, an amplitude filtering method for distributed deformation detection is proposed to overcome the PL, and is named as PLR. To increase the cross correlation between the master and slave images for offset tracking, an contrast enhancement method is proposed in **Chapter 5**, named as ACE-OT.

The main experimental results and conclusions in this thesis could be summarized as follows:

- **Large gradient deformation extraction based on InSAR and an external model**

  In **Chapter 3**, an improved InSAR algorithm based on external models is proposed, named as EMDD-PSI. The algorithm first obtains the prior deformation phase by the external model, and then subtracts the prior deformation phase from the wrapped differential interference phase to obtain the residual phase. The residual phase is used to optimize the prior model parameters. Afterwards, the residual phase is unwrapped to obtain the residual deformation. The final deformation can

be obtained by adding the residual deformation and the prior deformation together.

The proposed method is verified with 14 ascending Radarsat-2 Stripmap images, acquired from April 4th, 2015 to March 5th, 2016. The test area is located in Fengfeng mining area, China, where the maximum subsidence velocity is about 44 cm/year, beyond the capability of PSI. Besides, the deformation area is covered by vegetation, which would reduced the density of PSs. These two reasons lead to phase aliasing, making it difficult to obtain the correct deformation. The proposed method can reduce or even eliminate the possibility of phase aliasing by separating part of the deformed phase from the original differential interferogram. The prior model is a nonlinear model, which is conducive to extracting nonlinear information. The results show that EMDD-PSI can effectively extract the deformation whose gradient exceeds the capability of PSI, and can retain the non-linear characteristics of the deformation. Ground truth also has verified the effectiveness of EMDD-PSI.

For the parameter optimization, the brute force is applied for its simplicity. The whole optimization process is convergent, and the optimized parameters can leads to the minimum residual phase.

The results of this part demonstrate that the EMDD-PSI method is an effective method for obtaining large gradient deformations.

- **Amplitude filtering**

  In **Chapter 4**, the distribution of SAR amplitude image and its influence on 6 different OT method has been analyzed and discussed, and a conclusion is reached: for the distributed deformation detection, pixels with too high and too low amplitude values will affect the detection accuracy. Based on this situation, an amplitude filter is proposed. The filter determines the amplitude retention interval based on the characteristics of the amplitude distribution, and the amplitude value of the pixel outside the retention interval is replaced with 0. To verify the proposed method, 19 spotlight TerraSAR-X SLC images are employed to monitor ground deformation with pixel spacing of 0.91×0.86 m. These images were acquired from November 10, 2012 to July 10, 2013. A deformation area located in Daliuta Town, China is selected to assess the performance of the proposed method. This area is the largest coal producing region in China, where the maximum subsidence value is about 4.2 m.

  The GPS data is used as the ground truth. The results show that the proposed amplitude filter can reduce or eliminate PL effectively, which means it can improve OT accuracy for obtaining distributed deformation. The monitoring accuracy is increased by 21.6% w.r.t. the OT method without amplitude filter.

- **Amplitude contrast enhancement based on polarization data**

  In **Chapter 5**, inspired by [80], a contrast enhancement algorithm based on polarization data is proposed. By recombining the energy of different scattering characteristics of scatterers, it achieves the purpose of enhancing the contrast of the amplitude image, thereby improving the accuracy of OT. First, the method of extracting the scattering characteristics from different polarization combinations is discussed. Then an optimizing formula is proposed to achieve the purpose of enhancing the amplitude contrast. It is worth noting that due to the incomplete

polarization information, the scattering features extracted by the dual polarization data may be not correct and noise is increased, which could weaken the optimization effect.

Time series Radatsat-2 and Terrasar-X data are used to verify the proposed method. An artificial area and a mountainous area are selected as the region of interest. Experiments show that the Pauli decomposition can effectively distinguish different scattering characteristics. The contrast enhancement algorithm can increase the characteristics of strong scatterers and weaken distributed scatterers. In addition, the coherence of the image pair with enhanced contrast will be significantly enhanced, and the gradient near the peak of the Correlation Coefficient (CC) coefficient will also increase, which is conducive to improving the accuracy and reliability of OT.

To conclude, **Chapter 3** answer the first research question of this thesis, i.e., *"How to determine parameters of an external model to help PSI obtain large gradient deformation without introduce error?"*. The second research question *"How can the PL be eliminated or reduced in OT processing?"* is partially answered by **Chapter 4**. The last one *"How to optimize polarimetric data to improve OT result?"* has been answered by **Chapter 5**.

6.2 Future Research Lines

The presented work in this thesis all have a certain improvement in the acquisition of large gradient deformation based on SAR data, but there are still some open issues that are worth continuing to study. The main points are listed below.

- **The selection of models participating PSI processing**

  Although PIM is a good model to describe the deformation caused by the underground coal mining, for other factors that cause surface deformation, such as volcanoes, earthquakes, landslides, etc., PIM cannot describe them well. The transability of external models could be a problem worth studying to apply EMDD-PSI to other cases. On the one hand, a more general model can be applied. This model should be able to describe all the causes of surface deformation, so EMDD-PSI can be applied to various scenarios, but the accuracy of the model may be limited. On the other hand, looking for suitable models for each deformation cases could be an option. Such a workload would be large and it would require knowledge of various disciplines, but the accuracy of the model will be higher, comparing to applying an universal model.

- **Deep learning based OT and InSAR fusion for large gradient deformation monitoring**

  Phase aliasing is an inevitable problem for InSAR when the movement of ground surface is vigorous. As a recent hot topic, deep learning technology can predict the missing phase cycle by training with a large number of samples. There is already research studying phase unwrapping to solve this problem. However, OT is not introduced into this field. Although the accuracy is far lower than InSAR, in some

incoherence area OT has better performance. On the other hand, more input data could make the learning model smarter. Therefore, deep learning based OT and InSAR fusion may be a good solution for large gradient deformation monitoring.

List of Figures

List of Tables

Bibliography

[1] T. J. Wright, Z. Lu, and C. Wicks, "Source model for the M_w 6.7, 23 October 2002, Nenana mountain earthquake (Alaska) from InSAR," *Geophysical Research Letters*, vol. 30, no. 18, 2003.

[2] B. Delouis, J.-M. Nocquet, and M. Vallée, "Slip distribution of the February 27, 2010 M_w= 8.8 Maule earthquake, central Chile, from static and high-rate GPS, InSAR, and broadband teleseismic data," *Geophysical Research Letters*, vol. 37, no. 17, 2010.

[3] M. Polcari, A. Montuori, C. Bignami, M. Moro, S. Stramondo, and C. Tolomei, "Using multi-band InSAR data for detecting local deformation phenomena induced by the 2016–2017 central Italy seismic sequence," *Remote Sensing of Environment*, vol. 201, pp. 234–242, 2017.

[4] O. Cavalié, C. Lasserre, M.-P. Doin, G. Peltzer, J. Sun, X. Xu, and Z.-K. Shen, "Measurement of interseismic strain across the Haiyuan fault (Gansu, China), by InSAR," *Earth and Planetary Science Letters*, vol. 275, no. 3, pp. 246–257, 2008.

[5] J. Biggs, F. Amelung, N. Gourmelen, T. H. Dixon, and S.-W. Kim, "InSAR observations of 2007 Tanzania rifting episode reveal mixed fault and dyke extension in an immature continental rift," *Geophysical Journal International*, vol. 179, no. 1, pp. 549–558, 2009.

[6] A. Singleton, Z. Li, T. Hoey, and J.-P. Muller, "Evaluating sub-pixel offset techniques as an alternative to D-InSAR for monitoring episodic landslide movements in vegetated terrain," *Remote Sensing of Environment*, vol. 147, pp. 133–144, 2014.

[7] D. Massonnet and K. L. Feigl, "Radar interferometry and its application to changes in the Earth's surface," *Reviews of Geophysics*, vol. 36, no. 4, pp. 441–500, 1998.

[8] Z. Lu and J. T. Freymueller, "Synthetic aperture radar interferometry coherence analysis over Katmai volcano group, Alaska," *Journal of Geophysical Research: Solid Earth*, vol. 103, no. B12, pp. 29887–29894, 1998.

[9] E. Chaussard, F. Amelung, and Y. Aoki, "Characterization of open and closed volcanic systems in Indonesia and Mexico using InSAR time series," *Journal of Geophysical Research: Solid Earth*, vol. 118, no. 8, pp. 3957–3969, 2013.

[10] D. Massonnet, P. Briole, and A. Arnaud, "Deflation of Mount Etna monitored by spaceborne radar interferometry," *Nature*, vol. 375, no. 6532, pp. 567–570, 1995.

[11] X. Ding, G. Liu, Z. Li, Z. Li, and Y. Chen, "Ground subsidence monitoring in Hong Kong with satellite SAR interferometry," *Photogrammetric Engineering & Remote Sensing*, vol. 70, no. 10, pp. 1151–1156, 2004.

[12] L. Ge, C. Rizos, S. Han, and H. Zebker, "Mining subsidence monitoring using the combined InSAR and GPS approach," in *Proceedings of the 10th International Symposium on Deformation Measurements*, pp. 1–10, 2001.

[13] S. Samsonov, N. d'Oreye, and B. Smets, "Ground deformation associated with post-mining activity at the French–German border revealed by novel InSAR time series method," *International Journal of Applied Earth Observation and Geoinformation*, vol. 23, pp. 142–154, 2013.

[14] K. Yang, L. Yan, G. Huang, C. Chen, and Z. Wu, "Monitoring building deformation with InSAR: Experiments and validation," *Sensors*, vol. 16, no. 12, p. 2182, 2016.

[15] C. Zhao, Z. Lu, Q. Zhang, C. Yang, and W. Zhu, "Mining collapse monitoring with SAR imagery data: a case study of Datong mine, China," *Journal of Applied Remote Sensing*, vol. 8, no. 1, p. 083574, 2014.

[16] X. Diao, K. Wu, D. Zhou, and L. Li, "Integrating the probability integral method for subsidence prediction and differential synthetic aperture radar interferometry for monitoring mining subsidence in Fengfeng, China," *Journal of Applied Remote Sensing*, vol. 10, no. 1, p. 016028, 2016.

[17] H. Fan, L. Lu, and Y. Yao, "Method combining probability integration model and a small baseline subset for time series monitoring of mining subsidence," *Remote Sensing*, vol. 10, no. 9, p. 1444, 2018.

[18] K. Goel and N. Adam, "A distributed scatterer interferometry approach for precision monitoring of known surface deformation phenomena," *IEEE Transactions on Geoscience and Remote Sensing*, vol. 52, no. 9, pp. 5454–5468, 2013.

[19] M. Zheng, K. Deng, S. Du, J. Liu, J. Liu, and J. Feng, "Joint Probability Integral Method and TCPInSAR for Monitoring Mining Time-Series Deformation," *Journal of the Indian Society of Remote Sensing*, vol. 47, no. 1, pp. 63–75, 2019.

[20] T. A. Scambos, M. J. Dutkiewicz, J. C. Wilson, and R. A. Bindschadler, "Application of image cross-correlation to the measurement of glacier velocity using satellite image data," *Remote Sensing of Environment*, vol. 42, no. 3, pp. 177–186, 1992.

[21] R. Kotyński and K. Chałasińska-Macukow, "Optical correlator with dual nonlinearity," *Journal of Modern Optics*, vol. 43, no. 2, pp. 295–310, 1996.

[22] A. Gray, K. Mattar, P. Vachon, R. Bindschadler, K. Jezek, R. Forster, and J. Crawford, "InSAR results from the RADARSAT Antarctic Mapping Mission data: estimation of glacier motion using a simple registration procedure," in *IGARSS'98. Sensing and Managing the Environment. 1998 IEEE International Geoscience and Remote Sensing. Symposium Proceedings.(Cat. No. 98CH36174)*, vol. 3, pp. 1638–1640, IEEE, 1998.

[23] M. Debella-Gilo and A. Kääb, "Sub-pixel precision image matching for measuring surface displacements on mass movements using normalized cross-correlation," *Remote Sensing of Environment*, vol. 115, no. 1, pp. 130–142, 2011.

[24] X. Shi, L. Zhang, T. Balz, and M. Liao, "Landslide deformation monitoring using point-like target offset tracking with multi-mode high-resolution TerraSAR-X data," *ISPRS Journal of Photogrammetry and Remote Sensing*, vol. 105, pp. 128–140, 2015.

[25] E. Erten, "Glacier velocity estimation by means of a polarimetric similarity measure," *IEEE Transactions on Geoscience and Remote Sensing*, vol. 51, no. 6, pp. 3319–3327, 2013.

[26] H. Fan, X. Gao, J. Yang, K. Deng, and Y. Yu, "Monitoring mining subsidence using a combination of phase-stacking and offset-tracking methods," *Remote Sensing*, vol. 7, no. 7, pp. 9166–9183, 2015.

[27] C. Wang, X. Mao, and Q. Wang, "Landslide displacement monitoring by a fully polarimetric SAR offset tracking method," *Remote Sensing*, vol. 8, no. 8, p. 624, 2016.

[28] S.-H. Yun, H. Zebker, P. Segall, A. Hooper, and M. Poland, "Interferogram formation in the presence of complex and large deformation," *Geophysical Research Letters*, vol. 34, no. 12, 2007.

[29] V. D. Navarro-Sanchez, J. M. Lopez-Sanchez, and F. Vicente-Guijalba, "A contribution of polarimetry to satellite differential SAR interferometry: Increasing the number of pixel candidates," *IEEE Geoscience and Remote Sensing Letters*, vol. 7, no. 2, pp. 276–280, 2009.

[30] V. D. Navarro-Sanchez, J. M. Lopez-Sanchez, and L. Ferro-Famil, "Polarimetric approaches for persistent scatterers interferometry," *IEEE Transactions on Geoscience and Remote Sensing*, vol. 52, no. 3, pp. 1667–1676, 2013.

[31] R. Iglesias, D. Monells, X. Fabregas, J. J. Mallorqui, A. Aguasca, and C. Lopez-Martinez, "Phase quality optimization in polarimetric differential SAR interferometry," *IEEE Transactions on Geoscience and Remote Sensing*, vol. 52, no. 5, pp. 2875–2888, 2013.

[32] B. Wu, L. Tong, Y. Chen, and L. He, "New methods in multibaseline polarimetric SAR interferometry coherence optimization," *IEEE Geoscience and Remote Sensing Letters*, vol. 12, no. 10, pp. 2016–2020, 2015.

[33] B. Wu, L. Tong, Y. Chen, and L. He, "Improved SNR optimum method in PolDInSAR coherence optimization," *IEEE Geoscience and Remote Sensing Letters*, vol. 13, no. 7, pp. 982–986, 2016.

[34] Z. Sadeghi, M. J. V. Zoej, and J.-P. Muller, "Monitoring land subsidence in a rural area using a combination of ADInSAR and polarimetric coherence optimization," *IEEE Journal of Selected Topics in Applied Earth Observations and Remote Sensing*, vol. 10, no. 8, pp. 3582–3590, 2017.

[35] M. Esmaeili and M. Motagh, "Improved Persistent Scatterer analysis using Amplitude Dispersion Index optimization of dual polarimetry data," *ISPRS Journal of Photogrammetry and Remote Sensing*, vol. 117, pp. 108–114, 2016.

[36] M. Esmaeili, M. Motagh, and A. Hooper, "Application of dual-polarimetry SAR images in multitemporal InSAR processing," *IEEE Geoscience and Remote Sensing Letters*, vol. 14, no. 9, pp. 1489–1493, 2017.

[37] K. Ishitsuka, T. Matsuoka, and M. Tamura, "Persistent scatterer selection incorporating polarimetric SAR interferograms based on maximum likelihood theory," *IEEE Transactions on Geoscience and Remote Sensing*, vol. 55, no. 1, pp. 38–50, 2016.

[38] A. G. Mullissa, V. Tolpekin, A. Stein, and D. Perissin, "Polarimetric differential SAR interferometry in an arid natural environment," *International Journal of Applied Earth Observation and Geoinformation*, vol. 59, pp. 9–18, 2017.

[39] A. G. Mullissa, D. Perissin, V. A. Tolpekin, and A. Stein, "Polarimetry-based distributed scatterer processing method for PSI applications," *IEEE Transactions on Geoscience and Remote Sensing*, vol. 56, no. 6, pp. 3371–3382, 2018.

[40] Z. Sadeghi, M. J. V. Zoej, and J.-P. Muller, "Combination of persistent scatterer interferometry and single-baseline polarimetric coherence optimisation to estimate deformation rates with application to tehran basin," *PFG–Journal of Photogrammetry, Remote Sensing and Geoinformation Science*, vol. 85, no. 5, pp. 327–340, 2017.

[41] I. G. Cumming and F. H. Wong, "Digital processing of synthetic aperture radar data," *Artech House*, vol. 1, no. 3, 2005.

[42] M. I. Skolnik, "Introduction to radar systems," *New York*, 1980.

[43] T. P. Ager, "An introduction to synthetic aperture radar imaging," *Oceanography*, vol. 26, no. 2, pp. 20–33, 2013.

[44] J.-S. Lee and E. Pottier, *Polarimetric radar imaging: from basics to applications*. CRC Press, 2017.

[45] W. A. Holm and R. M. Barnes, "On radar polarization mixed target state decomposition techniques," in *Proceedings of the 1988 IEEE National Radar Conference*, pp. 249–254, IEEE, 1988.

[46] A. Freeman and S. L. Durden, "A three-component scattering model for polarimetric SAR data," *IEEE Transactions on Geoscience and Remote Sensing*, vol. 36, no. 3, pp. 963–973, 1998.

[47] E. Krogager, "New decomposition of the radar target scattering matrix," *Electronics Letters*, vol. 26, no. 18, pp. 1525–1527, 1990.

[48] W. L. Cameron and H. Rais, "Conservative polarimetric scatterers and their role in incorrect extensions of the Cameron decomposition," *IEEE Transactions on Geoscience and Remote Sensing*, vol. 44, no. 12, pp. 3506–3516, 2006.

[49] D. Just and R. Bamler, "Phase statistics of interferograms with applications to synthetic aperture radar," *Applied Optics*, vol. 33, no. 20, pp. 4361–4368, 1994.

[50] H. A. Zebker, J. Villasenor, *et al.*, "Decorrelation in interferometric radar echoes," *IEEE Transactions on Geoscience and Remote Sensing*, vol. 30, no. 5, pp. 950–959, 1992.

[51] F. Gatelli, A. M. Guamieri, F. Parizzi, P. Pasquali, C. Prati, and F. Rocca, "The wavenumber shift in SAR interferometry," *IEEE Transactions on Geoscience and Remote Sensing*, vol. 32, no. 4, pp. 855–865, 1994.

[52] O. Mora, J. J. Mallorqui, and A. Broquetas, "Linear and nonlinear terrain deformation maps from a reduced set of interferometric SAR images," *IEEE Transactions on Geoscience and Remote Sensing*, vol. 41, no. 10, pp. 2243–2253, 2003.

[53] P. Blanco-Sanchez, J. J. Mallorquí, S. Duque, and D. Monells, "The coherent pixels technique (CPT): An advanced DInSAR technique for nonlinear deformation monitoring," in *Earth Sciences and Mathematics*, pp. 1167–1193, Springer, 2008.

[54] P. Blanco-Sanchez, *SAR Differential Interferometry for deformation monitoring under a multi-frequency approach.* PhD thesis, Ph. D. Thesis, Universitat Politècnica de Catalunya, Barcelona, Spain, 2009.

[55] A. Ferretti, C. Prati, and F. Rocca, "Permanent scatterers in SAR interferometry," *IEEE Transactions on Geoscience and Remote Sensing*, vol. 39, no. 1, pp. 8–20, 2001.

[56] F. Zhao and J. J. Mallorqui, "A temporal phase coherence estimation algorithm and its application on DInSAR pixel selection," *IEEE Transactions on Geoscience and Remote Sensing*, vol. 57, no. 11, pp. 8350–8361, 2019.

[57] P. Berardino, G. Fornaro, R. Lanari, and E. Sansosti, "A new algorithm for surface deformation monitoring based on small baseline differential SAR interferograms," *IEEE Transactions on Geoscience and Remote Sensing*, vol. 40, no. 11, pp. 2375–2383, 2002.

[58] O. Mora, J. J. Mallorqui, and A. Broquetas, "Linear and nonlinear terrain deformation maps from a reduced set of interferometric SAR images," *IEEE Transactions on Geoscience and Remote Sensing*, vol. 41, no. 10, pp. 2243–2253, 2003.

[59] R. Lanari, O. Mora, M. Manunta, J. J. Mallorquí, P. Berardino, and E. Sansosti, "A small-baseline approach for investigating deformations on full-resolution differential SAR interferograms," *IEEE Transactions on Geoscience and Remote Sensing*, vol. 42, no. 7, pp. 1377–1386, 2004.

[60] R. Iglesias, *High-Resolution Space-Borne and Ground-Based SAR Persistent Scatterer Interferometry for Landslide Monitoring.* PhD thesis, Ph. D. Thesis, Universitat Politècnica de Catalunya, Barcelona, Spain, 2015.

[61] L. G. e. a. He G Q, Yang L, *Mining subsidence.* China University of Mining and Technology Press, 1991.

[62] D. Massonnet and K. L. Feigl, "Radar interferometry and its application to changes in the Earth's surface," *Reviews of Geophysics*, vol. 36, no. 4, pp. 441–500, 1998.

[63] C. N. C. I. Bureau, *Rules for coal pillar retention and coal mining in buildings, water bodies, railways and main shafts*. Coal industry press, 2000.

[64] H. Fan, L. Lu, and Y. Yao, "Method combining probability integration model and a small baseline subset for time series monitoring of mining subsidence," *Remote Sensing*, vol. 10, no. 9, p. 1444, 2018.

[65] C. Werner, U. Wegmuller, T. Strozzi, and A. Wiesmann, "Precision estimation of local offsets between pairs of SAR SLCs and detected SAR images," in *International Geoscience and Remote Sensing Symposium*, vol. 7, p. 4803, 2005.

[66] A. Singleton, Z. Li, T. Hoey, and J.-P. Muller, "Evaluating sub-pixel offset techniques as an alternative to D-InSAR for monitoring episodic landslide movements in vegetated terrain," *Remote Sensing of Environment*, vol. 147, pp. 133–144, 2014.

[67] X. Hu, T. Wang, and M. Liao, "Measuring coseismic displacements with point-like targets offset tracking," *IEEE Geoscience and Remote Sensing Letters*, vol. 11, no. 1, pp. 283–287, 2013.

[68] R. Michel, J.-P. Avouac, and J. Taboury, "Measuring ground displacements from SAR amplitude images: Application to the Landers earthquake," *Geophysical Research Letters*, vol. 26, no. 7, pp. 875–878, 1999.

[69] G. A. Arciniegas, W. Bijker, N. Kerle, and V. A. Tolpekin, "Coherence-and amplitude-based analysis of seismogenic damage in Bam, Iran, using ENVISAT ASAR data," *IEEE Transactions on Geoscience and Remote Sensing*, vol. 45, no. 6, pp. 1571–1581, 2007.

[70] A. Papoulis and S. U. Pillai, *Probability, random variables, and stochastic processes*. Tata McGraw-Hill Education, 2002.

[71] R. Bamler and M. Eineder, "Accuracy of differential shift estimation by correlation and split-bandwidth interferometry for wideband and delta-k SAR systems," *IEEE Geoscience and Remote Sensing Letters*, vol. 2, no. 2, pp. 151–155, 2005.

[72] E. Sansosti, P. Berardino, M. Manunta, F. Serafino, and G. Fornaro, "Geometrical SAR image registration," *IEEE Transactions on Geoscience and Remote Sensing*, vol. 44, no. 10, pp. 2861–2870, 2006.

[73] H. Fan, X. Gao, J. Yang, K. Deng, and Y. Yu, "Monitoring mining subsidence using a combination of phase-stacking and offset-tracking methods," *Remote Sensing*, vol. 7, no. 7, pp. 9166–9183, 2015.

[74] F. Zhao and J. J. Mallorqui, "Coherency matrix decomposition-based polarimetric persistent scatterer interferometry," *IEEE Transactions on Geoscience and Remote Sensing*, vol. 57, no. 10, pp. 7819–7831, 2019.

[75] F. Zhao and J. J. Mallorqui, "SMF-POLOPT: An adaptive multitemporal pol (DIn) SAR filtering and phase optimization algorithm for PSI applications," *IEEE Transactions on Geoscience and Remote Sensing*, vol. 57, no. 9, pp. 7135–7147, 2019.

[76] R. Iglesias González, A. Aguasca Solé, F. J. Fabregas Canovas, J. J. Mallorquí Franquet, D. Monells Miralles, C. López Martínez, and L. Pipia, "Ground-based polarimetric SAR interferometry for the monitoring of terrain displacement phenomena-part II: applications," *IEEE Journal of Selected Topics in Applied Earth Observations and Remote Sensing*, vol. 8, no. 3, pp. 994–1007, 2015.

[77] L. Pipia, X. Fabregas, A. Aguasca, C. Lopez-Martinez, S. Duque, J. J. Mallorqui, and J. Marturia, "Polarimetric differential SAR interferometry: First results with ground-based measurements," *IEEE Geoscience and Remote Sensing Letters*, vol. 6, no. 1, pp. 167–171, 2008.

[78] C. López-Martínez, X. Fàbregas, and L. Pipía, "PolSAR and PolInSAR model based information estimation," in *IEEE International Geoscience and Remote Sensing Symposium*, vol. 3, pp. III–959, IEEE, 2009.

[79] F. Zhao, J. J. Mallorqui, and J. M. Lopez-Sanchez, "Impact of SAR Image Resolution on Polarimetric Persistent Scatterer Interferometry With Amplitude Dispersion Optimization," *IEEE Transactions on Geoscience and Remote Sensing*, 2021.

[80] J. Yang, G. Dong, Y. Peng, Y. Yamaguchi, and H. Yamada, "Generalized optimization of polarimetric contrast enhancement," *IEEE Geoscience and Remote Sensing Letters*, vol. 1, no. 3, pp. 171–174, 2004.

[81] J. Yang, Y.-N. Peng, and S.-M. Lin, "Similarity between two scattering matrices," *Electronics Letters*, vol. 37, no. 3, pp. 193–194, 2001.

[82] W. Boerner, H. Brand, L. Cram, D. Giessing, and A. Jordan, "Inverse methods in electromagnetic imaging; Proceedings of the NATO Advanced Research Workshop, Bad Windsheim, West Germany, September 18-24, 1983. Parts 1 & 2," *Inverse Methods in Electromagnetic Imaging*, 1985.

[83] W.-M. Boerner, L. A. Cram, W. A. Holm, D. E. Stein, W. Wiesbeck, W. Keydel, D. Giuli, D. T. Gjessing, F. A. Molinet, and H. Brand, *Direct and inverse methods in radar polarimetry*, vol. 350. Springer Science & Business Media, 2013.

[84] W.-M. Boerner, "Introduction to radar polarimetry–with assessments of the historical development and of the current State-of-the-Art," *Electromagnetic Wave Interactions*, pp. 139–214, 1996.

[85] A. Kostinski and W. Boerner, "On the polarimetric contrast optimization," *IEEE Transactions on Antennas and Propagation*, vol. 35, no. 8, pp. 988–991, 1987.

[86] J. Huynen, *Phenomenological theory of radar targets*. PhD thesis, Technical University of Delft, 1970.

[87] S. R. Cloude and E. Pottier, "An entropy based classification scheme for land applications of polarimetric SAR," *IEEE Transactions on Geoscience and Remote Sensing*, vol. 35, no. 1, pp. 68–78, 1997.

[88] A. Swartz, H. Yueh, J. Kong, L. Novak, and R. Shin, "Optimal polarizations for achieving maximum contrast in radar images," *Journal of Geophysical Research: Solid Earth*, vol. 93, no. B12, pp. 15252–15260, 1988.

[89] H. Mott and W.-M. Boerner, "Polarimetric contrast enhancement coefficients for perfecting highresolution POL-SAR/SAL image feature extraction," in *Wideband Interferometric Sensing and Imaging Polarimetry*, vol. 3120, pp. 106–117, International Society for Optics and Photonics, 1997.

[90] M. R. Hestenes, E. Stiefel, *et al.*, *Methods of conjugate gradients for solving linear systems*, vol. 49. NBS Washington, DC, 1952.

[91] S. M. Pizer, E. P. Amburn, J. D. Austin, R. Cromartie, A. Geselowitz, T. Greer, B. ter Haar Romeny, J. B. Zimmerman, and K. Zuiderveld, "Adaptive histogram equalization and its variations," *Computer Vision, Graphics, and Image Processing*, vol. 39, no. 3, pp. 355–368, 1987.

[92] L. Mascolo, S. R. Cloude, J. M. Lopez-Sanchez, *et al.*, "Model-based decomposition of dual-pol SAR data: application to Sentinel-1," 2021.

List of Publications

Journal Articles

J1 **S. Du**, J. J. Mallorquí, H. Fan, et al, "Improving PSI Processing of Mining Induced Large Deformations with External Models," *Remote Sensing*, vol. 12, no. 19, pp. 1: 1-18, September 2020.

Conference Papers

C1 **S. Du**, J. J. Mallorquí, H. Fan "Improving PSI Processing of Mining Induced Large Deformations with External Models," *EUSAR 2021, Leipzig, Germany*, pp. 2196-2199.

C2 **S. Du**, J. J. Mallorquí "An improvement of offset tracking for cross hair (CH) and patch like (PL) elimination and reliability estimation for large deformation monitoring with SAR data," *IGARSS 2021, Brussels, Belgium*, WE2.MM-15.9.